Tomas Bata University in Zlín
Centre of Polymer Systems

Doctoral Thesis

Viscoelastic Response of Magnetorheological Suspensions

Viskoelastická odezva magnetoreologických suspenzí

Author: M.Sc. Andrei Munteanu

Degree programme: Nanotechnology and Advanced materials P0719D130002

Supervisor: prof. Ing. Michal Sedlačík, Ph.D.

Zlín, October 2024

Published by Tomas Bata University in Zlín in the Edition Doctoral Thesis Summary.

The publication was issued in the year 2024.

Key words in Czech: *magnetoreologie, karbonylové železo, nanotrubice, polypyrol, magnetoreologické elastomery, magnetoreologické tekutiny*

Key words: *magnetorheology, carbonyl iron, nanotubes, polypyrrole, magnetorheological elastomers, magnetorheological fluids*

Full text of the doctoral thesis is available in the Library of TBU in Zlín.

DEDICATION

These 4 years and 3 months are dedicated to Νικολέττος Μερκούριος "Nikole'ttos Merkou'rios" a childhood friend who was lost during a car accident during this Ph.D. His music and memories followed me in this journey.

"Χρόνου φείδου μάγκα, κάποτε οι ώρες θα τελειώσουν"
"Spend your time wisely dude, eventually the hours will run out"

ΙΧΩΡ - Εντρυφώ by Nikolletos Merkourios

ABSTRACT

Smart materials are usually referred to the systems that can alter some of their properties when exposed to an external stimulus. Magnetorheological fluids (MRFs) and elastomers (MREs) are categorized as good examples of smart materials as they are able to change properties such as their mechanical properties and conductivity under the influence of a magnetic field. This topic has grown significantly both in the fundamental research and applications however, there is a big gap in between as in fundamental research only one type of flow is studied while in real applications, more types of flow are present. This thesis tries to marry the fundamental research of MRFs and MREs with their applications. Different types of MRFs were developed based on specific applications. To be specific this thesis includes the development of conductive and magnetic composites based on polypyrrole (PPy), magnetite nanoparticles, nickel and iron microparticles (carbonyl iron) which were used as an MRF. The particles are used as electrical devices that are able to control the resistance and capacitance under the influence of an external magnetic field. Additionally, due to the ability of the PPy to be synthesised in different morphology, dimorphic MRFs were investigated filling an important gap of the field. Due to the rise of MRE-based materials, it is important to prepare recyclable MREs. Thermoplastic-based MREs were prepared based on several types of matrices including a thermoplastic polyurethane and a propylene-based elastomer supplemented with ethylene groups. Both types of MREs are able to be reprocessed several times. The mechanical properties after processing were similar to the initial batches. The reprocessing was simulated by studying the time dependency of the MREs and it was found that the matrix can interact and bond with the magnetic particles.

Keywords: *magnetorheology, carbonyl iron, nanotubes, polypyrrole, magnetorheological elastomers, magnetorheological fluids*

ABSTRAKT

Chytré materiály jsou obvykle označovány jako systémy, které mohou změnit některé ze svých vlastností, když jsou vystaveny vnějšímu podnětu. Magnetoreologické kapaliny (MRF) a elastomery (MRE) jsou příklady takových inteligentních materiálů, protože jsou schopny měnit vlastnosti, jako jsou jejich mechanické vlastnosti a vodivost, pod vlivem magnetického pole. Tyto materiály se těší výrazné pozornosti jak v základním výzkumu, tak v aplikacích, stále však existují možnosti jejich dalšího vylepšení. Tato práce se snaží spojit základní výzkum MRF a MRE s jejich aplikacemi. Na základě specifických aplikací byly vyvinuty různé typy MRF. Konkrétně tato práce zahrnuje vývoj vodivých a magnetických kompozitů na bázi polypyrrolu (PPy), nanočástic magnetitu, mikročástice niklu a železa (karbonylové železo), které byly použity jako MRF. Takový systém lze použít pro elektrická zařízení, která jsou schopna řídit odpor a kapacitu pod vlivem vnějšího magnetického pole. Navíc, vzhledem k možnostem syntézy PPy v různých morfologiích, byly zkoumány dimorfní MRF, které vyplňují důležitou mezeru v oboru. S ohledem na nárůst materiálů a aplikací na bázi MRE je důležité připravovat recyklovatelné MRE. V práci byly připraveny MRE na bázi termoplastů na základě několika typů matric včetně termoplastického polyuretanu a elastomeru na bázi propylenu doplněného ethylenovými skupinami. Oba typy MRE lze několikrát přepracovat. Mechanické vlastnosti po zpracování byly podobné jako u původních šarží. Přepracování bylo simulováno studiem časové závislosti MRE a bylo zjištěno, že matrice se při tomto procesu může interagovat a vázat s magnetickými částicemi.

Klicova slova: *magnetoreologie, karbonylové železo, nanotrubice, polypyrol, magnetoreologické elastomery, magnetoreologické tekutiny*

ACKNOWLEDGMENTS

I would like to acknowledge Michal Sedlacik my supervisor for giving me the opportunity to do this Ph.D. and for always helping me in need. Martin Cvek who was unoficially my consultant and who always used his free time to help me when needed. Our close partners Jaroslav Stejskal and Miroslava Trchova who despire being retired, are dedicated to science and without their advices and help, half of my papers would not exist. Similarly, Marek Jurca who is my trusted chemist, was always there for me when I needed advice, help with synthesis and much more. My African friend, Asabuwa who was the first chemist I worked with. Our coleagues from Pardubice, the group of Prof. Kalendova who gave us the very intersting paints to work with. Tomas Plachy who in times of need helped us with extra measurements. Our partners from Romania, Prof. Bica and Dr. Anitas who trusted in our materials and performed their excelent electrical characterization. All my coleagues, fellows Ph.D. students and recent postdocs for always making my day, keeping me in a good mood and giving me helpfull advice. Our administrative office coleagues, Klara Sedlackova, Martina Dostalova and Michal Studeny for their patience with me. Lastly, Lenka Munteanu my wife who helped me the most during my Ph.D. in the office, labs but also back home.

Contents

1. INTRODUCTION

1.1 Origins

The aim of this introduction part is to provide a reader interested in magnetorheology with a short description of the basic concepts of the science together with some basic physics from related fields. Magnetorheology is a complex word of Greek origin which combines the terms “magneto” i.e. “μαγνήτο” [maghni’to] and “rheology” i.e. “ρεολογία” [reologhi’a] with the latter being composed of two more words “ρέω” [re’o] which means the verb flow and “λόγος” [lo’ghos] which according to the most common translation means “reason” but in this case, it means “speech”, which is typical for definitions of sciences. Thus, rheology is the science that studies flow. “Μαγνήτο” comes from “Μαγνήτης” [Maghni’tis] (Magnet in English) which should be written with capital as it literally means the person who is descended from a specific Ionian tribe called “Μαγνησία” [Maghnisi’a] (Magnesia in English) which was colonized from the Magnesia of Thessaly in Greece. The meaning of the magnet nowadays comes from the Magnets of Ionia whose lands were rich of the mineral magnetite and are currently in Turkey. The term magnetorheology is the science of the flow behaviour of materials with magnetic properties, although the term does not have an official definition. Magnetorheological (MR) is thus a material whose rheological properties can be altered with a presence of a magnetic field. For the second and last word of this thesis’ title “suspension” describes the systems used for the thesis as unfortunately typical magnets are solid and will not flow in our lifetime for temperatures below their Curie temperature. Thus, the systems described here are suspensions of solid magnetic particles suspended in a fluid. However, the more appropriate term describing the systems used in this thesis would be dispersions.

1.2 Introduction to Magnetorheology and Magnetorheological Materials

The MR dispersions used in this thesis can be divided into two categories. On one hand magnetorheological fluids (MRFs) and on the other, magnetorheological elastomers (MREs). The former is a suspension consisted of ferromagnetic particles with size (in terms of hydrodynamic radius) higher of that of a micrometer [1]. These particles are dispersed in a fluid, thus a viscous medium, which depends on the desired applications [2]. A suspension, or more appropriately a colloid, of magnetic particles in the nanometer range is given the term ferrofluid which may undergo different magnetic phenomena such as Neel’s relaxation. The regime between ~100–1000 μm is unexplored due to the large remanent magnetization that the particles of that size have [3].

Magnetorheological elastomers on the other hand are also dispersions of magnetic particles with the same size criteria, however the dispersed phase is an elastomer matrix thus a viscoelastic medium [4, 5].

The MR dispersions are categorized as smart materials. Their most common applications take advantage of the material's ability to tune its mechanical properties upon exposure to a magnetic field. The altering of the mechanical properties happens within a millisecond. Once exposed to a magnetic field, the magnetic particles align in a column-like structure to minimize their free energy (see **section 2.3**). These columns add an additional elastic contribution, transforming the fluid in a soft solid or a yield stress fluid which is usually orders of magnitude higher than the stresses reached at the proportional shear rates when no magnetic field is applied [6]. The fraction of the material's shear stress with/without the presence of a magnetic field is commonly referred as the "MR effect" and it is the most important quantity of an MR material. Depending on the imposed magnetic field, the MR effect varies from the order of unity and can exceed four orders of magnitude [7]. This ability to alter the internal structure of the material is utilized in several applications with most notable including dampers, valves, and robotics [8-10]. Both types of MR dispersions are facing severe challenges which will be discussed later in detail [11].

2. THEORETICAL PART

2.1 Magnetic Particles

The most commonly used magnetic particles for MR-based research are by far the Carbonyl Iron (CI) particles due to their high saturation magnetization (*M*s) of ~200 emu/g which is a key quantity for the MR performance of the suspension. For comparison, magnetite-based particles which are the most commonly used in commercial magnetic suspensions may have ~4 times lower *M*s as depicted in **Fig. 2.1**. Despite having the highest *M*s, magnetite particles saturate faster (for lower fields) which is a useful property that is not utilized in literature. For that reason, both CI and composite magnetic particles based on magnetite are used in this thesis.

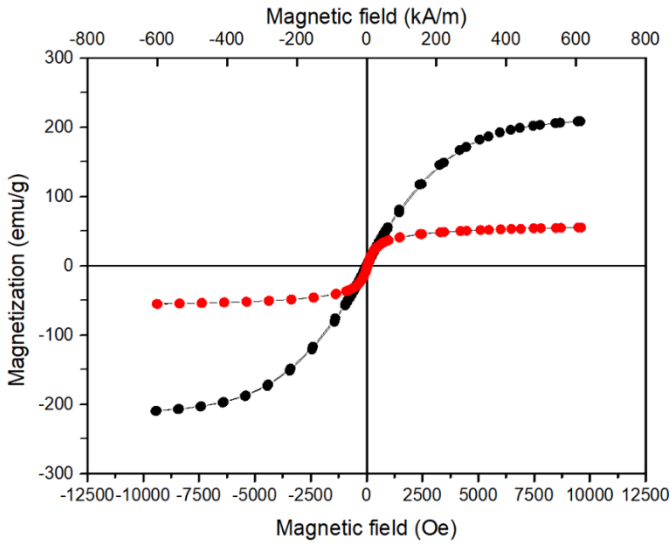

Figure 2.1 Vibrating sample magnetometry for CI CN grade (black) and a magnetite-based composite (red; PPy 6 later in this thesis).

The size of the particle affects its *M*s which is generally reduced with size as displayed in **Fig. 2.2a**. Particles in the range of the nm have a single domain which allows them to obtain the superparamagnetic status either through Neel's or thermal magnetic relaxation, or through thermal rotation. Larger particles in the range of a 100 nm display higher values of *M*s due to surface effects however, the presence of just a handful domains creates a large remanence which creates strong attractions between the particles during off-state. This results in the irreversible agglomeration of the magnetic particles which diminishes the system's stability. Lastly, a further increase of the particles size will result in the shrinkage of the permanent magnetization as the domains become too many and cancel each other out and in the end a net (practically) zero coercivity is achieved. Thus, the particles of this size display an ultra-soft ferromagnetic-like behaviour. The *M*s for particles of this size is further increased and so the MR performance which

establish them as great candidates for engineering applications [12]. The size effect in terms of the coercive field is shown in **Fig. 2b** together with the range where a dispersion consisted of such particles would be considered a ferrofluid or an MRF/MRE. The value of the coercive field is important for the stability of the system because the magnetostatic attractions between the particles may surpass the electrostatic repulsions of the double layer, thus the lowest remanence possible is preferred [13].

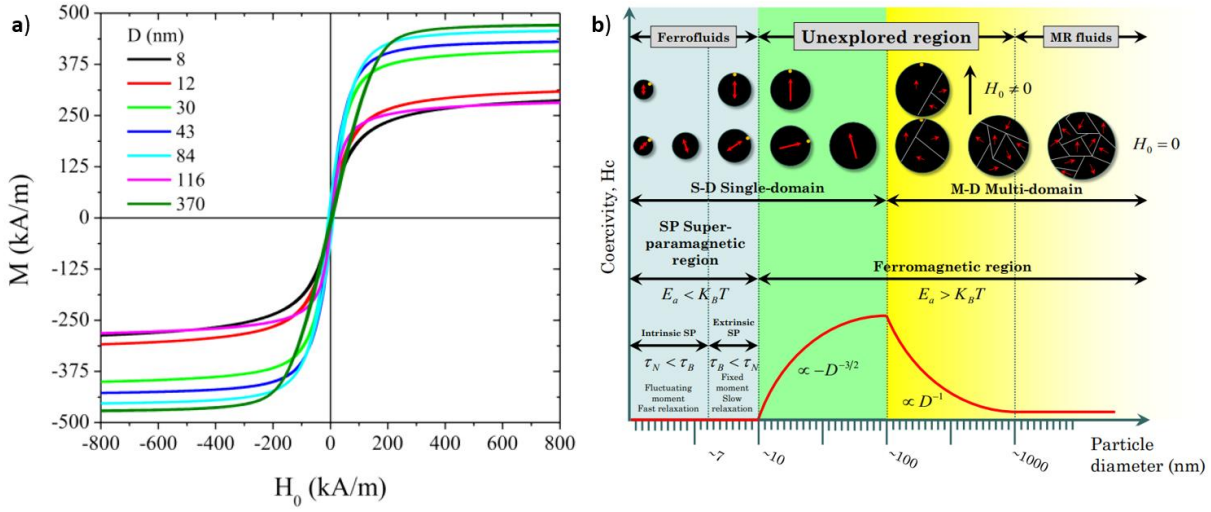

Figure 2.2 a) Magnetic curves for iron particles of various size. b) The effect of the size on the coercivity and the magnetic behaviour of iron particles. Several regions emerge namely the Ferrofluids region where below a critical size the particles display superparamagnetic behaviour due to Neel's relaxation and shortly after thermal rotation. For a second critical size the anisotropy energy surpasses k_bT and the particles obtain a remanent magnetization. The region continues until multiple domains are formed to lower the total magnetic energy and is called unexplored because the particles flocculate. Eventually as the particle's size is further increased, the magnetic domains are too many and have an almost net zero coercivity and at this point the region of the MR fluids begins [3].

Usually, the magnetic component of the particles is either coated or a part of a composite material to ensure a good affinity with the dispersed phase [14]. Depending on the dispersed phase, polar or non-polar coatings can be applied. A good affinity between the two phases ensures a stable and homogeneous material and without it, the particles aggregate and form clusters [15]. A second reason for the coating is the reduction of the density. The most commonly used magnetic particles (made of iron) have a density around ~7.9 g/cm^3 while the dispersed phase usually has a density near the unity thus, a huge density mismatch exists between these components. As a result, the sedimentation stability can be improved by reducing the overall density through coating of the particle and providing a better affinity with the continuous phase [16]. Lastly, coatings provide

functional groups which can be used in certain applications and provide chemical stability in aggressive environments [17]. Unfortunately, the magnetic particles inherit some of the negative effects from the coatings including high cost, complex preparation but more importantly a decline of magnetic properties since the coatings are non-magnetic materials. The decline of the magnetic properties is proportional to the amount of the coating thus thick coatings reduce the *M*s by a large amount [18].

Lastly, an important parameter affecting both, the MR performance and the stability of the system is the particles' shape [19, 20]. The mostly common shapes for the magnetic particles include spheres; however, there is a lot of interest for rods as well [21]. Spherical CI particles are produced massively, easily, and cheaply [22]. Rod-like particles on the other hand, have more complex preparations and usually do not have significantly different magnetic properties [23] with the exception of the demagnetization factor. The morphology plays a significant role for MRFs which suffer from the high sedimentation rates [24]. Rod-like particles with a high length over radius ratio have a large free volume which results in thermodynamic repulsions within the suspension, thus reducing the sedimentation rate [7].

2.2 Dispersed Phase

As mentioned before, there are two types of dispersed phases depending if the material is characterized as an MRF or MRE. The particles are suspended in liquids and solid matrices for MRFs and MREs, respectively, thus the prime difference between the two is the viscosity. For the former, the most common liquid phases include silicone and mineral oils; however, different liquids for different applications can be are used. There are two main concerns in regards to MRFs. First the interactions between the particles and the liquid carrier. Bad affinity between the carrier and the particles will result in irreversible large agglomerates which will settle and the suspension will no longer have any uses. Secondly, sedimentation is occurring naturally and many studies were dedicated to either diminish the effect of study it [25]. The sedimentation in a laminar flow was described by Stokes in the following expression:

$$u_s = \frac{2\,R^2 g}{9\,\nu}\,\left(\frac{\rho_p}{\rho_s} - 1\right) \qquad 2.1$$

where u_s is the sedimentation velocity, R the radius of the particle, ν the kinematic viscosity, g the gravitational acceleration, ρ_p the density of the particles, and, ρ_s the density of the solvent. The sedimentation velocity is inversely proportional to the viscosity of the liquid carrier and it is impacted by the density mismatch of the system. It is obvious that it is easier to fight sedimentation using carriers with

higher viscosity. Unfortunately, the viscosity of the carrier also affects the MR performance of the material. When a magnetic field is applied the particles within the suspension form chain-like structures which transform the suspension in a soft yield stress fluid. The viscosity of the carrier acts as a hinderance for the chains with its effect already well established [26]. So, a high viscosity hinders both the sedimentation and the magnetic response of the material thus the liquid carrier should be selected accordingly.

An obvious advantage of the MREs is the solid polymeric matrix in which the particles are embedded. Thus, sedimentation is not an issue however, the MR effect is significantly smaller when compared to MRFs which is not a big issue as MREs have their own unique applications. Due to the enormous advances in the polymer sciences, there are countless potential properties that MREs may inherit, thus vastly changing the type of the application from polymer to polymer. The most common types of polymeric matrices include the following. Silicon rubber is a great candidate as it can be ordered at various molecular weights thus, controlling the materials viscosity/elasticity. Additionally, this rubber is usually in a liquid state which allows the particles to be well distributed during preparation. Lastly, if cured under the presence of a magnetic field, the chain-like structures that the magnetic particles form will be permanent, an attribute that MRFs do not have [27]. Thermoplastic elastomers allow the reprocessing of the MRE allowing them to be recycled without losing their MR properties [28]. Lastly, the dispersed phase can be a two-component system thus it is important to include MR materials like MR foams and MR gels which have their own unique properties and uses [29]. There are several other types of polymeric matrices with genius applications however, it is out of the scope of this thesis. Similarly, both MREs and MRFs may include different types of additives which improve the materials however, these are not part of the investigation for this thesis.

2.3 Magnetorheological Effect

The MR effect was described as the alignment of the particles when an external magnetic field is applied which is shown in **Fig. 2.3**. Assuming there are no other forces and the medium is non-magnetic, during the off-state, the particles are randomly dispersed. When a magnetic field is applied, the particles become magnetized. Assuming that the particles act as single dipoles and (a fairly accurate approximation), the state with the lowest energy is achieved when the particles organize themselves into chains which are as far away as possible given the simple dipole potential energy:

$$U = -\vec{m} \cdot \vec{H} \qquad 2.2$$

with $\vec{m}$ and $\vec{H}$, being the magnetization of a single dipole and the magnetic field imposed from an external magnetic field (which can be considered as a neighboring dipole), respectively.

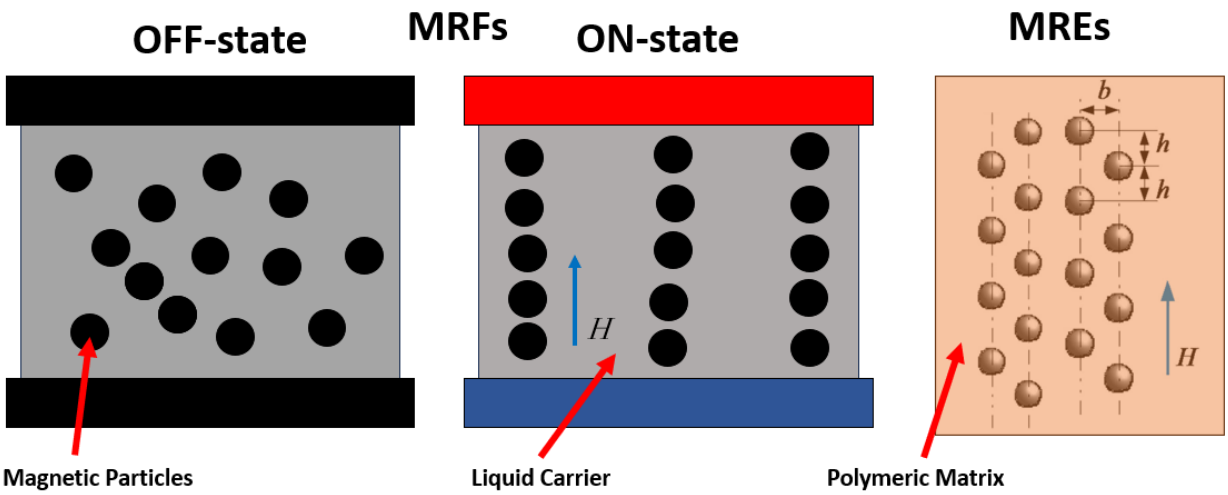

Figure 2.3 Schematic illustration of the MR mechanism for MRFs in chain-like structures and for MREs as suggested from Han et al [30]

This mechanism is very accurate for the liquid carriers whose viscosity values are low, thus mainly MRFs. For materials with a higher viscosity the particles cannot move (as) freely within the medium and are locked in place. This is the case for MREs which still possess an MR effect, however, a different mechanism is suggested. In this case the particles are also considered small enough to be considered as magnetic moments and all of them are considered to share the same magnetization. Then the interaction energy for 2 dipoles can be written as:

$$U = \frac{\mu_0 m^2}{4\pi r^3}(1 - 3cos^2\theta) \qquad 2.3$$

where μ_0, r and θ are the permeability of free space, the distance between the moments, and their angle, respectively. Again, the energy takes its lowest value when the moments are parallel in chain-like structures. By defining a shear strain, it is possible to show that a positive MR effect takes place through the derivatives of the interaction energy [31]. However, for a uniaxial deformation the opposite is true. Experimentally, MREs experience a positive MR effect during uniaxial deformation thus it was proposed that the particles obtain wavy configurations which topologically is closer to the reality as can be seen in **Fig. 2.3** [30].

Lastly, a different kind of MR effect which is not often mentioned is the change in electrical properties of the material. For MRFs, during the on-state, the formation of chain-like structures allows for conductive pathway to be formed. The carriers can move more efficiently thus increasing the conductivity of the system. It is suggested that the carrier transport is achieved via both variable-range

hopping mechanism or the correlated barrier hopping [32]. Similar to the mechanical properties, the conductivity is less affected in MREs. The particles are not aligning thus the barrier is higher for the charges to overcome. For anisotropic MREs on the other hand, the particles are aligned during curing and remain with the chain-like structure even during the off-state. For these MREs the conductivity is increased as well due to the magnetostriction phenomenon which reduces the distance between particles thus reducing the barrier for the charge carriers to bypass which increases the conductivity [33].

2.4 Rheology of MR systems

Rheology is a powerful tool to describe, characterize, and analyze MR systems. Magnetorheological systems usually display a complex behaviour which needs to be decoded in order to understand and determine if the given sample is appropriate for a specific application.

2.4.1 Rheology of MRFs

Magnetorheological fluids can be investigated using both rotation and oscillation modes; however,1 this thesis is focusing mainly in rotational rheology as it is the most common type of operational mode in applications [34]. In these experiments, a rotational deformation is imposed to the sample and the stress is measured by rheometer for a given shear rate. The most typical characterization test is the measurement of stress for increasing shear rates which is commonly known as a flow curve. The dynamic viscosity (henceforth always referred to as viscosity) is defined as the ratio of the shear stress over the shear rate. For fluids 4 typical behaviours are shown in **Fig. 2.4**. For the Newtonian behaviour, the viscosity remains constant and independent of the shear rate. For shear thinning and shear thickening behaviour on the other hand, the viscosity decreases or increases respectively with increasing shear rate. Magnetorheological fluids with all of these behaviours have been reported [21]. Lastly, materials that require a certain load to flow (Bingham plastic in **Fig. 2.4**, such as toothpaste, are important as this type of behaviour resembles well MRFs during the on-state. A typical flow curve for an MRF is shown in **Fig. 2.5a**. During the off-state a given suspension with a low concentration of magnetic particles φ displays a Newtonian behaviour. When an external magnetic field is applied the particles form chain-like structures and as a result the stress is increased and the behaviour changes to that of a yield stress fluid. Higher fields result to more robust chains, thus higher yield stresses (τ_y). Once the particles are magnetically saturated, the yield stress does not increase anymore. At lower shear rates the magnetostatic interactions dominate. At some point, as the shear rate is increased, the hydrodynamic forces will become relevant and a short transition region is observed. Before long, the hydrodynamic forces will surpass the magnetic and chains will be disrupted leading back to a

Newtonian behaviour or an overall Bingham plastic. The yield stress dependence on the external magnetic field is divided in three different power laws depending on its strength and is displayed in **Fig. 2.5b**. At small fields, the yield stress is proportional to the strength of the magnetic squared.

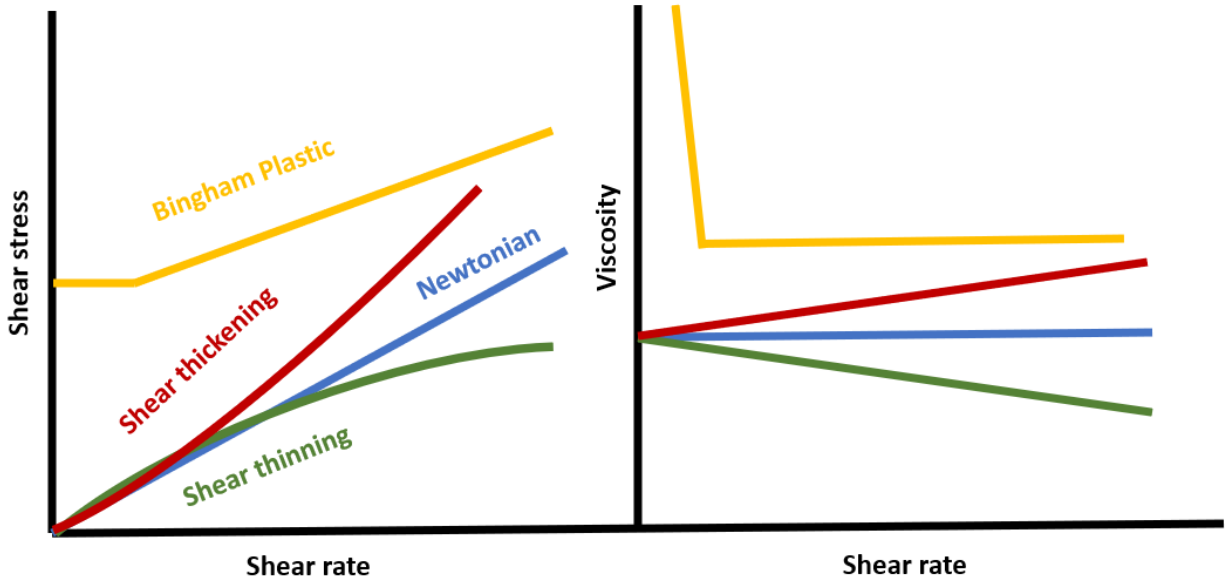

Figure 2.4 Typical flow profiles for various types of fluids.

When saturation begins the power law is $\tau_y \sim M_s^{0.5} H^{1.5}$ and eventually for larger magnetic fields $\tau_y \sim M_s^2$, with M_s being the saturation magnetization of the particles [35]. The yield stress depends on the particle concentration and at low φ the dependence is linear. At some point the power law becomes greater than unity [36]. Then there is an increase in viscosity and that is due to increase of the yield strength, this increase can be many orders of magnitude. This behavior is commonly known as the Bingham model and it is shown by the following equation:

$$\tau = \tau_y + \mu\dot{\gamma} \qquad 2.4$$

Where μ, and $\dot{\gamma}$ are constant with viscosity units, and the shear rate, respectively. Note that when the hydrodynamic forces take over, the behaviour can be non-Newtonian where other models for yield stress materials can be used such as the Herschel Bulkley, De Kee and more [37]. Other parameters that influence the flow curves include the temperature, the pressure, the polydispersity and the morphology which this thesis is more concern about. It is important to note that MRFs whose magnetic forces operate over a broad shear rate range are appreciated the most.

In the field of magnetorheology, the ration of the hydrodynamic forces over the magnetic ones is both a very important and a known quantity named Mason number (*Mn*) which is given by the following expression [26]:

$$Mn = \frac{9\, n_m \dot{\gamma} \varphi}{2\mu_o \mu_m M_m^2} \qquad 2.5$$

where n_m the dynamic viscosity of the continuous phase, μ_0 the permeability of the free space, μ_m the permeability of the continuous phase, and, M_m the magnetization of the suspension.

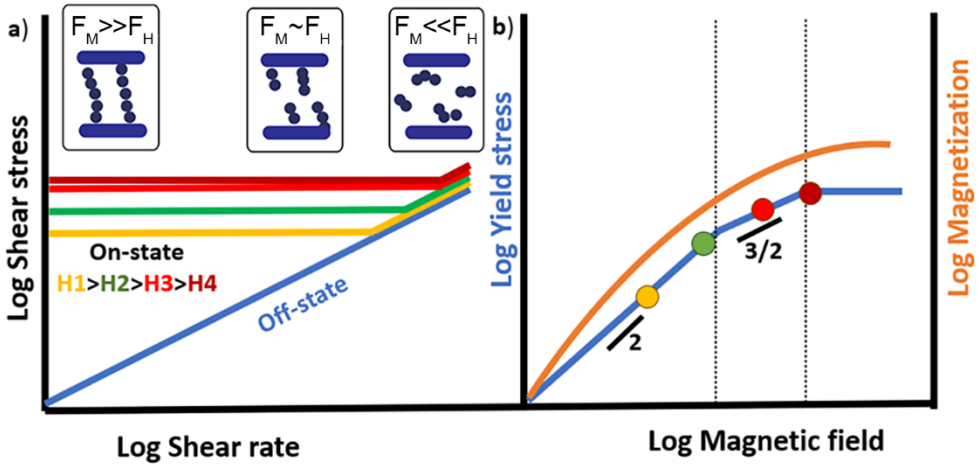

Figure 2.5 a) Typical flow curves for a hypothetical MRF during the on- and off-state together with an illustration of the fluid's structure. b) The yield stress and magnetization dependency on the magnetic field in blue and orange respectively for the same hypothetical MRF. The slopes are indicating the yield stress dependency and coloured circles the yield stress from part a).

Basically, a high *Mn* corresponds to the domination of the hydrodynamic forces. As can be seen in **Fig. 2.6a** the viscosity drops with a constant rate until a critical *Mn** is reached where the hydrodynamic forces are of the same order as the magnetic ones. Shortly after, hydrodynamic forces dominate reaching the high shear rate plateau. The *Mn* allows the data to be plotted in a single mastercurve with an example shown in **Fig. 2.6b** and as can be seen, since *Mn* is always <<1, the magnetic contribution dominates. It must be noted that all of the Eq 2.5 components are either known or can be estimated precisely from a single magnetic curve of the magnetic particles given the viscosity of the carrier is also known (usually provided from the supplier). So, using the *Mn*, it is easy to predict the MR behaviour of an MRF for a broad range of concentrations without performing any experiments which saves time and resources thus highly appreciated by the industry.

Other important numbers include the λ parameter which is the ration between the magnetic and thermal forces:

$$\lambda = \frac{\pi \mu_o \mu_m b^2 R^3 H^2}{2 k_b T} \qquad 2.6$$

where k_b, T, and, b are the Boltzmann's constant, the absolute temperature, and, the magnetic coupling parameter respectively. At saturated fields λ scales with M_m instead. The systems used in this thesis have relatively large R and H thus it is assumed that λ>>1. The λ parameter is connected with the *Mn* though the Peclet number $Pe = 1.5Mn\lambda$ [35].

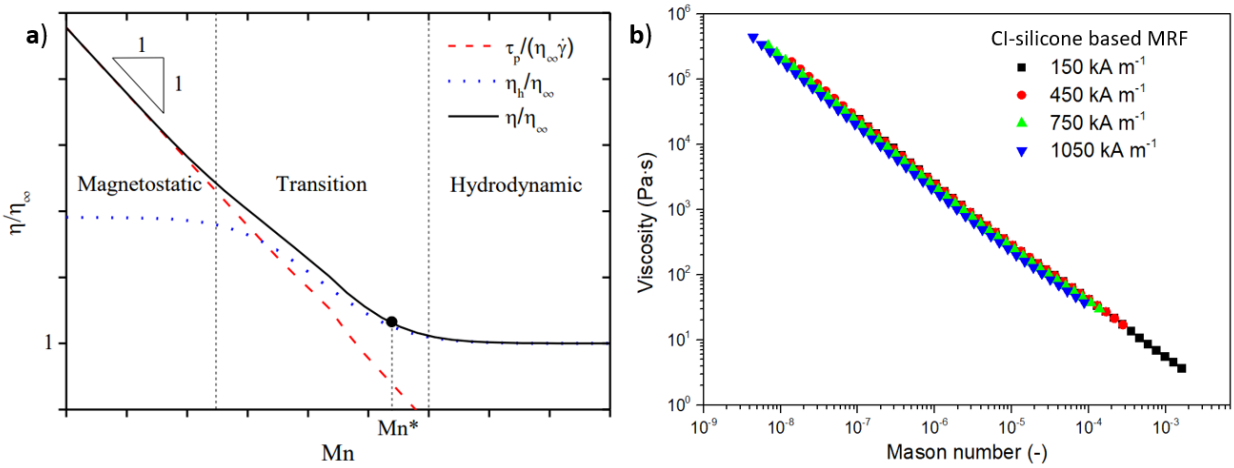

Figure 2.6 a) Apparent viscosity as a function of Mn. The red and blue dotted line represent the magnetic and hydrodynamic contributions to the viscosity and the black line is the overall behaviour. [38] b) An example of a mastercurve for a standard CI based MRF [7].

Lastly, the most important ration not discussed yet is the MR effect which essentially describes the performance of the MRF at a specific magnetic field value and shear rate. To be specific the MR effect is defined as the ration between the on-state stress or viscosity over the corresponding off-state value. For oscillatory tests instead of complex viscosity, usually the storage modulus *G'* is used to calculate the MR effect in a similar to the rotational rheology way. More precisely the MR effect for the rotational and oscillatory modes is defined in the following equations:

$$e_r = \frac{\tau_{on}}{\tau_{off}} = \frac{n_{on}}{n_{off}}, \qquad 2.7$$

$$e_s = \frac{G'_{on}}{G'_{off}} \qquad 2.8$$

2.4.2 Rheology of MREs

There are various applications in which MREs are used in oscillatory mode such as dampers and shock absorbers [39]. An efficient way to investigate the viscoelastic properties of a material is achieved through oscillatory tests. In these

experiments, an oscillatory deformation is applied to the sample at a given frequency and the stress is measured by rheometer. The regime where the stress and strain have a linear relationship at any frequency is called linear viscoelastic regime. The stress response is sinusoidal which usually has a phase lag compared to the imposed strain. A completely elastic material is in phase with the strain. On the other hand, a completely viscous material has a 90° phase angle difference. A viscoelastic material shows a response between elastic and viscous and hence the phase angle (δ) is between 0–90° which is usually the case for MREs. The phase angle holds the viscoelastic information, from the imposed strain and the measured stress.

The viscoelastic information can be extracted from the complex modulus G^* and the phase angle which allows the separation of G^* into a real and an imaginary part. The real part (G') is the storage modulus or elastic modulus which represents the stored deformation energy and it is usually associated with the MR effect. The imaginary part (G'') is the loss modulus which represents the tendency to dissipate energy thus very important in the damping applications of the MREs. The phase angle may take values of 0° and 90° responding to purely elastic and viscous behavior, respectively, whereas intermediate values correspond to a viscoelastic behavior. Materials with higher G' than G'' are said to display a solid-like behaviour. Likewise, if the G'' is considerably higher the materials experience a liquid-like behaviour. The equations which connect these parameters are:

$$G^* = (G'^2 + G''^2)^{1/2} \tag{2.9}$$

$$G' = G^* \cos(\delta) \tag{2.10}$$

$$G'' = G^* \sin(\delta) \tag{2.11}$$

$$\tan(\delta) = \frac{G''}{G'} \tag{2.12}$$

Several types of oscillatory tests can be used to investigate the behavior of MREs materials with the most common discussed in detail below.

Dynamic Strain Sweep (DSS) tests describe the deformation behavior of a material, these tests are mainly used to investigate the limit of the applied deformation in which the inner structure of the material remains unaffected. For a given temperature, an oscillatory deformation is applied at a constant frequency for varying strain amplitudes and the G' and G'' at each strain are calculated. The linear viscoelastic regime (LVE) is defined as the range of strain at which the storage modulus G' becomes strain independent. The critical strain γ_L (the onset of non-linearity) in **Fig. 2.7a** indicates the limit of the LVE at the point where the

plateau of *G'* starts to drop. In the LVE, tests can be carried out without destroying the material's internal structure. For MREs specifically these measurements are more complex as these are usually highly filled polymers, thus subject to the Payne effect [40]. The signature of the effect is a sudden shoulder of the *G"* towards the end of the LVE as can be seen in **Fig. 2.7b**. Applying a magnetic field usually shifts the values of the *G'* to higher values without changing the trend of the overall behaviour.

Dynamic Time Sweep (DTS) tests are mainly used in curing studies and are also useful to observe solvent evaporation or drying. Additionally, these tests can detect the thermal degradation of the sample and crosslinking which is relevant to this thesis [41].

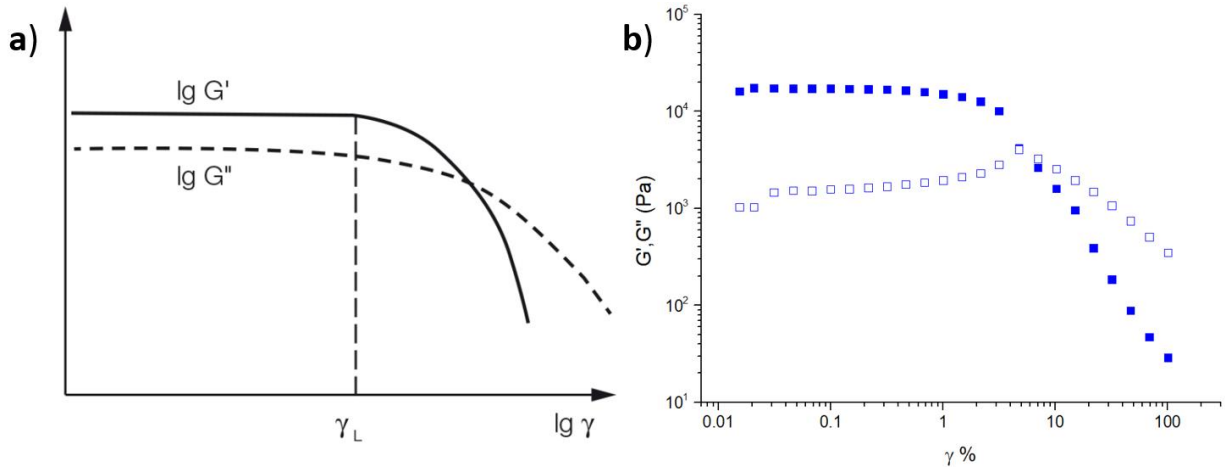

Figure 2.7 a) Typical DSS for a polymeric system. The plateau of G' indicates the linear regime with γ_L being the limit of linearity [41]. b) DSS for a carbon black based elastomer, closed and open symbols correspond to G' and G", respectively.

These tests have been used to study MREs with time-dependent behaviour, for instance, systems where the particles and the host matrix interact. Potential changes in the viscoelasticity are detected over time while the material undergoes an oscillatory deformation at a constant strain and frequency. In this thesis, DTS tests are used to secure that the sample has reached steady state when the samples were loaded at high temperatures. This is indicated when *G'* and *G"* are not changing with time as shown **Fig. 2.8** where after ~6 minutes the sample reached a steady state however, it can take much longer even several days.

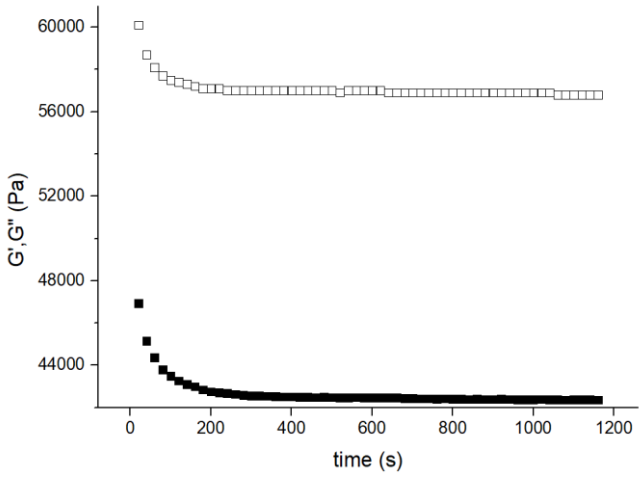

Figure 2.8 DTS for a CI/thermoplastic-based MRE right after loading at 170 °C. Closed and open symbols correspond to G' and G'', respectively.

Dynamic Frequency Sweep (DFS) tests describe the viscoelastic spectra of a material. Repeating these tests for different temperatures, characteristics like the melting point, glass transition, rubbery plateau, relaxation times, phase transitions and more can be studied [42]. The strain amplitude is kept constant and the frequency is varied. The shape of *G'* and *G''* over frequency can characterize the material's structure. A common example for linear polybutadiene with entanglements is shown in **Fig. 2.9**. The viscoelastic spectrum is shown in four regions corresponding to different characteristic sizes and a characteristic relaxation time for each size can be extracted. For the glassy region at high frequencies or short times (or low temperatures), the behavior is solid-like with modulus being time independent. Such short times correspond to the chemical bonds and the molecules are shown seem "frozen" as the frequency is higher that their movement. Giving more time for the molecules to start moving, the modulus drops as local parts of the chains start to relax. As the time passes, larger parts relax further reducing the moduli until the chains are completely relaxed and the material is flowing. However, usually the molecular weight of the polymer is large enough and there are entanglements in which case a plateau is formed just like in **Fig. 2.9**. The time needed for the chains to completely relax depends on the molecular weight and when the terminal regime is reached, the Maxwel behaviour with a characteristic drop of the moduli can be observed, indicated with the slopes of 1 for *G''* and 2 for *G'* in a log scale as shown in **Fig. 2.9**. For MREs the two regions at low frequencies are important since above the T_g the chains are frozen and so are the particles, thus no MR effect can be displayed.

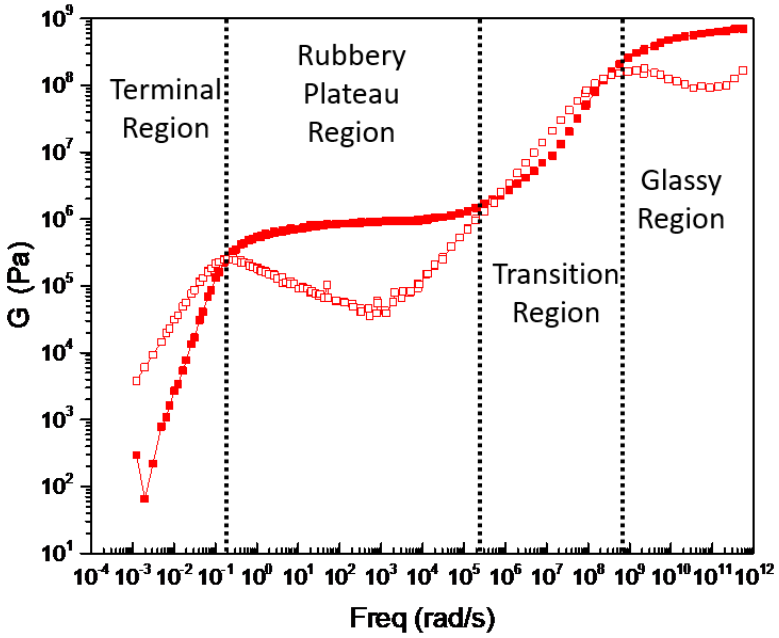

Figure 2.9 Viscoelastic moduli G' and G" (closed and opened symbols, respectively, for a linear polybutadiene with Mw = 155 Kg/mol at 250 K. The data were kindly provided by Leo Gury.

Adding the magnetic particles to the pure polymer will shift the rubbery plateau to a higher modulus. The value of the rubbery plateau for the pure polymer is important to know as the MR effect for a given particle concentration can be calculated relevantly accurately [31]. The terminal regime is also very important as MREs which just like filled elastomers do not display the Maxwell behaviour. Instead, *G'* and *G"* either drop with different slopes or even display a secondary plateau. To conclude, DFS graphs and their derivatives may give great insight of the material's structures and are a powerful tool to characterize an MRE.

3. MOTIVATION AND AIMS OF THE THESIS

3.1 Motivation

Progress in MRFs by the Juan de Vicente, Daniel J. Klingenberg and Jose R. Morillas were the inspiration to study the topic of this thesis due to their creativity and dedication to the field [11, 26, 35, 43-46]. The field of magnetorheology has many advances in both fundamental research and applications. However, in the author's opinion there is a big gap separating these advances. For example, fundamental research uses perfect homogeneous fields which are unlikely to be achieved in applications. On the contrary, the flow and deformations in real applications are not considered in fundamental research. Works that will marry fundamental research with the applications for both MRFs and MREs is the main motivation of this thesis.

3.2 Aims

Aims of this study include:

- Study of polypyrrole-based MRFs
- Study the impact of magnetic tubes in conventional MRFs
- Fabrication and study of electronic devices based on various MRFs
- Fabrication of recyclable MREs
- Study the particle-matrix interaction within MREs

4. SELECTED RESULTS

4.1 Polypyrrole nanotubes-based MRFs

In this thesis 2 types of magnetic particles are used. First, conventional CI particles supplied by BASF (Germany) and secondly, polypyrrole (PPy) based magnetic nanotubes which were synthesized [7]. The PPy nanotubes were synthesised and decorated with magnetite nanoparticles during a two-step synthesis. Two samples were synthesized at different molarities of iron (III) chloride hexahydrate ($FeCl_3 \cdot 6H_2O$). **Table 4.1** presents the amount of each component used with the mole ratio of $FeCl_3 \cdot 6H_2O$ over pyrrole represented as *n*. For the synthesis, firstly the pyrrole (>97%) was dispersed in water (0.2 M in 100 mL) with methyl orange (0.004 M in 100 mL) being added later on. The dye is the key substance which guides the growth of tube-like morphology instead of spheres. Aside, a second solution of $FeCl_3 \cdot 6H_2O$ in water ($FeCl_3 \cdot 6H_2O$ is 0.5 M in 100 mL for *n*=2.5 and 1.2 M in 100 mL for n=*6*) was prepared. Right after, both solutions were combined and the polymerization of pyrrole to the PPy nanotubes was complete at room temperature once the mixture turned dark brown/black and thickened with the procedure taking a few minutes. **Fig. 4.1** shows the main synthesis reactions. The final molar concentrations of the reaction mixture are: 0.1 M pyrrole; 0.25 M $FeCl_3 \cdot 6H_2O$ – for *n*=2.5 and 0.6 M for *n*=6 and 0.002 M methyl orange. To decorate the PPy nanotubes with magnetite, the resulting PPy dispersion was mixed with an excessive amount of ammonium hydroxide (4 M) at room temperature until the solution became basic (pH > 10). Lastly, the decorated nanotubes were isolated by filtration and washed with ethanol. The particles were left to dry overnight at 60 °C.

Table 4.1. Preparation compositions for PPy/magnetite nanotubes.

	n	Pyrrole (mL)	$FeCl_3 \cdot 6H_2O$ (g)	Water (mL)	Methyl orange (mg)
PPy2.5	2.5	1.4	13.52	200	130
PPy6	6	1.4	32.45	200	130

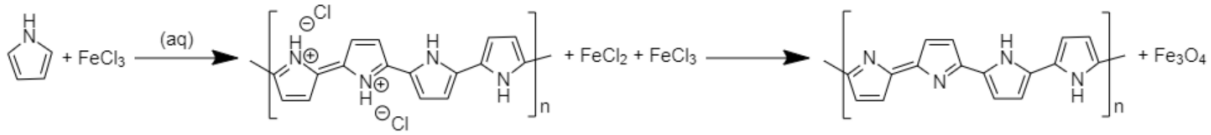

Figure 4.1 The two-step synthesis of magnetic nanotubes; PPy nanotubes are first created using the oxidation of the pyrrole with $FeCl_3 \cdot 6H_2O$. Excess amounts of $FeCl_3 \cdot 6H_2O$ lead to the creation of magnetite under alkaline conditions converting PPy to a base [7].

4.2 MRF-based electronic devices

Electrical devices with tunable parameters that utilize MRFs are on the rise [47]. Such a device was fabricated based on the PPy2.5 and PPy6 magnetic tubes which were dispersed in silicone oil with a volume concentration of 50 %. In short, several MRFs based on these particles and silicone oil were prepared. The device basically consists of an MRF that is sandwiched between two copper plates as shown and described in **Fig. 4.2a, b** in detail. The device is the connected with an RLC bridge and is placed inside a set-up that may impose static magnetic fields as shown and described in **Fig. 4.2 c**.

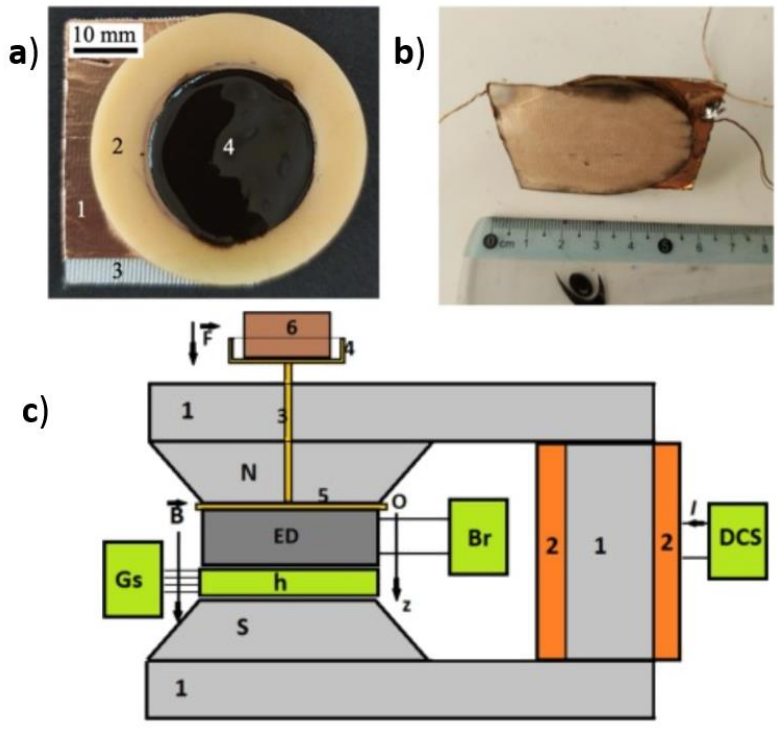

Figure 4.2 a) Top view of the electric device (ED) with 1 being the copper plate, 2 a natural rubber ring with diameter and thickness of 20 and 2 mm respectively, 3 is an insulating tape and 4 the MRF. b) The ED covered with the copper plates from both sides. c) The measuring set-up with 1 being the magnetic core, 2 copper coils connected to a DC source (DCS) for the production a magnetic field, 3-5 base for a load, 6 being an 800g load. The ED is connected to a power source (Br) [15].

It is possible to use a superimposed AC signal together with any combination of a static electric and magnetic fields. The MRF-based device acts as a capacitor with an equivalent resistance connected in parallel. The electrical properties of the MRF-based device can be measured under various conditions. When a static external electric field is applied, the particles can become electrically polarized and the whole MRF improves its dielectric properties. The distance of the dipoles is basically the distance between particles when the chain-like structure is formed. It is possible to alter this distance by varying the electric and magnetic fields, thus control the properties of the dielectric as a whole. The mechanism and how the external fields affect the interparticle distance is presented in **Fig. 4.3** in detail.

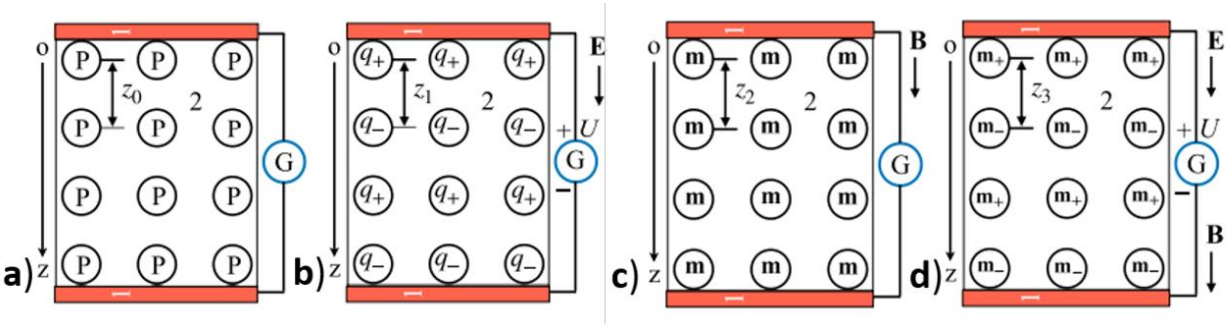

Figure 4.3 The MRF-based electric device under various conditions. a) No electric or magnetic fields are applied; the particles are considered to be randomly dispersed with an average distance between them z_0. b) Only an electric field is applied, the particles become electrically polarized and form column-like structures with an average distance between particles being z_1. c) Only an external magnetic field is applied and the particles are magnetically polarized with an average distance between them z_2. d) Simultaneous application of an electric and magnetic field. The average distance is now z_3 which is the shortest [48].

Fig. 4.4 displays the dependance of the equivalent resistance and capacitance for the same MRF, based on PPy6 particles at different frequencies and loads (a,b 1 Hz, 900 g, c,d 10 Hz, 800 g, constant impedance). For all samples the resistance has a decreasing tendency both with electric and magnetic fields. The resistance drops at a specific rate denoted by the fitted curves in **Fig. 4.4a**. The slope is independent of the magnetic field. In the given experimental window, the magnetic field has a higher impact for both samples when compared with the influence of the electric field with the resistance being half, at saturated fields. The capacitance has different trends. For the sample tested at 1 Hz **Fig. 4.4b**, the capacitance has a strong response both with the electric and magnetic fields. Unlike the resistance, the impact of the magnetic field depends on the electric field. For the sample measured at 10 Hz, the capacitance shows a completely different trend when compared to the 1Hz sample. The electric field is not particularly impactful and a good response is only observed when the magnetic field is altered. As can be seen by varying certain parameters, it is possible not

only to tune the electrical properties of these MRF-based devices but to obtain different trends. There are three extensive studies based on these MRF-based electrical devices with all the details [15, 48, 49].

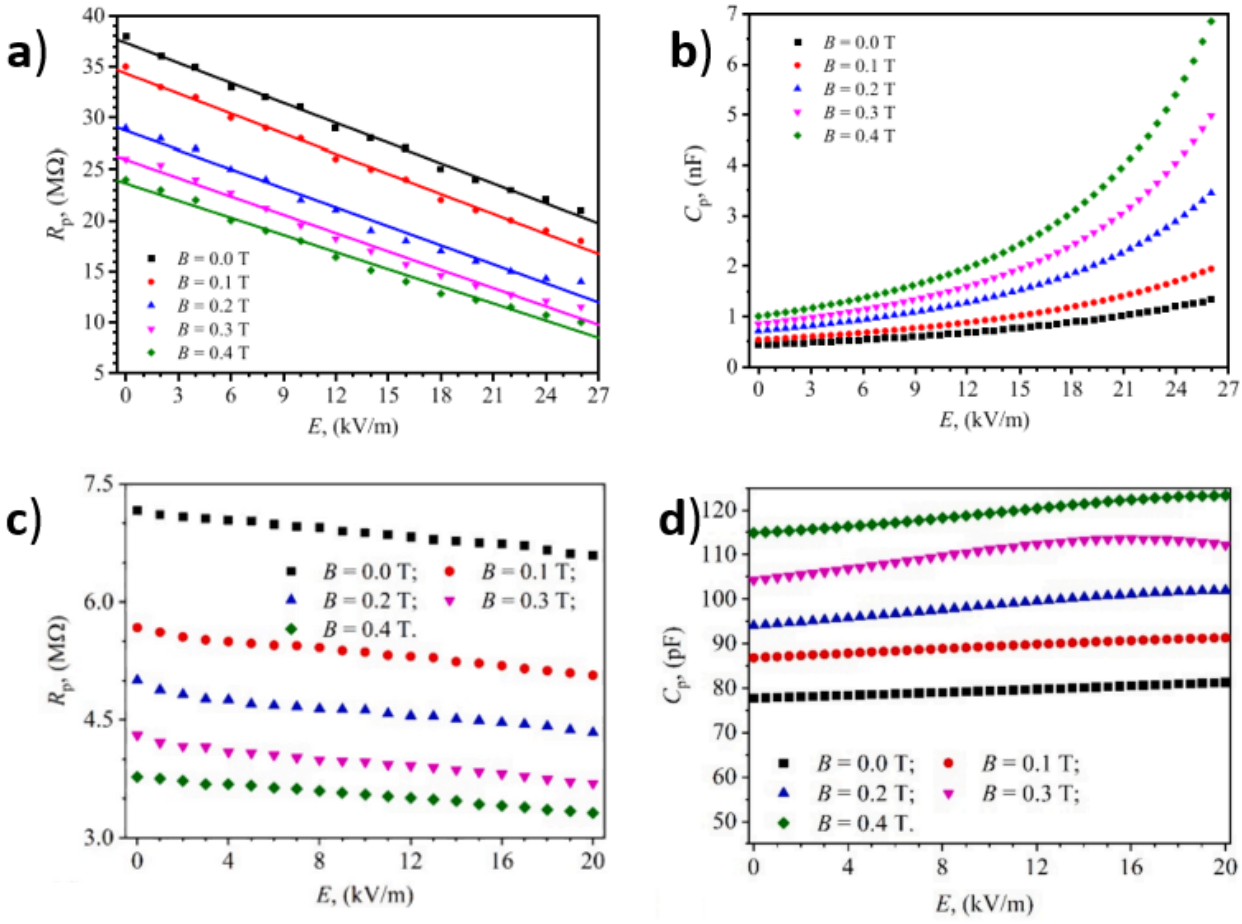

Figure 4.2 Capacitance and its equivalent resistance for an electric device at a,b) 1 Hz and 900 g load, and c,d) 10 Hz, 800 g load and constant impedance of 100 kΩ at the terminals of the RLC meter [15, 48].

4.3 Dimorphic MRFs

A dimorphic magnetorheological fluid (DMRF) is usually a three-component system composed of a conventional MRF and another type of magnetic or non-magnetic particles with a different morphology. For example, spherical and rod-like particles dispersed in an oil. There are only a handful of publications that include dimorphic MRFs, thus there is a large gap in the field to investigate [50, 51]. Moreover, to our knowledge, DMRFs based on magnetic nanotubes were not studied. Two different DMRFs were prepared with the characteristics presented in **Table 4.2**.

The MR effect of the samples at low and saturated fields is presented in **Fig. 4.5**. For both graphs the MRF 2.5 has overall inferior performance except at high frequencies in **Fig. 4.5a**. The MRF 6 on the other hand, shows similar

performance to the conventional MRF at saturated fields. However, at low fields, the MRF 6 outperforms the standard MRF by a considerable amount. The reason behind this observation was deemed to be the different types of magnetic particles. Despite having a much lower *Ms*, magnetite saturates at lower fields as was shown in **Fig. 2.1**.

Table 4.2 Composition of the prepared magnetorheological fluids in vol%.

	Code name		
Components	MRF 2.5	MRF 6	Standard MRF
Carbonyl iron	10	10	10
PPy2.5	1	0	0
PPy6	0	1	0
Silicone oil	89	89	90

Thus, the chain-like structures formed at the lower fields are more robust giving rise to a better MR effect. This is very important as less powerful fields are required to reach a better MR effect, thus less energy consumption is needed.

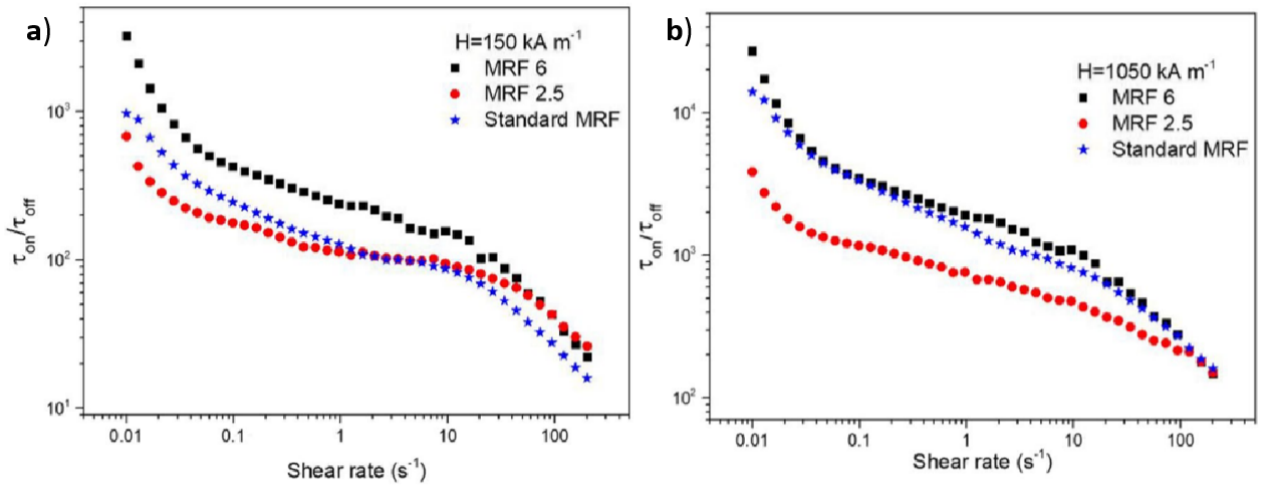

Figure 4.5 MR effect of various DMRFs compared to a standard MRF at different shear rates and magnetic fields a) 150 kA/m, b) 1050 kA/m [7].

The DMRFs were also tested at elevated temperatures through step-wise test with the MRF 6 sample shown in **Fig. 4.6a**. To be precise, the samples were subjected to a steady shear and the magnetic field was turn on and off repetitively with the field being constantly increasing between steps. At 60 °C the chains remain robust and the on-state shear stress is only slightly reduced when compared with the

shear stress at room temperature. However, during the off-state the viscosity is more temperature dependent which leads to a considerably lower shear stress. The average of all shear stress points at a given period is used to calculate the MR effect in **Fig. 4.6b** where all samples are compared. Key findings include that the MR performance is affected by the temperature especially at saturated fields. The DMRFs have much higher MR effects when compared to the standard MRF which is very impressive as only 1 vol% of nanotubes was added. The study includes the investigation of the effect of the nanotubes on the sedimentation stability, *Mn* and other key properties for magnetorheology [7].

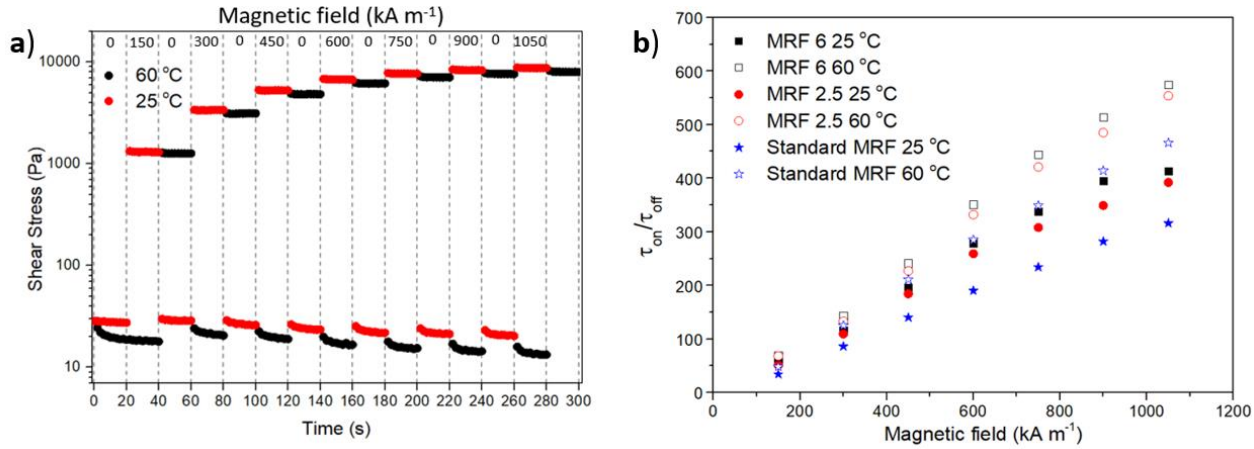

Figure 4.6 a) Effect of the step-wise increase of the magnetic field on the shear stress under a steady shear of 50 s^{-1} at different temperatures for the MRF 6. Changes of the magnetic field are illustrated with dotted lines with the values noted on top. The sample at 25 °C is shifted by 20 seconds for clarity reasons. b) MR effect at different magnetic fields for different MRFs at room temperature and 60 °C [7].

4.4 Recyclable MREs

One of the most commonly used matrices in MREs is silicon rubber due to its liquid state in which the magnetic particles can be dispersed homogeneously before curing. However, such elastomers cannot be recycled. In this section the possibility of reprocessing of MREs is showcased. The matrices are prepared through compression moulding using a polyurethane-based thermoplastic elastomer and CI particles, at different concentration, which are mixed prior inside a compounder. The samples were used in various tests, then they were recycled and tested again with this process being repeated three times with all the details included in the published paper [52]. As can be seen in **Fig. 4.7**, results show that in terms of mechanical properties both of the MREs and the pure elastomer managed to keep overall the same properties even after three reprocessing cycles. The tensile strength and the elongation at break are slightly reduced for every cycle; however, considering that in applications usually only one third of recycled material is used, these are very satisfying results. Only the after being recycled

three times (R3), the reprocessed MRE sample started to show noticeable changes. On the other hand, as shown in **Fig 4.7b**, the values of the Young's modulus were only sustained for the pure elastomer with the MRE showing a degrading trend with each reprocessing cycle.

The magnetorheological properties of these samples were also examined. For samples with a low content of CI particles, no MR effect was observed as the elastomer is too stiff for the particle to move.

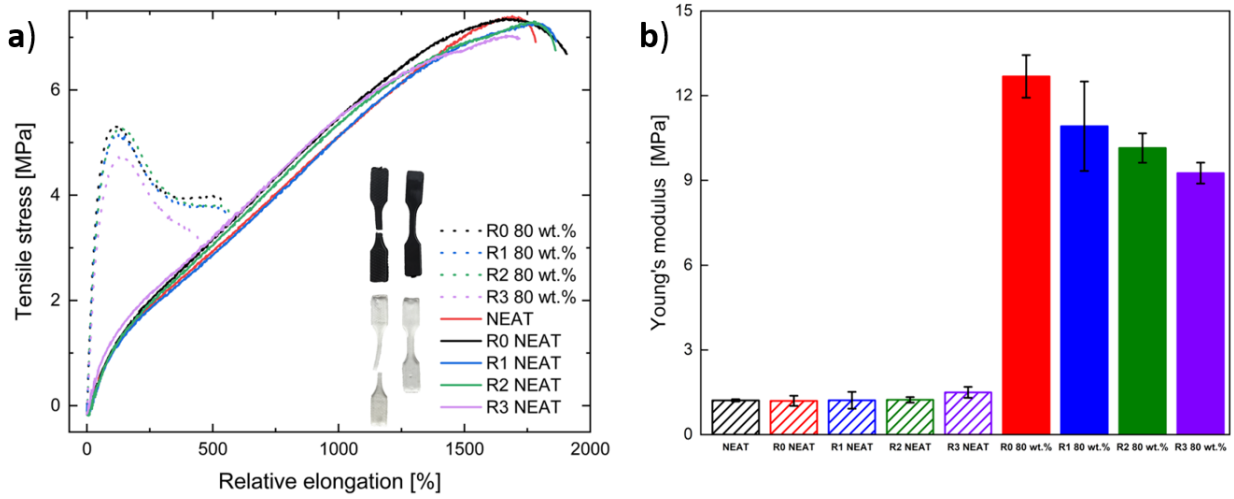

Figure 4.3 a) Tensile tests for a reprocessed thermoplastic MRE with 80 wt% filling and their pure analogs. b) the Young's modulus of the same samples. R0-R3 indicate the preprocessing cycle i.e. R0 the first sample, R1 once reprocessed sample etc. [52].

For the 80 wt% MREs, there was also no MR effect with the reasons explained in detail in the following **section 4.5**. Only for samples with a 50 wt% filling an MRE effect was observed and only for the non-reprocessed ones. This is demonstrated through dynamic strain sweeps in **Fig. 4.8a** where the *G'* increases with increasing magnetic fields within the LVE. The MR effect of the corresponding samples is shown in **Fig. 4.8b** and it must be noted that it is defined as the ratio of the difference between the *G'* of the on- and off-state over the *G'* of the off-state thus it is expected to be much lower than the one defined from **Eq. 2.8**. The reprocessed MRE displays a typical dependence on the magnetic field as described in the **section 2.4**.

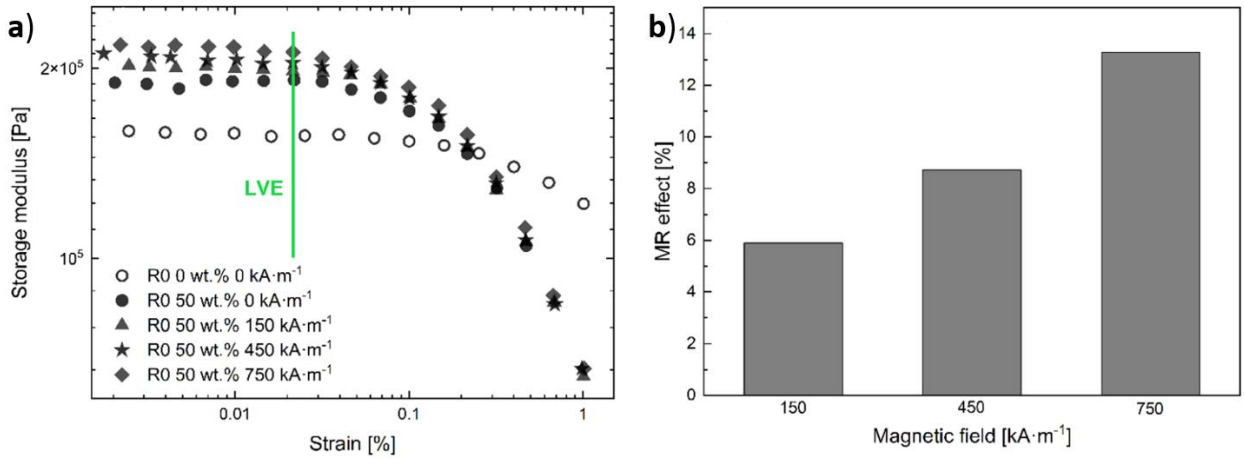

Figure 4.4 a) Dynamic strain sweeps for an MRE containing 50 wt% CI particles at different magnetic fields (filled symbols; circles 0 kA/m; triangles 150 kA/m; stars 450 kA/m; diamonds 750 kA/m); the neat matrix (unfilled) and (b) MR effect for the same 50 wt% matrix [52].

4.5 Particle-matrix interaction within MREs

As mentioned above, highly filled thermoplastic MREs did not display an MR effect while MREs with a less amount of filling did. This unexpected result was explained through the particle-matrix interactions during reprocessing. Dynamic time sweeps were performed to simulate the samples during reprocessing and they are shown in **Fig. 4.9**. For these measurements, the temperature was set to the processing one at 180 °C, and the sample was quickly loaded trimmed and measured. For the neat elastomer in **Fig. 4.9a**, a typical curve is extracted with the *G'* decreasing over time as the sample is heated and softens. The 30 wt% MRE shows the same decreasing trend for the first hour however, right after the *G'* is increased. The same elastomer is shown in **Fig. 4.9b** at a different scale together with the MRE with 80 wt% which shows a *G'* that is increasing for more than an order of magnitude. This increasement of *G'* has to do with the particle-matrix interactions. The thermoplastic elastomer is composed of polyurethane groups which can easily produce free radicals at the processing temperatures. Additionally, the CI particles are covered with a hydroxyl layer which can also produce radicals. Thus, a meeting of these radicals will result in a covalent bond which is demonstrated by the stiffening of the material. For the 30 wt% MRE, there are few particles and the softening due heating has a higher impact on the *G'*. However, after an hour the bonding process becomes dominant. For the 80 wt% particles on the other hand, the bonding formation is instantaneous and the amount of bonds is high enough to overcome the softening by a large amount. This explains why only the unprocessed sample displayed an MR effect. During the recycling processes the magnetic particles bond with the matrix and thus are not able to move and form any kind of structures.

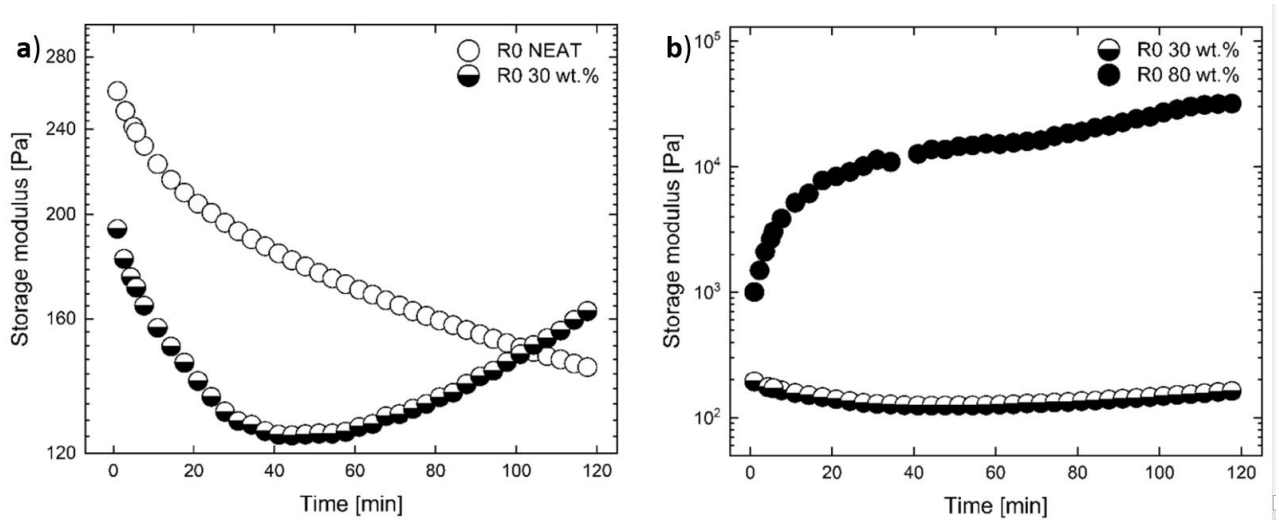

Figure 4.5 Dynamic time sweeps for (a) unprocessed pure elastomer (open circles) and the 30 wt% MRE (half open circles) and (b) 30 wt% MRE and the 80 wt% (filled circles) [52].

5. CONCLUDING REMARKS

5.1 Evaluation and summary of the Ph.D. goals

There were five general goals in total set for this Ph.D. study. The goals had to do with the marriage between the fundamental research of the MR systems with their applications. Each goal is evaluated separably as follows:

- Studies of various polypyrrole-based MRFs were conducted. In particular, the previous PPy nanotube synthesis methods are now optimized. Two types of PPy composites were prepared. The former include magnetite nanoparticles decorated on the PPy nanotubes in various concentrations. The amount of the magnetite nanoparticles can be easily manipulated through the solutes of the rection. The latter includes nickel microparticles coated with PPy nanoparticles. Both types of composites were extensively studied in MRFs.

- An investigation of the impact of the abovementioned magnetic nanotubes in conventional MRFs was conducted. Various types of the abovementioned PPy nanotubes (with higher or lower amounts of magnetite nanoparticles) were mixed in small amounts with a conventional CI-based MRF. The resulting MRF showed superior MR properties with a greater sedimentation stability.

- Several electrical devices composed of MRFs were prepared. The MRFs were composed of both the PPy nanotubes decorated with magnetite and nickel particles coated with PPy particles of different morphology. The electrical devices took advantage of the dual conductive and magnetic nature of these types of particles. The devices could be used both as a mean to characterize MRFs and as devices with tunable electrical properties.

- Recyclable MREs were prepared based on a thermoplastic polyurethane and CI particles. The mechanical properties were compared to the pure analogue elastomer and its recycled pallets. It was concluded that for an 100% recycled MRE, the material properties are not supressed significantly. Additionally, some of the other properties, such as the piezoresistivity, were preserved even after three reprocessing cycles however, the MR behaviour was only observed for some of the samples and only for a single reprocessing cycle due to the development of a covalent bonding between the particles and the matrix.

- During processing of MREs or when they are exposed to elevated temperature, the polymeric matrix may react with the surface of the magnetic particles. These interactions were studied for two types of elastomers including a polyurethane-based thermoplastic elastomer with numerous active groups that promote the particle-matrix interactions. The second elastomer was a polypropylene-based thermoplastic elastomer which has no active groups and theoretically, should show no signs of bonding. The particle-matrix interactions were mainly evaluated through rheology and proposed mechanisms were suggested.

- Most of the abovementioned studies are already published in Q1/Q2 impact factor journals, thus it can be said that the goals are generally achieved. The papers counted for this Ph.D. are the following:

  1) Anitas EM, **Munteanu A**, Sedlacik M, Bica I, Munteanu L, Stejskal J. Magnetic and electric effects in magnetorheological suspensions based on silicone oil and polypyrrole nanotubes decorated with magnetite nanoparticles. *Results in Physics*. 2024;61:107768.

  2) **Munteanu A**, Plachý T, Munteanu L, Ngwabebhoh FA, Stejskal J, Trchová M, et al. Bidisperse magnetorheological fluids utilizing composite polypyrrole nanotubes/magnetite nanoparticles and carbonyl iron microspheres. *Rheologica Acta*. 2023;62(9):461-72.

  3) **Munteanu A**, Ronzova A, Kutalkova E, Drohsler P, Moucka R, Kracalik M, et al. Reprocessed magnetorheological elastomers with reduced carbon footprint and their piezoresistive properties. *Scientific Reports*. 2022;12(1):12041.

  4) Jurča M, Vilčáková J, Kazantseva NE, **Munteanu A**, Munteanu L, Sedlačík M, et al. Conducting and magnetic hybrid polypyrrole/nickel composites and their application in magnetorheology. *Materials*. 2023;17(1):151.

5.2 Summary of the research work reports

A summary of the published papers in regards to the abovementioned goals is given below:

- **Article I** titled "Magnetic and electric effects in magnetorheological suspensions based on silicone oil and polypyrrole nanotubes decorated with magnetite nanoparticles"

Paper overview: Polypyrrole-magnetite composites-based magnetorheological fluids were prepared and used as parts of an electric device with tunable resistivity and capacitance.

Two MRFs composed of two different types of PPy nanotubes decorated with magnetite nanoparticles dispersed in silicone oil were investigated. One type of the nanotubes is more conductive while the second more magnetic. The MRFs were used as dielectric materials as part of an electrical device which operates in external magnetic and electric fields. The resistance and the capacitance of the device are then measured under external fields. The trends of the resistance and capacitates follow the dipolar approximation model. It was found that it is possible to tune the equivalent resistance and the capacitance by changing the values of the external electric and magnetic fields. The system responds better to magnetic fields allowing the capacitance and the resistance to be tuned much easier for the nanotubes with the highest amount of magnetite nanoparticles.

- **Article II** titled "Bidisperse magnetorheological fluids utilizing composite polypyrrole nanotubes/magnetite nanoparticles and carbonyl iron microspheres".

Paper overview: Evaluation of the MR performance and the stability of a dimorphic MRF based on CI microspheres and PPy-magnetite nanotubes.

In this work two types of magnetic PPy nanotubes which were decorated with different amounts of magnetite were synthesized using a new method. The method allows for nanotubes with tunable magnetic and electric properties to be synthesized. These nanotubes were mixed with a conventional CI-based MRF and this is the first study which investigates the combination of spherical and tube-like magnetic particles. The flow behaviour of the DMRFs was compared with a conventional MRF. The two systems showed similar flow-properties however, one of the DMRFs showed a higher stress increased during the on-state, especially at low magnetic fields. This was attributed to the faster magnetic saturation of the nanotubes over the CI-based particles. The experiments were performed also at elevated temperatures where it was proven that both DMRFs have a better MR response. Lastly, the stability of the systems was investigated with both DMRFs showing a greater sedimentation stability over the conventional MRF.

Author contribution: conceptualization, investigation, writing-original draft.

- **Article III** titled "Reprocessed magnetorheological elastomers with reduced carbon footprint and their piezoresistive properties".

Paper overview: A study of the mechanical and piezoresistive properties of thermoplastic MREs based on a polyurethane matrix after several reprocessing cycles and the interactions between the matrix and the magnetic particles.

This research presents a unique type of MRE which is able to be reprocessed several times while keeping the mechanical properties almost at the same level,

with just a ~10% reduction. In total three reprocessing cycles were performed with the material being destroyed and then recycled repetitively. The internal structure, MR performance and the piezoresistivity of these MREs and their pure analogues were evaluated. The MR effect was greatly supressed due to the new internal structure of the MRE which contained covalent bonds between the polyurethane matrix and the magnetic particles. The elastomers' molecular weight was reduced which seemed to the cause of the reduction in the mechanical properties. Surprisingly, the Payne effect was not spotted despite the MREs being highly filled. Lastly, the piezoresistivity tests showed a slight drop in the conductivity after each recycling process however, the changes did not significantly affect the final product. The study is significant as usually only one third of the reprocessed material are used however, this study showed a usable final product composed of 100% recycled materials.

Author contribution: conceptualization, investigation, writing-original draft.

- **Article IV** titled "Conducting and magnetic hybrid polypyrrole/nickel composites and their application in magnetorheology"

Paper overview: Synthesis of hybrid organic/inorganic composites with dual electrically conductive and ferromagnetic behaviour and their application in magnetorheology.

Under the presence of ammonium peroxydisulfate, it was possible to coat nickel microparticles with PPy in a globular and tube-like morphology. The conductivity of composites was in the order of 10^{-1} S cm^{-1} while the magnetic properties depended heavily on the content of nickel. The morphology of the coating played a small role in the conducting and magnetic properties of these particles. The globular composites with two different amounts of nickel were dispersed in a silicone oil and the magnetorheological properties of the system were then evaluated. Depending on the amount of nickel, the MR effect was found between 7–15 which was higher than other nickel-based MRFs from the literature.

Author contribution: investigation, writing, reviewing, and editing.

5.3 Contribution to science

There were several contributions to science through the papers published in this thesis. To be precise:

- An established synthesis method to prepare PPy nanotubes was used. However, several modifications were included which led to the diminish of the residual particles (not tubes) in the system after the synthesis and greatly improved the effective yield of PPy nanotubes.

- For the first time, a DMRF composed of magnetic particles with tube and spherical morphologies were studied.

- The effect of particles that start saturating at different fields was evaluated for the first time.

- For the first time, recyclable MREs with piezoresistive properties were prepared and studied.

- For the first time, the interactions between the filler and the matrix were investigated for MREs under processing conditions. Before these were only speculated. These findings can be easily implemented for any polymer composites.

- The "library of science" was enriched with various MRFs and MREs being included in terms of their mechanical, electrical and magnetic properties.

5.4 Future work

There are several current projects that are being finalized with the manuscripts being in their final states. These include:

- **Future Article I** titled "Processing-Induced Particle/Matrix Interactions in Magnetorheological Elastomers Based on Thermoplastic Matrix"

In this study, a detail investigation is performed on the interactions between the magnetic particles and a matrix of a thermoplastic MRE. The manuscript is finished and in the processed of being submitting before then end of 2024. A first authorship is expected.

- **Future Article II** titled "Tunable Electrical Conductivity of Nickel-Polypyrrole Microparticles Suspensions under Electric and Magnetic Fields"

This is a finished manuscript very similar with the ones explain in section 4.2 with a nickel-based MRF instead of the MRF 6 and MRF 2.5. Currently it is reviewed from the co-authors from University of Timisoara and it is expected to be submitted before the date of the Ph.D. defense. A co-authorship is expected from this study.

REFERENCES

1. Genc, S. and B. Derin, *Synthesis and rheology of ferrofluids: a review.* Current Opinion in Chemical Engineering, 2014. **3**: p. 118-124.
2. Kole, M. and S. Khandekar, *Engineering applications of ferrofluids: A review.* Journal of Magnetism and Magnetic Materials, 2021. **537**: p. 168222.
3. Shahrivar, K., et al., *Rheological behavior of magnetic colloids in the borderline between ferrofluids and magnetorheological fluids.* Journal of Rheology, 2019. **63**(4): p. 547-558.
4. Li, Y., et al., *A state-of-the-art review on magnetorheological elastomer devices.* Smart materials and structures, 2014. **23**(12): p. 123001.
5. Bastola, A.K., et al., *Recent progress of magnetorheological elastomers: a review.* Smart Materials and Structures, 2020. **29**(12): p. 123002.
6. Tang, X., et al., *Structure-enhanced yield stress of magnetorheological fluids.* Journal of Applied Physics, 2000. **87**(5): p. 2634-2638.
7. Munteanu, A., et al., *Bidisperse magnetorheological fluids utilizing composite polypyrrole nanotubes/magnetite nanoparticles and carbonyl iron microspheres.* Rheologica Acta, 2023. **62**(9): p. 461-472.
8. Zhu, X., X. Jing, and L. Cheng, *Magnetorheological fluid dampers: A review on structure design and analysis.* Journal of intelligent material systems and structures, 2012. **23**(8): p. 839-873.
9. Abd Fatah, A.Y., et al., *A review of design and modeling of magnetorheological valve.* International Journal of Modern Physics B, 2015. **29**(04): p. 1530004.
10. Sohn, J.W., G.-W. Kim, and S.-B. Choi, *A state-of-the-art review on robots and medical devices using smart fluids and shape memory alloys.* Applied Sciences, 2018. **8**(10): p. 1928.
11. Klingenberg, D.J., *Magnetorheology: Applications and challenges.* American Institute of Chemical Engineers. AIChE Journal, 2001. **47**(2): p. 246.
12. Phule, P.P., *Magnetorheological (MR) fluids: principles and applications.* Smart Materials Bulletin, 2001. **2001**(2): p. 7-10.
13. Bell, R., et al., *Influence of particle shape on the properties of magnetorheological fluids.* International Journal of Modern Physics B, 2007. **21**(28n29): p. 5018-5025.
14. Jang, I., et al., *Role of organic coating on carbonyl iron suspended particles in magnetorheological fluids.* Journal of applied physics, 2005. **97**(10).
15. Anitas, E.M., et al., *Magnetic and electric effects in magnetorheological suspensions based on silicone oil and polypyrrole nanotubes decorated with magnetite nanoparticles.* Results in Physics, 2024. **61**: p. 107768.

16. Fei, C., et al., *Preparation of magnetorheological fluid with excellent sedimentation stability.* Materials and Manufacturing Processes, 2020. **35**(10): p. 1077-1083.
17. Sedlacik, M., et al., *A dimorphic magnetorheological fluid with improved oxidation and chemical stability under oscillatory shear.* Smart Materials and Structures, 2013. **22**(3): p. 035011.
18. Sedlacik, M., et al., *Rheological properties of magnetorheological suspensions based on core–shell structured polyaniline-coated carbonyl iron particles.* Smart Materials and Structures, 2010. **19**(11): p. 115008.
19. Xu, L. and G. Zhou, *Enhancement of Magnetorheological Fluids with Size and Morphology—Optimized Fe3O4 Nanoparticles: Impacts on Rheological Properties and Stability.* Materials, 2024. **17**(12): p. 2838.
20. Tong, Y., X. Dong, and M. Qi, *High performance magnetorheological fluids with flower-like cobalt particles.* Smart Materials and Structures, 2017. **26**(2): p. 025023.
21. Morillas, J.R. and J. de Vicente, *Magnetorheology: a review.* Soft Matter, 2020. **16**(42): p. 9614-9642.
22. Bloemacher, D., *Carbonyl iron powders: Its production and new developments.* Metal powder report, 1990. **45**(2): p. 117-119.
23. Stejskal, J., et al., *Conducting and magnetic composites polypyrrole nanotubes/magnetite nanoparticles: application in magnetorheology.* ACS Applied Nano Materials, 2021. **4**(2): p. 2247-2256.
24. Wang, G., et al., *Rheological performances and enhanced sedimentation stability of mesoporous Fe3O4 nanospheres in magnetorheological fluid.* Journal of Molecular Liquids, 2021. **336**: p. 116389.
25. Kumar, J.S., et al., *A review of challenges and solutions in the preparation and use of magnetorheological fluids.* International journal of mechanical and materials engineering, 2019. **14**: p. 1-18.
26. Klingenberg, D.J., J.C. Ulicny, and M.A. Golden, *Mason numbers for magnetorheology.* Journal of Rheology, 2007. **51**(5): p. 883-893.
27. Böse, H., *Viscoelastic properties of silicone-based magnetorheological elastomers.* International Journal of Modern Physics B, 2007. **21**(28n29): p. 4790-4797.
28. Cvek, M., et al., *Reprocessing of injection-molded magnetorheological elastomers based on TPE matrix.* Composites Part B: Engineering, 2019. **172**: p. 253-261.
29. Norhaniza, R., et al., *Relationship between the response of microscopic and magnetic properties with highly uniform dispersion of carbonyl iron particles in magnetorheological polyurethane foam.* Smart Materials and Structures, 2020. **29**(11): p. 115012.
30. Han, Y., W. Hong, and L.E. Faidley, *Field-stiffening effect of magneto-rheological elastomers.* International Journal of Solids and Structures, 2013. **50**(14-15): p. 2281-2288.

31. Jolly, M.R., J.D. Carlson, and B.C. Munoz, *A model of the behaviour of magnetorheological materials.* Smart materials and structures, 1996. **5**(5): p. 607.
32. Malaescu, I., et al., *Investigations on the electrical conductivity and complex dielectric permittivity of a ferrofluid subjected to the action of a polarizing magnetic field.* Materials Research Bulletin, 2023. **164**: p. 112281.
33. Bica, I., et al., *Magnetostrictive and viscoelastic characteristics of polyurethane-based magnetorheological elastomer.* Journal of Industrial and Engineering Chemistry, 2019. **73**: p. 128-133.
34. de Vicente, J., *Magnetorheology: A review.* e-rheo-iba, 2013. **1**: p. 1-18.
35. De Vicente, J., D.J. Klingenberg, and R. Hidalgo-Alvarez, *Magnetorheological fluids: a review.* Soft matter, 2011. **7**(8): p. 3701-3710.
36. Ancey, C. and H. Jorrot, *Yield stress for particle suspensions within a clay dispersion.* Journal of Rheology, 2001. **45**(2): p. 297-319.
37. Zhu, H., Y. Kim, and D. De Kee, *Non-Newtonian fluids with a yield stress.* Journal of Non-Newtonian Fluid Mechanics, 2005. **129**(3): p. 177-181.
38. Morillas Medina, J.R., *Non-linear magnetorheology: Multibody and multipole effects on the yield stress.* 2019.
39. Li, W., X. Zhang, and H. Du, *Magnetorheological elastomers and their applications*, in *Advances in elastomers I: blends and interpenetrating networks*. 2013, Springer. p. 357-374.
40. Tong, Y., X. Dong, and M. Qi, *Payne effect and damping properties of flower-like cobalt particles-based magnetorheological elastomers.* Composites Communications, 2019. **15**: p. 120-128.
41. Mezger, T.G., *The rheology handbook*. Vol. 10. 2012: Vincentz Network Hannover, Germany.
42. Rubinstein, M. and R.H. Colby, *Polymer physics*. 2003: Oxford university press.
43. de Vicente, J., et al., *Effect of particle shape in magnetorheology.* Journal of Rheology, 2010. **54**(6): p. 1337-1362.
44. Morillas, J.R. and J. de Vicente, *Yielding behavior of model magnetorheological fluids.* Soft Matter, 2019. **15**(16): p. 3330-3342.
45. Morillas, J.R. and J. de Vicente, *Magnetorheology in saturating fields.* Physical Review E, 2019. **99**(6): p. 062604.
46. Bombard, A.J., et al., *Magnetorheology of dimorphic magnetorheological fluids based on nanofibers.* Smart materials and structures, 2014. **23**(12): p. 125013.
47. Bica, I. and E. Anitas, *Magnetic flux density effect on electrical properties and visco-elastic state of magnetoactive tissues.* Composites Part B: Engineering, 2019. **159**: p. 13-19.

48. Bica, I., et al., *Electrorheological and magnetorheological properties of liquid composites based on polypyrrole nanotubes/magnetite nanoparticles.* Smart Materials and Structures, 2024. **33**(6): p. 065007.
49. Bica, I., et al., *Electromagnetic modulation of conductance and susceptance in electrical devices based on silicone oil with polypyrrole–magnetite particle composites.* Journal of Materials Chemistry C, 2024. **12**(34): p. 13596-13608.
50. Jiang, W., et al., *Dimorphic magnetorheological fluid with improved rheological properties.* Journal of Magnetism and Magnetic Materials, 2011. **323**(24): p. 3246-3250.
51. Ngatu, G., et al., *Dimorphic magnetorheological fluids: exploiting partial substitution of microspheres by nanowires.* Smart Materials and Structures, 2008. **17**(4): p. 045022.
52. Munteanu, A., et al., *Reprocessed magnetorheological elastomers with reduced carbon footprint and their piezoresistive properties.* Scientific Reports, 2022. **12**(1): p. 12041.

LIST OF FIGURES AND TABLES

List of Figures

List of tables

LIST OF SYMBOLS AND ABBREVIATIONS

CI	Carbonyl Iron
DFS	Dynamic frequency sweep
DMRF	Dimorphic magnetorheological fluid
DSS	Dynamic strain sweep
DTS	Dynamic time sweep
ED	Electric device
LVE	Linear viscoelastic regime
MR	Magnetorheological
MRE	Magnetorheological elastomer
MRF	Magnetorheological fluid
b	Magnetic coupling parameter
e_r	Magnetorheological effect
G	Gravitational acceleration
G'	Storage modulus
G'_{off}	G' during the off-state
G'_{on}	G' during the on-state
G''	Loss Modulus
G^*	Complex modulus
H	Magnetic field
k_B	Boltzmann's constant
m	Magnetization of a dipole
M_m	Magnetization of the suspension
Mn	Mason number
Ms	Saturation magnetization
Mw	Polymer molecular weight
n_m	Viscosity of the continuous phase
Pe	Peclet number
PPy	Polypyrrole
R	Radius of a spherical particle
r	Distance between magnetic moments
T	Absolute temperature
T_g	Glass transition temperature
U	Dipole potential energy
u_s	Sedimentation velocity
$\dot{\gamma}$	Shear rate
γ_L	Critical strain
δ	Phase angle
η_{off}	Shear viscosity during the off-state
η_{on}	Shear viscosity during the on-state
Θ	Angle between magnetic moments
λ	Lamda parameter
μ_0	Permeability of free space
μ_m	Permeability of the continuous phase
V	Kinematic viscosity
ρ_p	Density of particles

ρ_s	Density of solvent
T	Shear stress
τ_{off}	Shear stress during the off-state
τ_{on}	Shear stress during the on-state
τ_y	Yield stress

CURRICULUM VITAE

Personal information	
Surname and name:	Munteanu Andrei
Contact:	munteanu@utb.cz
Current affiliation:	Centre of Polymer Systems, University Institute, Tomas Bata University in Zlín, trida T. Bati 5678, 76001 Zlín, Czech Republic
Nationality:	Hellenic and Moldavian
Date of Birth:	04. 08. 1994
Education	
Bachelor 2013-2018	Material Science, University of Crete
Masters 2018-2020	Material Science, University of Crete
Ph.D. 2020-present	Nanomaterials and Nanotechnology, Tomas Bata University

Projects

2020	Grant TBU IGA/CPS/2020/006
Member	The Influence of the Modification of Dispersed Particles on the Utility Properties of Magnetorheological Systems
2021	Grant TBU IGA/CPS/2021/003
Member	Piezorezistivity of Advanced Materials
2022	Grant TBU IGA/CPS/2022/004
Principle investigator	Magneto-responsive Systems
2023	MŠMT DKRVO RP/CPS/2022/007
Member	Smart nanomaterials: from basics to application
2023	Grant TBU IGA/CPS/2023/004
Member	Stability of Magnetorheological Elastomers
2023-present	Czech Science Foundation 23-07244S
Member	Anisotropic Magnetorheological Elastomers with Controlled Electrical Properties
2024	MEYS INTER-EXCELLENCE II LUABA24039
Member	Development of magnetoactive elastomeric Surfaces with controlled wettability for functional Liquid Manipulation - SALMON

Conferences

2022	European Polymer Progress, Prague
Poster	Recycled Polymer Composites with Magnetic Properties
2023	International Congress on Rheology, Athens
Poster	Magnetorheology of Dimorphic Fluids: The Case of Nanotubes-Microspheres System

Mobility

April-May 2023	Johannes Kepler University Linz, Austria.

LIST OF PUBLICATIONS

According to the Web of Science:

1. **Munteanu A**, Ronzova A, Kutalkova E, Drohsler P, Moucka R, Kracalik M, et al. Reprocessed magnetorheological elastomers with reduced carbon footprint and their piezoresistive properties. Scientific Reports. 2022;12(1):12041.
2. Munteanu L, **Munteanu A**, Sedlacik M, Kutalkova E, Kohl M, Kalendova A. Zinc ferrite/polyaniline composite particles: Pigment applicable as electro-active paint. Journal of Industrial and Engineering Chemistry. 2022;115:440-8.
3. **Munteanu A**, Plachý T, Munteanu L, Ngwabebhoh FA, Stejskal J, Trchová M, et al. Bidisperse magnetorheological fluids utilizing composite polypyrrole nanotubes/magnetite nanoparticles and carbonyl iron microspheres. Rheologica Acta. 2023;62(9):461-72.
4. Jurča M, Vilčáková J, Kazantseva NE, **Munteanu A**, Munteanu L, Sedlačík M, et al. Conducting and magnetic hybrid polypyrrole/nickel composites and their application in magnetorheology. Materials. 2023;17(1):151.
5. Bica I, Anitas EM, Sedlacik M, **Munteanu A**, Munteanu L, Chirigiu LME, et al. Electromagnetic modulation of conductance and susceptance in electrical devices based on silicone oil with polypyrrole–magnetite particle composites. Journal of Materials Chemistry C. 2024;12(34):13596-608.
6. Bica I, Anitas EM, Sedlacik M, **Munteanu A**, Munteanu L, Chirigiu LME. Electrorheological and magnetorheological properties of liquid composites based on polypyrrole nanotubes/magnetite nanoparticles. Smart Materials and Structures. 2024;33(6):065007.

ACCEPTED MANUSCRIPTS

7. **Munteanu A**, Sedlacik M. Progress in Surface Functionalized Particle-based Magnetorheological Composites. 2023.
8. Anitas EM, **Munteanu A**, Sedlacik M, Bica I, Munteanu L, Stejskal J. Magnetic and electric effects in magnetorheological suspensions based on silicone oil and polypyrrole nanotubes decorated with magnetite nanoparticles. Results in Physics. 2024;61:107768.

SUBMITTED MANUSCRIPTS

9. Munteanu L, **Munteanu A**, Sedlacik M. Electrorheology a material open review. Progress in material science 2024

Viskoelastická odezva magnetoreologických suspenzí

Viscoelastic response of magnetorheological suspensions

Doctoral Thesis

Published by Tomas Bata University in Zlín

nám. T.G. Masaryka 5555, 760 01, Zlín

Edition: published electronically

Typsetting by: Andrei Munteanu, M.Sc.

This publication has not undergone any proofreading or editorial review.

Publication year: 2024

Paper 1

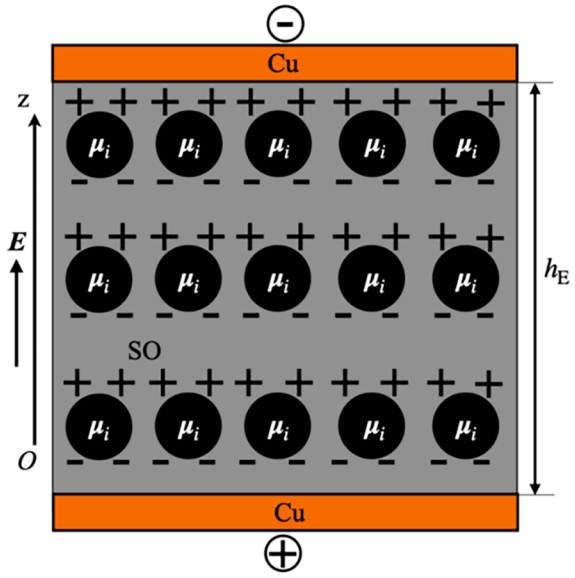

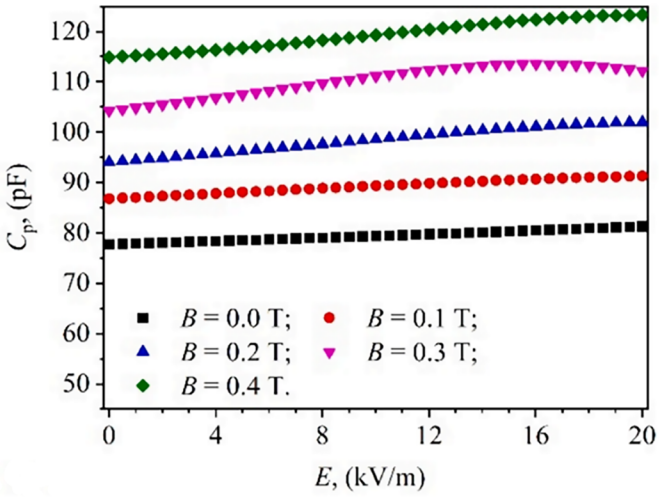

ELSEVIER
Results in Physics
Accepted 15th May 2024

Results in Physics 61 (2024) 107768

Contents lists available at ScienceDirect

Results in Physics

journal homepage: www.elsevier.com/locate/rinp

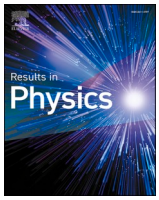

Magnetic and electric effects in magnetorheological suspensions based on silicone oil and polypyrrole nanotubes decorated with magnetite nanoparticles

Eugen Mircea Anitas [a,b], Andrei Munteanu [c], Michal Sedlacik [c,d,*,1], Ioan Bica [e], Lenka Munteanu [c], Jaroslav Stejskal [c]

[a] Horia Hulubei National Institute for R&D in Physics and Nuclear Engineering, Reactorului 30, RO-077125 Măgurele, Romania
[b] Joint Institute for Nuclear Research, Joliot Curie 6, 141980 Dubna, Moscow Region, Russia[2]
[c] Centre of Polymer Systems, Tomas Bata University in Zlín, Tr. T. Bati 5678, 76001 Zlín, Czech Republic
[d] Department of Production Engineering, Faculty of Technology, Tomas Bata University in Zlín, Vavreckova 275, 760 01 Zlín, Czech Republic
[e] West University of Timișoara, 4 V. Pârvan Ave., Timișoara 300223, Timiș County, Romania

ARTICLE INFO

Keywords:
Magnetorheological suspensions
Polypyrrole nanotubes
Magnetite nanoparticles
Relative dielectric permittivity
Dielectric loss factor
Active magnetic composites

ABSTRACT

In this work, two magnetorheological suspensions composed of polypyrrole nanorods decorated with magnetite nanoparticles and suspended in silicone oil were studied as electrical devices. The electrical devices (EDs) were fabricated in a unique cell using nanotubes with different magnetic and electric properties which can be tailored during synthesis. The electrical effects of the suspensions were studied under static electric and magnetic fields and were superimposed on a medium-frequency electric field. The electrical resistance Rp and the quality factor Qp at the terminals of EDs were extracted and analysed. Additionally, the equivalent electrical capacitances Cp were obtained through a well-established theory and then compared for each ED. Through the electrical and magnetic dipolar approximation model, it was illustrated that the electrical effect induced in a suspension can be three times higher depending on the amount of the magnetite. Thus, by tuning the synthesis parameters, it is possible to obtain EDs with well-defined and unique properties.

Introduction

Magnetorheological suspensions (MRSs) are colloidal intelligent materials consisting of magnetic microparticles which are dispersed in a non-magnetic carrier [1–4]. Under the influence of an external magnetic field, a magnetic phase is formed containing column-like aggregates which are oriented along the magnetic field lines [5,6]. In turn, this leads to a fast and reversible change of the material's mechanical and electrical properties, including magnetorheological [7,8], magneto-resistive [9] or magneto-dielectric (*MDE*) behaviour [10,11].

Numerous applications in various fields take advantage of the mentioned effects. The magnetorheological effect is mainly used in shock absorbers and mechanical vibrations [12–16], or in magnetically controllable clutches [17,18]. The MDE effect is a phenomenon in which the electrical capacitance or the relative dielectric permittivity are changed in the presence of a magnetic field. Well-known materials with good MDE properties are MRSs based on silicone oil (SO) and carbonyl iron (CI) microparticles [9] or MRSs absorbed by cotton fabrics [10], for which the relative dielectric permittivity and the dielectric loss factor can be tuned by an external magnetic field.

Several types of magnetic particles are generally used for applications. However, when mixed in a solution such magnetic particles tend to sediment due to the high density mismatch [19]. A good solution would be to use rod or tube-like particles [20]. Their high free volume leads to high entropic repulsions which improves the stability of the solution. For tube-like magnetic particles especially, the literature is extremely limited [21]. For that reason, tube-like particles were selected. However, as mentioned above, good electric properties are also

* Corresponding author at: Centre of Polymer Systems, Tomas Bata University in Zlín, Tr. T. Bati 5678, 76001 Zlín, Czech Republic.
E-mail addresses: eanitasro@gmail.com (E.M. Anitas), munteanu@utb.cz (A. Munteanu), msedlacik@utb.cz (M. Sedlacik), ioan.bica@e-uvt.ro (I. Bica), strouhalova@utb.cz (L. Munteanu), stejskal@utb.cz (J. Stejskal).
[1] ORCID: 0000-0003-3918-5084.
[2] International Intergovernmental Organization.

https://doi.org/10.1016/j.rinp.2024.107768
Received 23 April 2024; Accepted 15 May 2024
Available online 18 May 2024

needed. Thus in this work, magnetic and conductive nanotubes are investigated as MDEs.

Another benefit of polypyrrole is its use in medical and environmental applications [22]. Environmentally friendly and low-cost MRSs have already been investigated. As an example, magnetically active membranes, consisting of honey, carbonyl iron, and silver microparticles, can be used for various biomedical applications since they allow a remote and magnetically induced release of the bioactive components [23]. For the case of electrical devices based on MRS with honey, the response occurs only upon the application of an external magnetic field. However, here by using PPMY particles, we expect that the response of the electrical device to occur both for external magnetic and electric fields something that other MDEs are lacking.

The aim of this work is twofold. Firstly, to show that it is possible for MRS based on SO and polypyrrole nanotubes decorated with magnetite nanoparticles to induce electro-magnetodielectric and electro-magnetoconductive effects, by using a medium-frequency electric field superimposed on static electric and magnetic fields. Secondly, to investigate which type of particles are responsible for these effects. To this aim, polypyrrole/magnetite (PPMY) nanoparticles were synthesised in two forms; PPMY6 and PPMY2.5 in accordance to the procedure described in Ref. [24]. Two MRSs, denoted MRS_1 and MRS_2 were prepared by using the same volume fractions of nanoparticles (PPYM6, and PPYM2.5, in the respective order), and SO. By using a measuring cell with a diameter of 20 mm and a height of 2 mm, two electrical devices (ED_1 and ED_2) are manufactured.

The electrical resistance R_p and the quality factor Q_p are measured at the terminals of the devices. Following, equivalent electrical capacitance C_p of each device is extracted from the obtained data. Further, C_p and R_p are used to determine the magneto-dielectric, magneto-electro-conductive (MCE), as well as electro-magnetodielectric and electro-magnetoconductive effects in the obtained suspensions. It is shown that the electro-magnetodielectric effects, and respectively the electro-magnetoconductive effects of MRS_1 are up to about three times higher as compared to MRS_2.

Experiment

Materials

The following materials were used for fabrication of MRSs; silicone oil (SO, MS 100 type produced by Silicone Commerciale SpA, Italy). The density of SO is $\rho_{SO} = 0.98$ g cm^{-3} and the kinematic viscosity is $\nu = 100$ cSt at 25 °C. The relative dielectric permittivity at the frequency $f = 100$ kHz and the same temperature is $\varepsilon_r = 2.8$. This type of SO can be used in a wide range of temperatures, from −55 °C up to 220 °C.

For the magnetic nanoparticles, a two-step synthesis was performed to obtain two kinds of nanotubes. The codenames of PPMY6 and PPMY2.5 were selected to emphasize the molar ratio of $FeCl_3{\cdot}6H_2O$ over pyrrole which was used to make each type of nanotubes. A detailed description of the synthesis is provided in our previous work Ref. [24].

The morphology of the nanoparticles was studied by scanning electron microscope (SEM) NOVA NanoSEM 450 (FEI, The Netherlands) and shown in Fig. 1. As can be seen, the tube-like shape was confirmed for both types of particles and the higher molar ratio of $FeCl_3{\cdot}6H_2O$ resulted in increased amount of magnetite covering the polypyrrole tubes (Fig. 1a) [24]. Regarding the size of both particles, the tubes appear to be approximately around 1–3 μm in length and diameter in a nanometer range. In magnetorheological fluids based on iron oxide nanorods, the larger the size of the nanorods resulted in a higher performance of the fluids [25].

The PPMY6 and PPMY2.5 nanoparticles, having remanent electrical polarization, form millimetric-size agglomerates with different morphology and a high degree of polydispersity, as shown in Fig. 2. In order to decrease the polydispersity degree, the agglomerates have been partially redispersed using a friction bowl with pestle, for about 15 min per sample.

The obtained particles P_1 and P_2 (Fig. 3a and 3b) have smaller sizes: the average diameter of P_1 is 12.55 μm and a standard deviation of 4.37 μm, and the average diameter of P_2 is 13.60 μm and a standard deviation of 4.14 μm, obtained by a fit with a lognormal distribution, as shown in Fig. 3c and 3d. By measuring the volumes and masses of $_{P1}$ and P_2, the densities $\rho_1 = 0.32$ g cm^{-3}, and $\rho_2 = 0.27$ g cm^{-3} respectively were extracted. The suspensions MRS_1 and MRS_2 were prepared by manual mixing of 1.5 cm^3 of SO and 1.5 cm^3 of P_1, and respectively P_2 microparticles, for about 10 min, in a 25 mL Berzelius glass.

The magnetization curves of the PPMY6 and PPMY2.5 nanoparticles have been obtained by a vibrating-sample magnetometer (VSM, Model 7407, USA) with the intensity of the magnetic field ranging from –796 to + 796 kA m^{-1} at room temperature. The results are shown in Fig. 4. As can be seen in Fig. 4a, PPMY6 show superior magnetization M_{SP}, exceeding 61 A m^2 kg^{-1}, in comparison to their counterpart which

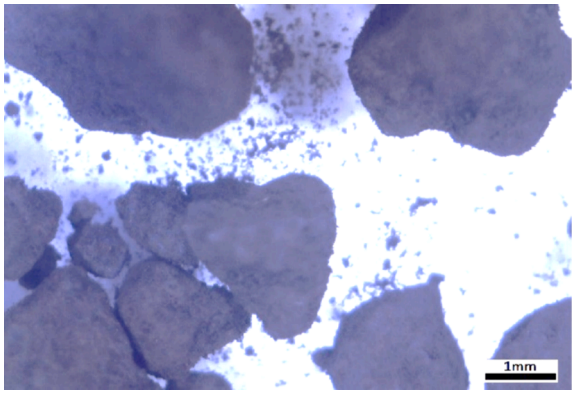

Fig. 2. The morphology of PPMY6 microparticles, obtained using a digital microscope. PPMY2.5 have a similar morphology.

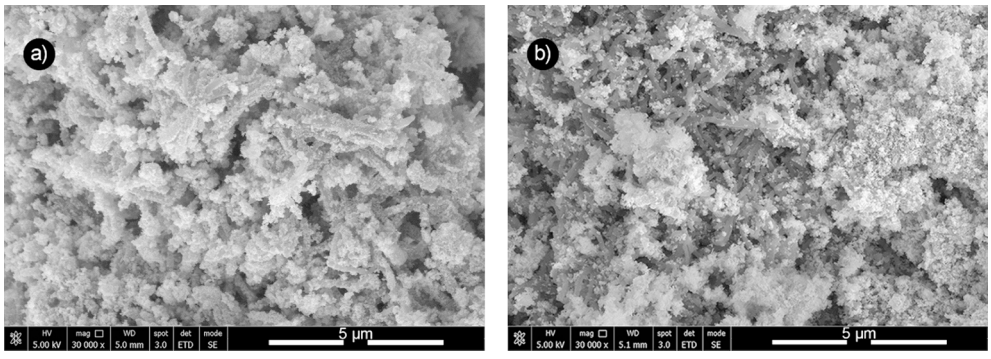

Fig. 1. The morphology of PPMY6 (a) and PPMY2.5 (b) evaluated by SEM.

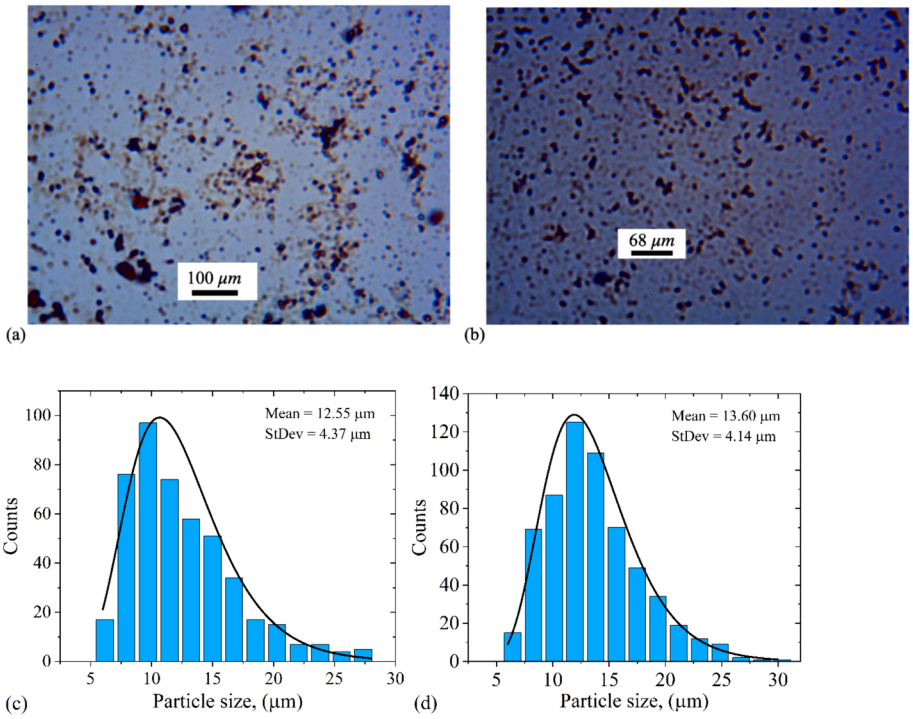

Fig. 3. Microparticles P_1 (a), and P_2 (b) visualized in transmission mode, by using OPTIKA microscope (made in Italy). The corresponding histograms of the equivalent diameters (blue bars) and the fit with a lognormal distribution function (black curve) for P_1 (c) and P_2 (d). (For interpretation of the references to colour in this figure legend, the reader is referred to the web version of this article.)

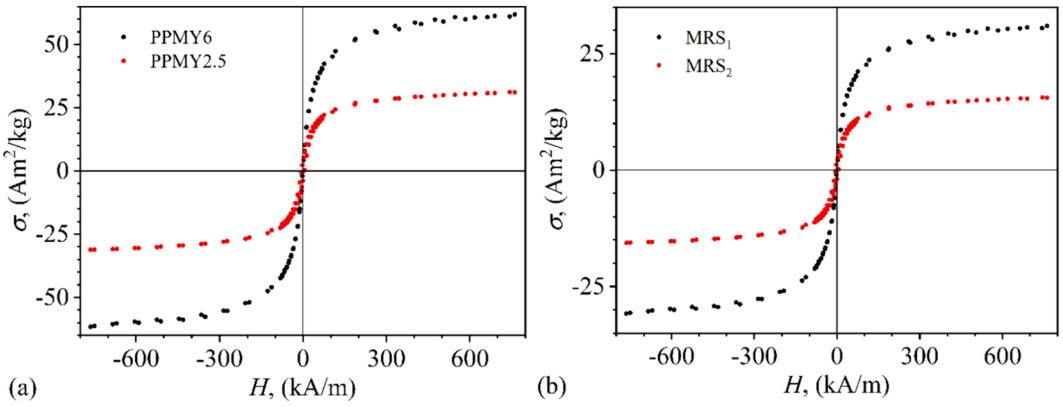

Fig. 4. The relative magnetization σ function of the intensity H of the magnetic field, for: a) particles PPMY6 and PPMY2.5; b) suspensions MRS_1 and MRS_2.

peaked at 31 A m^2 kg^{-1}. This indicates that especially PPMY6 particles are promising also for magnetorheological suspensions [24].

It is known that between the saturation magnetization M_{SP} of the particles and the saturation magnetization M_{MRS} of the suspensions, the following relationship holds: $\mu_0 M_{MRS} = \Phi_P \mu_0 M_{SP}$, [21], where μ_0 is the magnetic constant of the vacuum and Φ_P is the volume fraction of the particles. Since the volume fractions of particles P_1 and P_2 in their respective suspensions are 50 %, then by using the above relation together with the magnetization curves of the particles form Fig. 4a, one obtains in Fig. 4b the magnetization curves of MRS_1 and MRS_2. Note that when compared to the pure particles, it is apparent that in suspension form, the overall magnetization is significantly lower, due to decreased concentration of the magnetic nanoparticles, which are responsible for the magnetic response.

Fabrication of electrical devices

The materials used for the manufacture of the devices are:

- A copper foil with electroconductive adhesive (FCua) in the form of a roll (Fig. 5a), was purchased from Fruugo (UK). The length of the copper foil is 20 m, the width is 20 mm and thickness is 0.05 mm. The adhesive side is covered with a paper layer with a thickness of 0.5 mm.
- A surgical tape (ST), Durapore 3 M type, was obtained from Help Net (Fig. 5b, pos. 1) in the form of a roll. The length of the tape is 9.5 m, the width is 50 mm and the thickness is 0.2 mm. The outer side of ST is non-adhesive (Fig. 5b, pos. 1), while the inner side is adhesive (Fig. 5b, pos. 2).
- A crystal protection film (F), was purchased from Office Direct (Romania), in A4 format. The thickness of the foil is 0.12 mm.

Fig. 5. (a) Copper foil (pos. 1). Paper band on the side with electroconductive adhesive. (b) Surgical tape roll (pos. 1). The adhesive side of the tape (pos. 2). (c) Natural rubber pad.

- A self-adhesive pad (Ba), purchased from Carboy with a diameter of 40 mm and thickness of 2 mm (Fig. 5c). The pad is made from natural rubber and can support a weight of up to 700 N.

The EDs were manufactured according to the following steps:

1. Two pieces with dimensions 45 mm × 40 mm were cut from the ST band and the F coil. The adhesive side of ST was placed on the foil F by pressing.
2. The copper foil was placed on the non-adhesive side of the assembly made during step 1 by pressing until the surface area of ST was covered. As a result, the components of the measuring cell MC (Fig. 6a) were completed.
3. A hole with a diameter of 20 mm was made with a steel drill in the pad from Fig. 5(c). This part was placed with the adhesive side on the copper side of the assembly obtained during step 2 (Fig. 6b). As such, the second component of the measuring cell MC (Fig. 6b) is made.
4. The suspensions were then poured on the copper side, as shown in Fig. 7a. Following, the electrical device ED_1 with MRS_1, and the device ED_2 with MRS_2 were completed by electrically insulating the copper sides through the ST using heating. Fig. 7b show the final configuration of the obtained ED.

Experimental setup

The overall configuration of the experimental installation is shown in Fig. 8 (pos 6). The setup was used to study the magnetic suspensions in a medium-frequency electric field superimposed on a static magnetic field and uniform mechanical tension forces. The installation consists of an electromagnet, a direct current source (DCS), RXN-3020D type from HAOXIN (China), an RLC bridge Br, E720 type (Belarus), a gaussmeter Gs, DX-102 type from Dexing Magnets (China), a hall probe h, and a force application unit for the deformation of the device. The displacement unit is made of non-magnetic elements, and it consists of a shaft passing through the magnetic pole of the electromagnet and is mechanically coupled with a disk and a plate. The mass marked with a value of 800 g (Fig. 8) on the plate, is a lead disk. The ED and the probe h of the gaussmeter are fixed between the poles of the electromagnet utilizing a non-magnetic disk.

The working frequency f of the Br bridge is 10 kHz. The static magnetic field has magnetic flux density values B with a maximum of 420 mT, adjustable in steps of 30 mT. At the beginning, and during the measurements, the values of B were set within the limits of $\pm$ 2 %. The intensity E inside the EDs can be tuned in steps of 2 kV_{dc} m^{-1} up to a maximum value of 20 kV_{dc} m^{-1} by adjusting the voltage on the bridge.

Using the Br bridge, the parallel electrical resistance R_p and the quality factor Q_p of EDs are measured during the application of the magnetic field or the intensity of a static electric field. During the measurements, the impedance at the terminals of the RLC meter is fixed at 100 kΩ.

Experimental results, theoretical model and discussions

The effect of magnetic field $B \neq 0, E = 0$

The EDs are inserted one by one between the magnetic poles of the electromagnet. The resistance R_p and the quality factor Q_p of EDs are measured for magnetic flux density in the range $0 \leq B$ (mT) ≤ 420, periodically increased by steps of 30 mT in the absence of the static electric field. The recorded values are shown in Fig. 9.

Let us consider that nanoparticles P_1 and P_2 are monodisperse-like and uniformly distributed in the SO matrix (Fig. 10a). In the presence of a magnetic field, they become magnetic dipoles oriented along the magnetic field lines in the form of parallel and equidistant chains (Fig. 10b). Then, two identical and neighbouring magnetic dipoles form an electrical microcapacitor electrically connected in parallel with an electrical microresistor.

Through the values of R_p and Q_p, the equivalent electrical capacitance C_p is calculated using the following well-known formula:

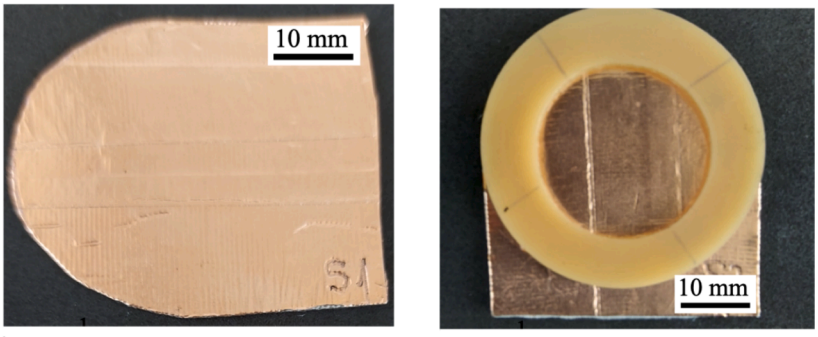

(a) (b)

Fig. 6. The components of the measuring cell MC. (a) Copper foil. (b) Natural rubber ring on top of the copper foil.

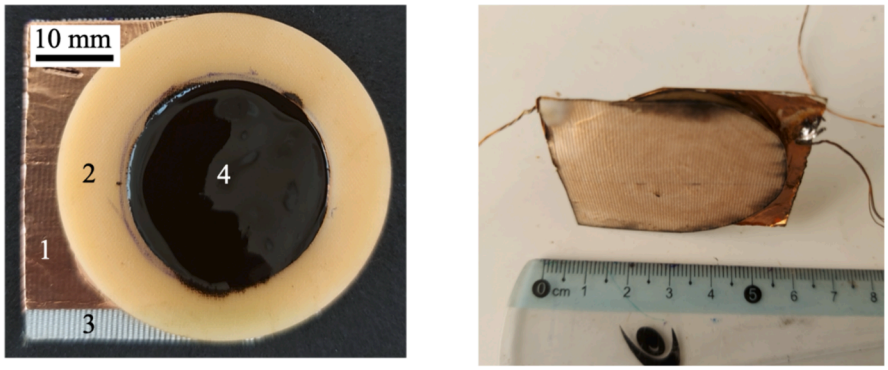

Fig. 7. (a) Subassembly with MRSs. (b) The end configuration of ED. 1 – copper foil, 2 – natural rubber ring with a diameter of 20 mm and thickness of 2 mm, 3 – ST band with non-adhesive surface, 4 – MRSs.

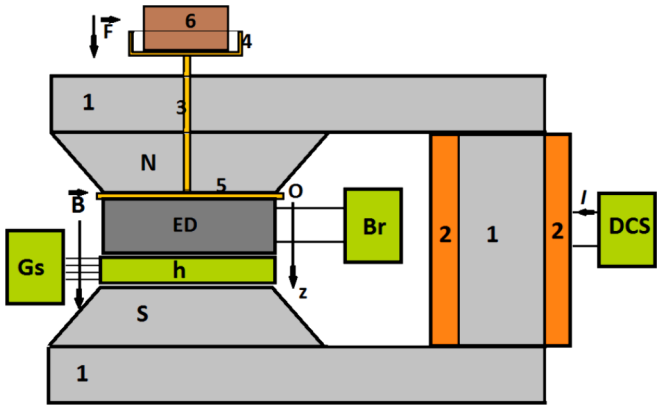

Fig. 8. Experimental setup (overall configuration): 1 – magnetic core, 2 – coil, 3 – non-magnetic spindle, 4 – non-magnetic plate, 5 – non-magnetic disk, 6 – non-magnetic marked mass, N and S – magnetic poles, ED – electrical device, Br – RLC bridge, Gs – gaussmeter, h – hall probe, DCS – continuous current source, Oz – coordinate axis, $\boldsymbol{B}$ – magnetic flux density vector, $\boldsymbol{F}$ – force vector, I – intensity of electric current.

$$C_{\mathrm{p}} = \frac{Q_{\mathrm{p}}}{2\pi f R_{\mathrm{p}}}, \tag{1}$$

Using the parameters mentioned in the experimental setup the above-mentioned formula can be rewritten:

$$C_{\mathrm{p}}(pF) \simeq \frac{16 Q_{\mathrm{p}}}{R_{\mathrm{p}}(\mathrm{M\Omega})}, \tag{2}$$

By using the variations $R_{\mathrm{p}} = R_{\mathrm{p}}\,(B)_{\mathrm{ED}}$ from Fig. 9a, and $Q_{\mathrm{p}} = Q_{\mathrm{p}}\,(B)_{\mathrm{ED}}$ from Fig. 9b, the variation of the capacitance can be deducted with the magnetic flux density, i.e. $C_{\mathrm{p}} = C_{\mathrm{p}}\,(B)_{\mathrm{ED}}$, as shown in Fig. 11a. The results in Figs. 9a and 11a suggest that EDs are real capacitors, whose equivalent electrical scheme consists of a resistor and a capacitor connected in parallel. In addition, R_{p} and Q_{p} decreases, and respectively increases with B, leading to an increase of the electrical conductivity.

Using the volume fractions of the magnetizable nanoparticles (representing the percentage of magnetizable particles in the MRS), from Ref. [26] it can be shown that the expressions for C_{p} and R_{p} can be written as:

$$C_p = \epsilon_0 \epsilon'_{MRS} \frac{S}{h_0}\left(1 - \frac{2.25\Phi S B^2}{\mu_0 k d}\right), \tag{3}$$

and

$$R_p = \frac{h_0}{S\sigma_0}\left(1 - \frac{2.25\Phi S B^2}{\mu_0 k d}\right), \tag{4}$$

respectively. Here, ϵ_0 is the vacuum dielectric constant, ϵ'_{MRS} the relative

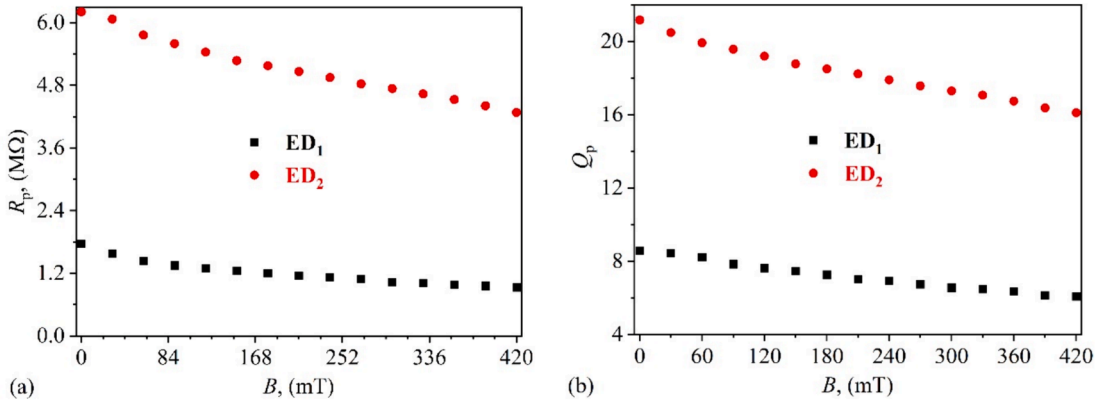

Fig. 9. Variation of the electrical resistance R_{p} (a) and of the quality factor Q_{p} (b) with the magnetic flux density B for ED_1 (black colour) and ED_2 (red colour). (For interpretation of the references to colour in this figure legend, the reader is referred to the web version of this article.)

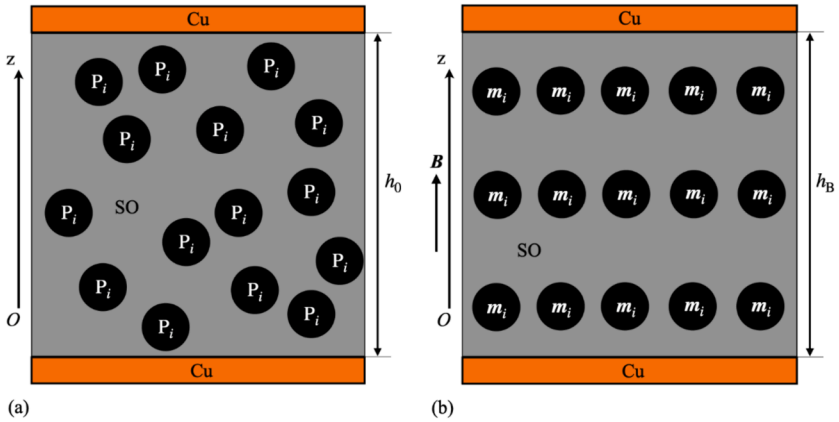

Fig. 10. Distribution of particles P_i (i = 1,2) in silicone oil (model) in the absence of a magnetic field (a), and respectively in the presence of a magnetic field (b). Here, $\boldsymbol{B}$ is the magnetic field density vector, $\boldsymbol{m}_i$ is the magnetic moment vector of particle P_i (i = 1, 2), Oz is the coordinate axis, h_0 and h_B are the distances between the copper plates (Cu) in the presence, and respectively in the absence of the magnetic field.

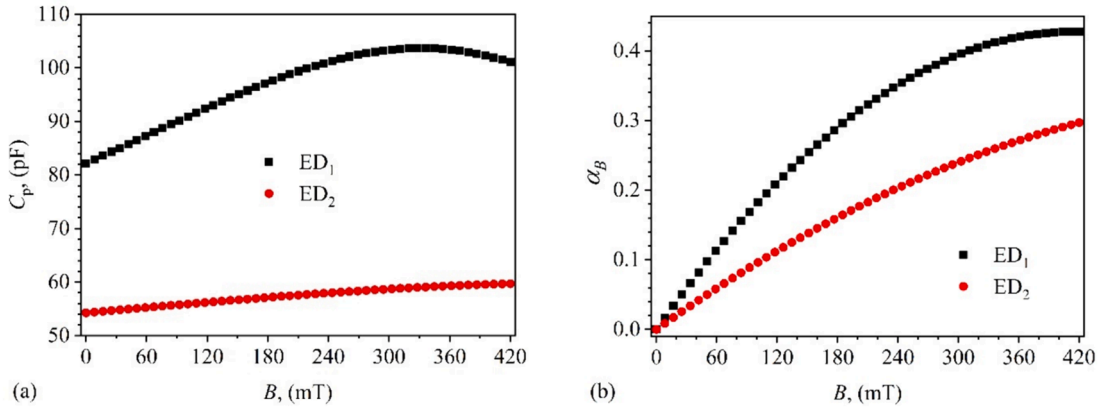

Fig. 11. Variation of the electrical capacitance C_p (a) and of the dimensionless quantity α_B (b) with the magnetic flux density B for ED_1 (black colour) and ED_2 (red colour). (For interpretation of the references to colour in this figure legend, the reader is referred to the web version of this article.)

dielectric permittivity of the suspensions, S represents the common surface area between the copper foil and MRS, h_0 refers to the thickness of MRS, Φ the volume fraction of nanoparticles inside MRS, μ_0 stands for the vacuum magnetic constant, k the deformability constant of the magnetic dipoles chain, d refers to the equivalent diameter of the magnetic dipoles, and equal to that of particles, and σ_0 is the electrical conductivity of MRS in the absence of the magnetic field.

Equations (3) and (4) show that the values of C_p and R_p are highly dependent on the magnetic flux density, in agreement with the experimental data from Fig. 9a and 11a. However, for the same values of the nanoparticles volume fractions, and for the same values of B, the values of R_p (Fig. 9a), and respectively of C_p (Fig. 11a) are different. According to the model given by Eqs. (3) and (4), the observed effect is due to the values of average diameters of the particles from MRS, and due to the values of the deformability constants of the magnetic dipole chains. In particular, an increase of either the average diameter or of the deformability constant leads to a less pronounced decrease of C_p and R_p with B.

To quantify the contribution induced by the diameters of magnetic dipoles and by the deformability constant of the chains they form, we introduce the magneto-deformation effect:

$$\alpha_B \equiv \frac{2.25\Phi S B^2}{\mu_0 k d}, \tag{5}$$

which describes the ratio between the deformation magnetic force of the magnetic dipole chains and the resistance force opposed by these chains. Therefore, by using Eqs. (4) and (5), α_B can be rewritten as:

$$\alpha_B = 1 - \frac{R_p}{R_{p0}}, \tag{6}$$

where $R_{p0} \equiv \frac{h_0}{S\sigma_0}$ is the resistance in the absence of the magnetic field.

By introducing in Eq. (6) the variation of resistance with magnetic flux density from Fig. 9a, variation of α_B with magnetic flux density is obtained, i.e. $\alpha_B = \alpha_B(B)$, as shown in Fig. 11b. The results show that α_B for P_1 particles is significantly higher when compared to P_2 particles. In particular, for $B \geq 300$ mT, α_B is about two times larger for P_1 microparticles, in agreement with the model of the magnetic dipole approximation and confirmed by the results obtained in [23,26,27].

The quantification of the type of nanoparticles on the behaviour of the capacitance and resistance is addressed by using the *MDE* and *MCE* effects, defined by:

$$MDE(\%) \equiv \left(\frac{C_p}{C_{p0}} - 1\right) \times 100, \tag{7}$$

and respectively by:

$$MCE(\%) \equiv \left(\frac{R_{p0}}{R_p} - 1\right) \times 100. \tag{8}$$

Thus, using the data from the capacitance and resistance from Fig. 9a, and 11a respectively, from the Eqs. (7) and (8), the variation of *MDE* and *MCE* are obtained, as shown in Fig. 12a, and respectively 12b. The

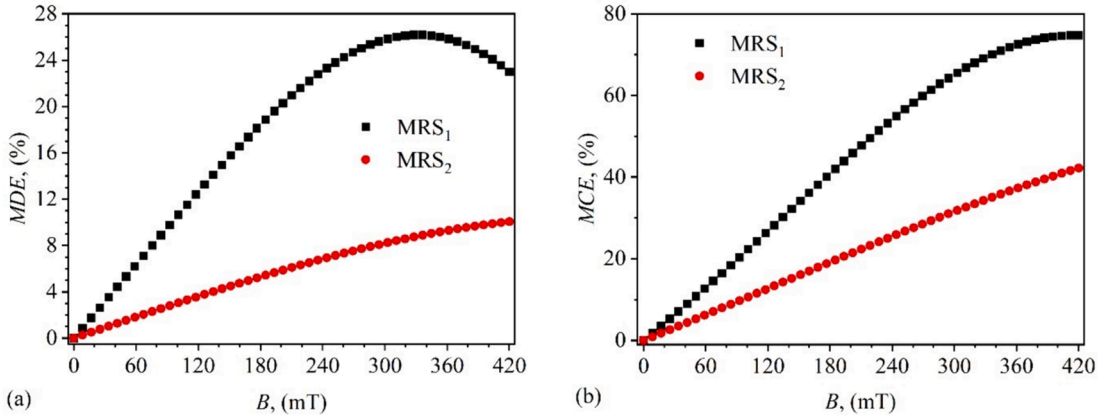

Fig. 12. Variation of the *MDE* (a) and of the *MCE* (b) with the magnetic flux density B for ED_1 (black colour) and ED_2 (red colour). (For interpretation of the references to colour in this figure legend, the reader is referred to the web version of this article.)

results indicate that the type of particles used can significantly influence the MRSs *MDE* and *MCE*. In particular, for $B > 0$, the contribution of the P_1 nanoparticles is higher if compared to P_2 nanoparticles, for both *MDE* and *MCE*. This is due to the different structure and stoichiometric composition of P_1 and P_2.

The observed effects resulted from the magnetization of the two types of particles (see Fig. 4b), as they are responsible for the occurrence of different magnetic forces, and thus for different magneto-deformations of the magnetic dipole chains in MRSs [24,27]. As a result of the interaction between the magnetic dipole chains, for P_1 particles, the resistance (Fig. 9a) and capacitance (Fig. 11a) induce the maximum at $B \simeq 340$ mT in *MDE* (Fig. 12a) and *MCE* (Fig. 12b). Through their proximity and the agglomeration process, the number of columns with electric microcapacitors and microresistors decreases. This leads to a decrease of resistance R_p and capacitance C_p, therefore changing the behaviour of *MDE* and *MCE* for MRS_1 sample.

The effect of electric field $\boldsymbol{B} = 0, \boldsymbol{E} \neq 0$

The quantities R_p and Q_p are measured as a function of the intensity E of a static electric field, and in the absence of magnetic field. Using the electric field, the samples were scanned from 0 to 20 kV m^{-1}, in intervals of 2 kV m^{-1}. The results are presented in Fig. 13a, and 13b respectively showing that EDs are equivalent, from an electrical point of view, to a resistor connected in parallel to a capacitor.

The electric field between the copper foils of EDs is uniformly distributed. As a result, the P_i, ($i = 1, 2$) particles obtain electrical charges q, thus becoming electrical dipoles. Within the volumes of MRSs, the quantity of charge can be expressed by [26]:

$$Q = \frac{6\Phi S q}{\pi d^2}. \tag{9}$$

Similarly to the magnetic dipoles, the electrical dipoles are oriented along the electric field lines, in the form of columns. This formation behaviour is illustrated in Fig. 14. We assume that these columns have equal lengths and are uniformly distributed in the MRS. In an electric field, the length h_0 of the columns becomes $h_E < h_0$ (as illustrated in Fig. 14).

By using the variations $R_p = R_p(B)$ and $Q_p = Q_p$ (B) from Fig. 9 in Eq. (2), the variation of capacitance $C_p = C_p(B)$ can be calculated as demonstrated in Fig. 15a. From the above assumptions and according to the model developed in Ref. [26], the length h_E can be calculated as:

$$h_E = h_0\left(1 - \frac{QE}{h_0 k_E}\right), \tag{10}$$

where k_E is the deformability constant of the electric dipole chains. Thus, by knowing h_E, we obtain the equivalent electrical capacitance of EDs in static magnetic field, as:

$$C_p = \frac{C_{p0}}{1 - \frac{QE}{h_E k_E}}, \tag{11}$$

where:

$$C_{p0} \equiv \frac{\epsilon_0 \epsilon'_{MRS} S}{h_0} \tag{12}$$

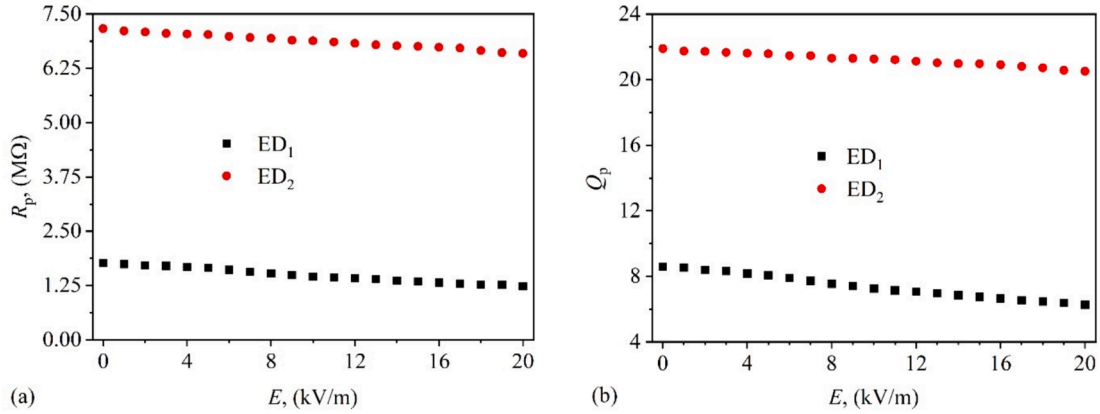

Fig. 13. Variation of the electrical resistance R_p (a) and of the quality factor Q_p (b) with the intensity E of a static electric field for ED_1 (black colour) and ED_2 (red colour). (For interpretation of the references to colour in this figure legend, the reader is referred to the web version of this article.)

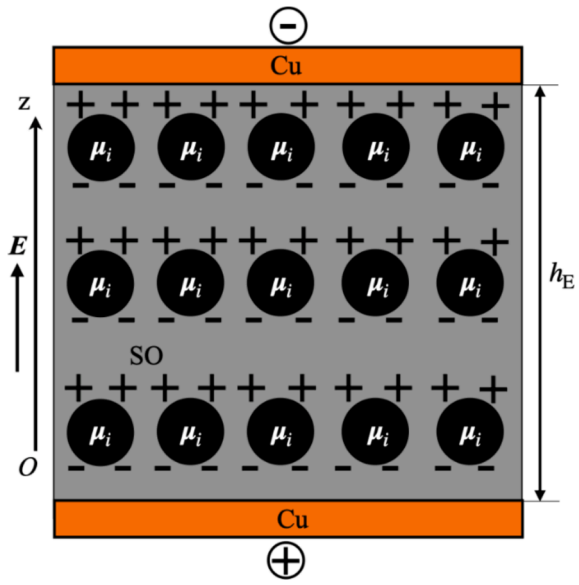

Fig. 14. Distribution of particles P_i (i = 1, 2) in silicone oil (model) in the presence of a static electric field. Here, E is the electric field intensity vector, $\boldsymbol{\mu}_1$ (i = 1, 2) is the electric moment, Oz is the coordinate axis, and h_E is the distances between the copper plates (Cu) in the presence, of the electric field. For the configuration without electric field, see Fig. 10a.

is the equivalent electrical capacitance of EDs in the absence of the electric field.

Similarly, the electrical resistance can be written as:

$$R_p = R_{p0}\left(1 - \frac{QE}{h_E k_E}\right), \tag{13}$$

where:

$$R_{p0} \equiv \frac{h_0}{\sigma_{MRS} S} \tag{14}$$

is the equivalent electrical resistance of EDs in the absence of electric field.

Equations (13) and (14) show that the values of the capacitance and resistance are greatly influenced by the values E of the intensity of the electric field, in agreement with experimental data from Figs. 9a and 11a. However, for the same volume fractions values of the particles, and for the same values of the intensity of the electric field, the values of C_p, and R_p are varied. According to the model given by Eqs. (13) and (14) the observed effects arise due to the values of the average diameters of the particles, as well as due to the deformability constants of the electrical dipole chains.

In order to quantify the contributions of these two factors, we introduce the electro-deformation effect:

$$\alpha_E \equiv \frac{QE}{h_E k_E}, \tag{15}$$

which describes the ratio between the electrical force of deformations of electrical dipole chains, and the resistance force opposed by the chains.

By combining Eqs. (13) and (15), one obtains α_E in the form:

$$\alpha_E \equiv 1 - \frac{R_p}{R_{p0}}. \tag{16}$$

Then, by using the variation of resistance from Fig. 11a in Eq. (16), the variation $\alpha_E = \alpha_E(E)$ can be obtained, as shown in Fig. 15b.

The results show that for $E > 0$, $\alpha_E(E)_{ED1} > \alpha_E(E)_{ED2}$. This effect arises due to the difference in the electrical polarization of particles P_1 and P_2, at a fixed value of intensity $E > 0$.

For the quantification of the contribution of the particles type to the capacitance and resistance, we introduce the relative contribution of the electric field, in the absence of the magnetic field, to the electrical capacitance (Λ_C) and to resistance (Λ_R), as:

$$\Lambda_C(\%) = \left(\frac{C_p}{C_{p0}} - 1\right) \times 100, \tag{17}$$

and respectively:

$$\Lambda_R(\%) = \left(\frac{R_{p0}}{R_p} - 1\right) \times 100. \tag{18}$$

Then, by using the variation of the capacitance (Fig. 11a) and of the resistance (Fig. 9a), the variations $\Lambda_C = \Lambda_C(E)$, and $\Lambda_R = \Lambda_R(E)$ are obtained as shown in Fig. 16a and 16b respectively. The results show that Λ_C and Λ_R have a quasi-linear increase with E, while $\Lambda_{C_{MRS1}} > \Lambda_{C_{MRS2}}$ and $\Lambda_{R_{MRS1}} > \Lambda_{R_{MRS2}}$ for $E > 0$. These effects can be correlated to the different values of the modulus of the electrical polarization vector, and the electrical conductivities of particles P_1 and P_2 [26] due to the accumulation of electrical charges in the volume of MRS and due to the electro and magneto-deformations of the column dipoles. In turn, this leads to an increase of the electrical conductivity and capacitance.

The combined effect of the electric and magnetic fields $\boldsymbol{B} \neq 0, \boldsymbol{E} \neq 0$

The EDs are introduced in a static electric field superimposed over a static magnetic field and an electric field of frequency $f = 10$ kHz with an effective value of $u = 1V_{ef}$. The intensity of the static electric field is

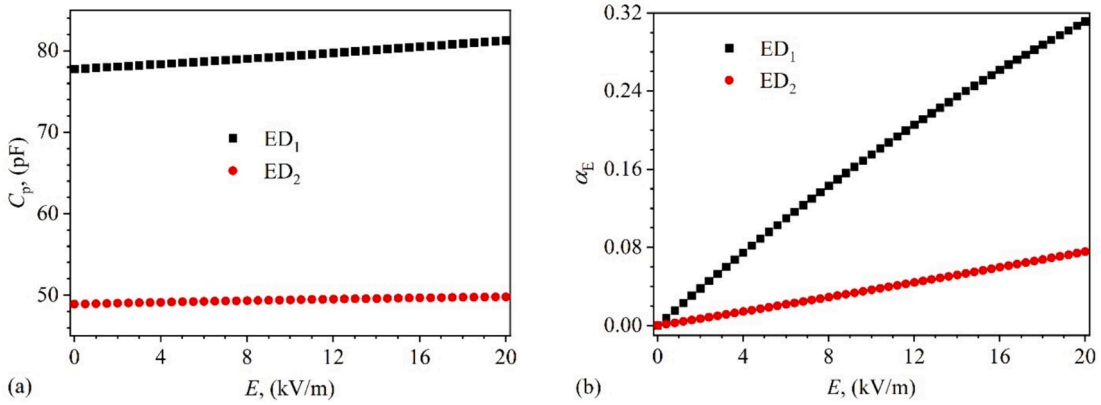

Fig. 15. Variation of the electrical capacitance C_p (a) and the quantity α_E (b) with the intensity E of a static electric field for ED_1 (black colour) and ED_2 (red colour). (For interpretation of the references to colour in this figure legend, the reader is referred to the web version of this article.)

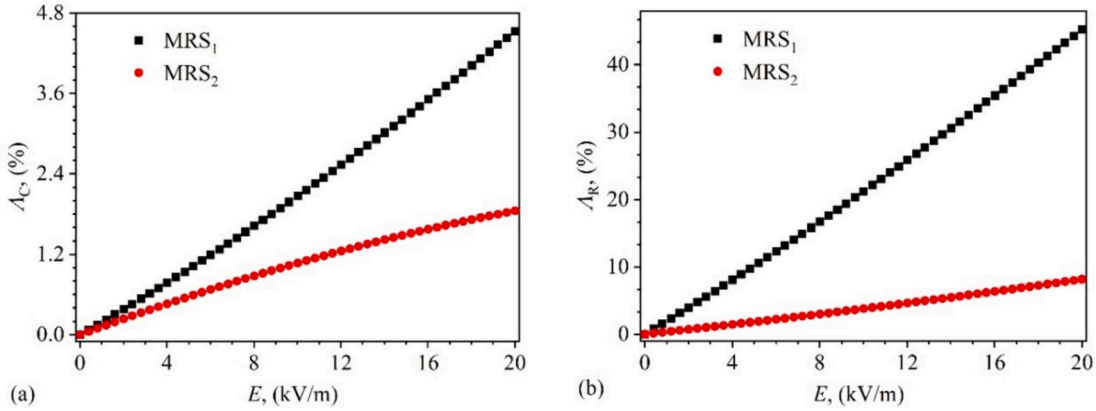

Fig. 16. Variation of Λ_C (a) and Λ_R (b) with the intensity E of a static electric field for MRS_1 (black colour) and MRS_2 (red colour). (For interpretation of the references to colour in this figure legend, the reader is referred to the web version of this article.)

steadily increased from 0 to 20kV m^{-1} in steps of 2 kV m^{-1}. The static magnetic field is also altered within the range of 0 and 0.4 T in steps of 100 mT. R_p and Q_p are measured during the application of the electric and magnetic fields. The obtained values for ED_1 and ED_2 are presented in Figs. 17 and 18, respectively. The results show that for both devices R_p (and Q_p) decrease with increasing values of the electric field in agreement with Eq. (13). When the electric field is fixed, R_p and Q_p decrease with increasing values of the magnetic field. Thus, R_p and Q_p are greatly influenced by the static electric and magnetic fields superimposed on a medium-frequency electric field.

Using the data from Figs. 17 and 18 in Eq. (2) the capacitances of ED_1 and ED_2 can be obtained, as shown in Fig. 19a, and b.

The results show that for fixed values of magnetic field, the capacitance has a quasi-linear increase with the electric field, in agreement with Eq. (11). Similarly, considering the fixed values of electric field, the capacitance increases significantly with increasing magnetic field, in agreement with Eq. (3). However, for fixed values of magnetic field the contribution of P_1 particles to the capacitance is two times larger when compared to P_2 particles. The effect is due to the high magnetic and electric polarization of P_1 particles compared to P_2 particles.

The quantification of the contribution of these fields, to the values of the relative dielectric permittivity of MRSs is examined by introducing the electro-magnetodielectric effect β_C, defined as:

$$\beta_C(\%) = \left(\frac{C_p(E)_B}{C_p(E)_{B=0}} - 1\right) \times 100, \tag{19}$$

where $C_p(E)_B$ is the capacitance when $E \neq 0$ and $B \neq 0$, and $C_p(E)_{B=0}$ is the capacitance when $E \neq 0$ and $B = 0$ T. By using the variation of the capacitance from Fig. 19, the variation of the electro-magnetodielectric effect can be evaluated, as shown in Fig. 20. The results show that for fixed values of field, the β_C increases for higher values of the magnetic field. Increasing both fields, leads to the agglomeration of dipole columns [26], which in turn results to a change of the shape of functions $\beta_C = \beta_C(E)$.

The quantification of the contribution of the static electric and magnetic fields superimposed on the medium-frequency electric field, to the electrical conductivities of MRSs is performed by introducing the electro-magnetoconductive quantity β_R, defined as:

$$\beta_R(\%) = \left(\frac{R_p(E)_{B=0}}{R_p(E)_B} - 1\right) \times 100, \tag{20}$$

where $R_p(E)_{B=0}$ is the resistance when $E \neq 0$ and $B = 0$ mT, and $R_p(E)_B$ is the resistance when $E \neq 0$ and $B \neq 0$. Thus, by using the variation of resistances form Figs. 17 and 18, it is possible to obtain the variation of the electro-magnetoconductive effects, as depicted in Fig. 21. The dependence of the electrical conductivity on the electric field superimposed on the magnetic is also clearly observed. Due to the interactions between column dipoles, the effect of dipole columns agglomeration is much more pronounced for MRS_1 as compared to MRS_2, for high values of B.

Conclusions

In this work, two suspensions with considerable magnetorheological properties are manufactured. Silicone oil was utilised as a liquid carrier

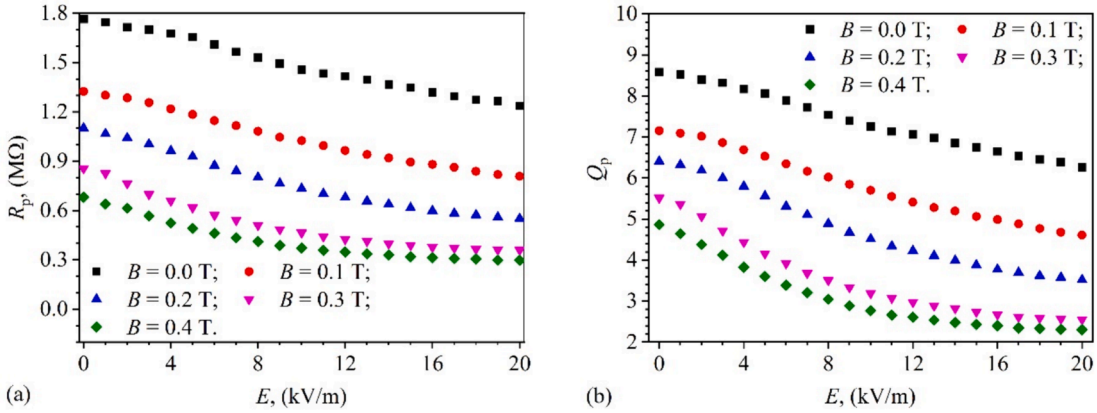

Fig. 17. Variation of the electrical resistance R_p (a) and of the quality factor Q_p (b) with the intensity E of a static electric field for ED_1, at fixed values of magnetic flux density B.

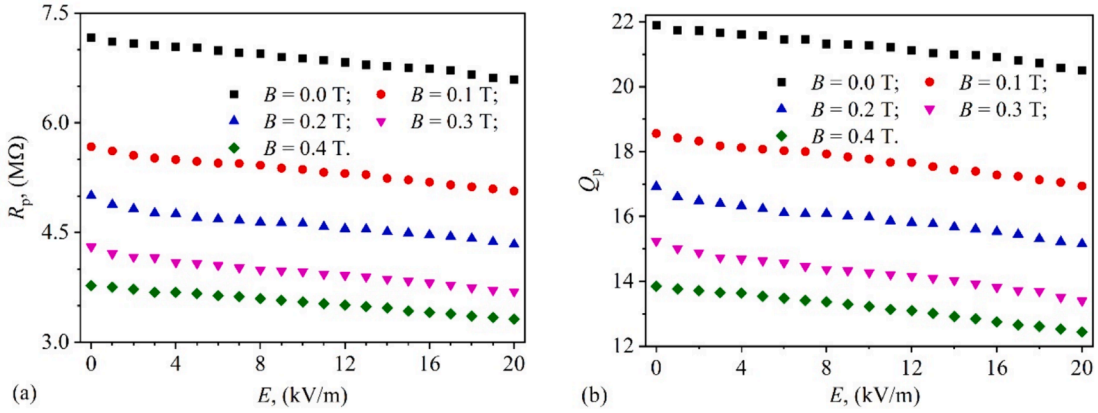

Fig. 18. Variation of the electrical resistance R_p (a) and of the quality factor Q_p (b) with the intensity E of a static electric field for ED_2, at fixed values of magnetic flux density B.

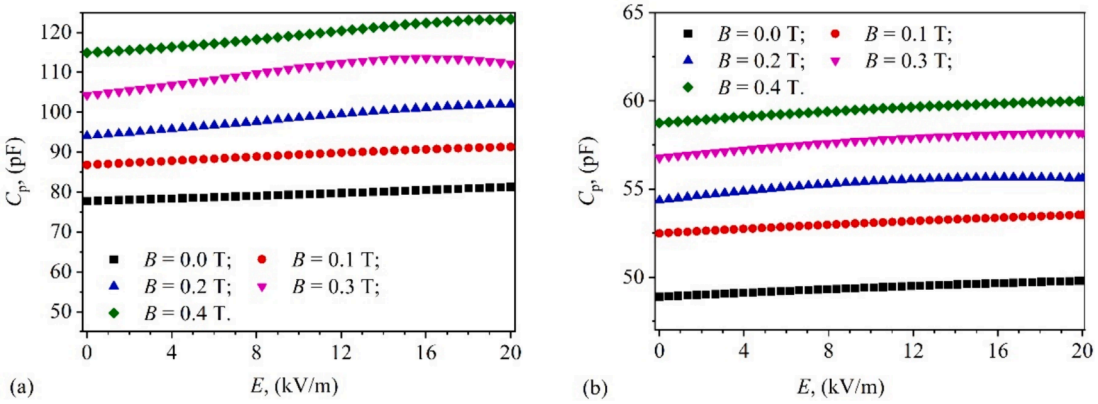

Fig. 19. Variation of the electrical capacitance C_p with the intensity E of a static electric field and at fixed values of magnetic flux density B, for ED_1 (a) and ED_2 (b).

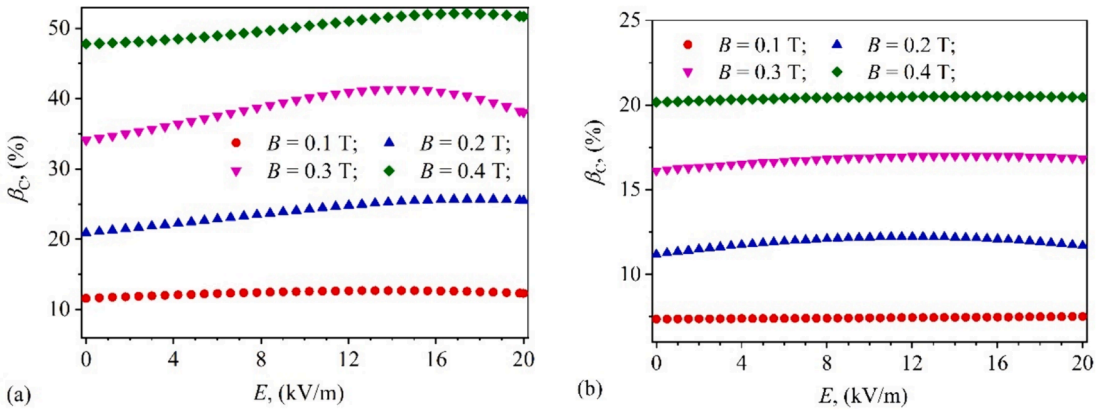

Fig. 20. Variation of the electro-magnetodielectric effect β_C with the intensity E of a static electric field and at fixed values of magnetic flux density B, for MRS_1 (a) and MRS_2 (b).

and two types of fillers (P_1 and P_2) as dispersed phase were compared. The fillers consist of polypyrrole nanotubes decorated with magnetite nanoparticles (PPYM6 and PPYM2.5). Each magnetorheological suspension contains the same volume fraction of PPYM6 and PPYM2.5 nanoparticles, and the same volume of silicone oil. Furthermore, the suspensions are used as dielectric materials for fabrication of electrical devices. An experimental setup is built to measure the electrical resistance and the quality factor at the terminals of the devices in the presence of static electric and magnetic fields superimposed on a medium-frequency electric field.

Based on the experimental results, the electrical capacitance of the capacitor is obtained. It is shown that the behaviour of both resistance and capacitance can be well described qualitatively by the models of electrical and magnetic dipolar approximations, and respectively by using the principle of effects superposition. An important feature is that in spite of the equal amounts of matrix and fillers, the induced electro-magnetodielectric effect (e.g. at $B = 0.4$ T and $0 \leq E(\mathrm{kV\,m^{-1}}) \leq 20$; Fig. 20), and the electro-magnetoconductive effect (e.g. at $B = 0.4$ T and $12 \leq E(\mathrm{kV\,m^{-1}}) \leq 20$; Fig. 21) is higher up to about three times for

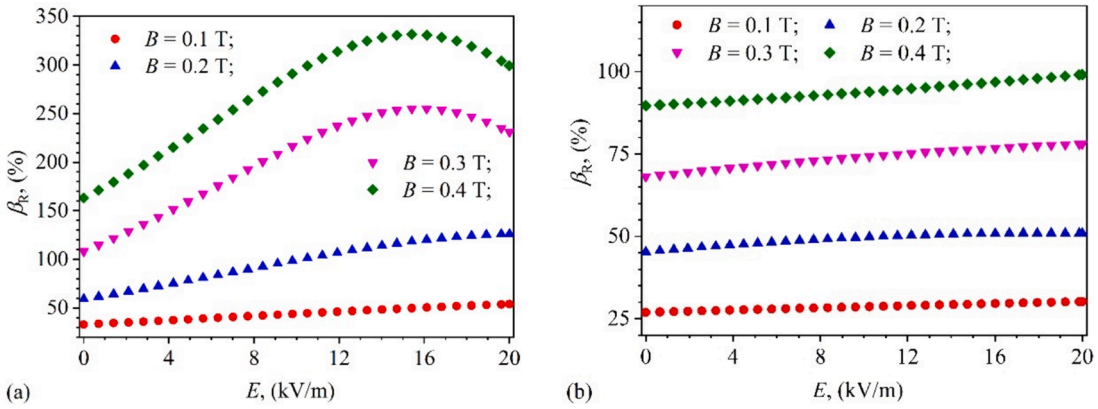

Fig. 21. Variation of the electro-magnetoconductive effect β_R with the intensity E of a static electric field and at fixed values of magnetic flux density B, for MRS_1 (a) and MRS_2 (b).

suspensions with P_1 particles.

These properties are important for the device manufacturing for monitoring electric and magnetic fields and respectively electromagnetic fields, as it is well-known that they contribute to pollution affecting life.

CRediT authorship contribution statement

Eugen Mircea Anitas: Investigation, Visualization, Writing – original draft. **Andrei Munteanu:** Investigation, Writing – original draft. **Michal Sedlacik:** Conceptualization, Funding acquisition, Supervision, Writing – review & editing. **Ioan Bica:** Conceptualization, Formal analysis, Investigation, Methodology. **Lenka Munteanu:** Investigation, Visualization, Writing – review & editing. **Jaroslav Stejskal:** Conceptualization, Methodology.

Declaration of competing interest

The authors declare the following financial interests/personal relationships which may be considered as potential competing interests: Michal Sedlacik reports financial support was provided by Czech Science Foundation. If there are other authors, they declare that they have no known competing financial interests or personal relationships that could have appeared to influence the work reported in this paper.

Data availability

Data will be made available on request.

Acknowledgements

The authors A.M., L.M., and M.S. wish to thank the Czech Science Foundation [23-07244S] for the financial support. This work and the project were realized with the financial support of the internal grant of the TBU in Zlín No. IGA/CPS/2024/008 funded from the resources of specific university research.

References

[1] S. Genc, Experimental studies on magnetorheological fluids, (2022).
[2] Bica I, Liu YD, Choi HJ. Physical characteristics of magnetorheological suspensions and their applications. J Ind Eng Chem 2013;19(2):394–406.
[3] Nika G, Vernescu B. Multiscale modeling of magnetorheological suspensions. Z Angew Math Phys 2020;71:1–19.
[4] Osial M, Pregowska A, Warczak M, Giersig M. Magnetorheological fluids: A concise review of composition, physicochemical properties, and models. J Intell Mater Syst Struct 2023;21.
[5] de Vicente J, Klingenberg DJ, Hidalgo-Alvarez R. Magnetorheological fluids: a review. Soft Matter 2011;7(8):3701–10.
[6] Jeong JY, Kim S, Baek E, You CY, Choi HJ. Suspension rheology of polyaniline coated manganese ferrite particles under electric/magnetic fields. Colloid Surf A-Physicochem Eng Asp 2023;656:130438.
[7] Pei P, Peng Y. The squeeze strengthening effect on the rheological and microstructured behaviors of magnetorheological fluids: A molecular dynamics study. Soft Matter 2021;17(1):184–200.
[8] Plachy T, Cvek M, Munster L, Hanulikova B, Suly P, Vesel A, et al. Enhanced magnetorheological effect of suspensions based on carbonyl iron particles coated with poly (amidoamine) dendrons. Rheol Acta 2021;60:263–76.
[9] Lu Q, Balasoiu M, Choi HJ, Anitas EM, Bica I, Cirigiu LME. Magneto-dielectric and viscoelastic characteristics of iron oxide microfiber-based magnetoreological suspension. J Ind Eng Chem 2022;112:58–66.
[10] Bica I, Anitas E. Magnetic flux density effect on electrical properties and viscoelastic state of magnetoactive tissues. Compos B Eng 2019;159:13–9.
[11] Bica I, Anitas E. Magnetodielectric effects in hybrid magnetorheological suspensions based on beekeeping products. J Ind Eng Chem 2019;77:385–92.
[12] Acharya S, Tak RSS, Singh SB, Kumar H, Characterization of magnetorheological brake utilizing synthesized and commercial fluids, Mater Today: Proc 2021:46; 9419-24.
[13] Bica I. Damper with magnetorheological suspension. J Magn Magn Mater 2002;241 (2–3):196–200.
[14] Deng Z, Wei X, Li X, Zhao S, Zhu S. Design and multi-objective optimization of magnetorheological damper considering vehicle riding comfort and operation stability. J Intell Mater Syst Struct 2022;33(9):1215–28.
[15] Yang J, Ning D, Sun S, Zheng J, Lu H, Nakano M, et al. A semi-active suspension using a magnetorheological damper with nonlinear negative-stiffness component. Mech Syst Sig Process 2021;147:107071.
[16] Tang X, Du H, Sun S, Ning D, Xing Z, Li W. Takagi-Sugeno fuzzy control for semi-active vehicle suspension with a magnetorheological damper and experimental validation. IEEE/ASME Trans Mechatron 2016;22(1):291–300.
[17] Shiao Y, Kantipudi MB. High torque density magnetorheological brake with multipole dual disc construction. Smart Mater Struct 2022;31(4):045022.
[18] Bica I. Magnetorheological suspension electromagnetic brake. J Magn Magn Mater 2004;270(3):321–6.
[19] Choi SB. Sedimentation stability of magnetorheological fluids: the state of the art and challenging issues. Micromachines 2022;13(11):1904.
[20] Bombard AJF, Goncalves FR, Morillas JR, de Vicente J. Magnetorheology of dimorphic magnetorheological fluids based on nanofibers. Smart Mater Struct 2014;23(12):125013.
[21] Ko SW, Yang MS, Choi HJ. Adsorption of polymer coated magnetite composite particles onto carbon nanotubes and their magnetorheology. Mater Lett 2009;63 (11):861–3.
[22] Stejskal J, Trchova M. Conducting polypyrrole nanotubes: a review. Chem Pap 2018;72(7):1563–95.
[23] Bica I, Iacobescu G-E. The influence of magnetic fields on the electrical conductivity of membranes based on cotton fabric, honey, and microparticles of carbonyl iron and silver. Materials 2023;16(5):1995.
[24] Stejskal J, Sapurina I, Vilcakova J, Plachy T, Sedlacik M, Bubulinca C, et al. Conducting and magnetic composites polypyrrole nanotubes/magnetite nanoparticles: Application in magnetorheology. ACS Appl Nano Mater 2021;4(2): 2247–56.
[25] Gwon H, Park S, Lu Q, Choi HJ, Lee S. Size effect of iron oxide nanorods with controlled aspect ratio on magneto-responsive behavior. J Ind Eng Chem 2023;124: 279–86.
[26] Bica I, Bălăşoiu M, Sfirloaga P. Effects of electric and magnetic fields on dielectric and elastic properties of membranes composed of cotton fabric and carbonyl iron microparticles. Results Phys 2022;35:105332.
[27] Melle S, Study of the dynamics in MR suspensions subject to external fields by means of optical techniques: aggregation processes, structure formation and temporal evolution, Madrid, 1995.

Paper 2

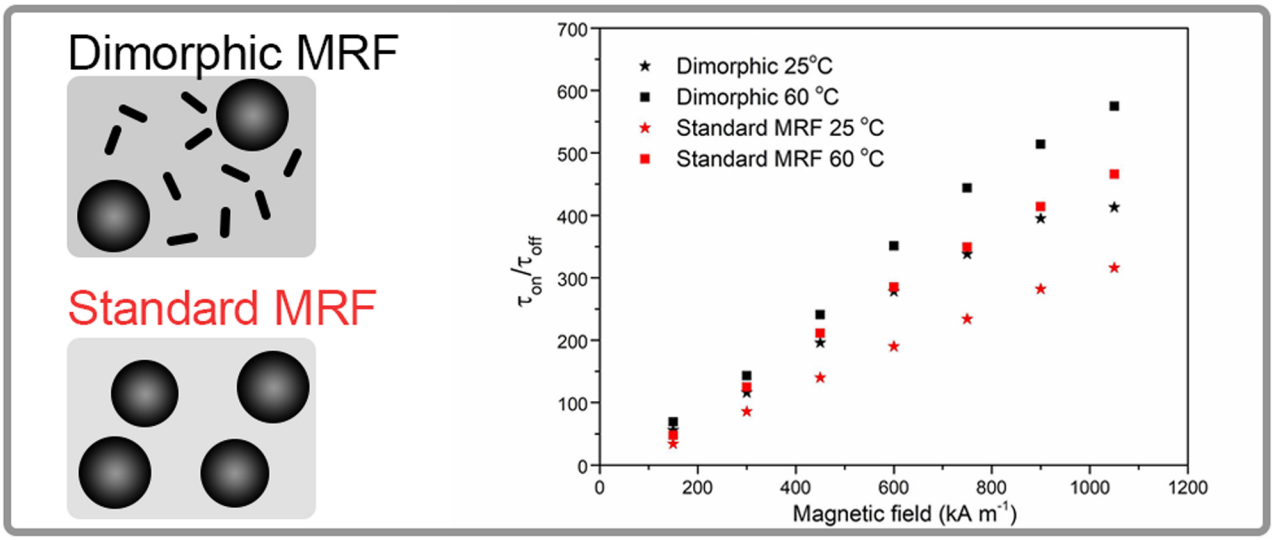

Springer
Rheologica Acta
Accepted 15th July 2023

Rheologica Acta (2023) 62:461–472
https://doi.org/10.1007/s00397-023-01409-9

ORIGINAL CONTRIBUTION

Bidisperse magnetorheological fluids utilizing composite polypyrrole nanotubes/magnetite nanoparticles and carbonyl iron microspheres

Andrei Munteanu[1] · Tomáš Plachý[1] · Lenka Munteanu[1] · Fahanwi Asabuwa Ngwabebhoh[1] · Jaroslav Stejskal[1] · Miroslava Trchová[2] · Michal Kubík[3] · Michal Sedlačík[1,4]

Received: 16 May 2023 / Revised: 14 July 2023 / Accepted: 15 July 2023 / Published online: 2 August 2023

Abstract

Conductive polypyrrole nanotubes were synthesized with a two-step one-pot synthesis. During synthesis, the nanotubes were decorated with magnetite nanoparticles at different concentrations granting them magnetic properties. The characterization of the tubes revealed differences from the theoretical reactions. A bidisperse magnetorheological fluid (MRF) was prepared by mixing the composite polypyrrole nanotubes/magnetite nanoparticles with commercial carbonyl iron spherical microparticles in silicone oil. The rheological properties of the bidisperse system were studied under the presence of magnetic field at room and elevated temperature. An enhancement of the MR effect with the presence of the nanotubes was observed when compared with a standard MRF consisted only of magnetic microparticles. Due to the faster magnetic saturation of the nanotubes, this enhancement is exceptionally high at low magnetic fields. The stability of the system is studied under dynamic conditions where it is revealed that the nanotubes keep the standard particles well dispersed with the sedimentation improving by more than 50%.

Keywords Magnetic composite · Polypyrrole nanotubes · Magnetorheology · Bidisperse system · Sedimentation Stability

Introduction

A magnetorheological fluid (MRF) is a unique type of smart material which may alter its viscosity by several orders of magnitude within milliseconds upon exposure to an external magnetic field (de Vicente et al. 2011). A typical MRF is composed of micrometre-sized magnetic particles suspended in a non-magnetic carrier liquid. Due to its ability to change from liquid to solid-like state, several applications are involved. Brakes, clutches, and shock absorbers are the most common examples (Bai et al. 2019; Zainordin et al. 2021; Park et al. 2021; Deng et al. 2021).

Despite the plethora of studies and applications, these MRFs still face prominent problems such as corrosion at high temperatures and aggressive environments, coagulation due to the unfavourable interactions between the particles and liquid carrier, and lastly sedimentation caused by the density mismatch of the components. Several solutions have been proposed to overcome these problems, most notably using various additives, different morphologies, and coating the magnetic particles (Stejskal et al. 2021a; Thiagarajan and Koh 2021). Another approach would be the addition of rod-like particles in the suspension (Sedlacik and Pavlinek 2017), thus creating a bidisperse system (or also called dimorphic, a system in which the dispersed phase particles are of two different morphologies or size). Such dimorphic magnetorheological fluids (DMRFs) decrease the sedimentation effect to acceptable levels and prevent the coagulation due to the steric repulsions provided by the rod-like particles (Sedlacik et al. 2013). The majority of bidisperse studies however are focused on the interactions between spheres with heavily mismatched size. These studies have shown that sedimentation stability is significantly increased (Wang et al.

✉ Michal Sedlačík
msedlacik@utb.cz

1 Centre of Polymer Systems, University Institute, Tomas Bata University in Zlín, 760 01 Zlín, Czech Republic

2 University of Chemistry and Technology Prague, 6, 166 28 Prague, Czech Republic

3 Faculty of Mechanical Engineering, Institute of Machine and Industrial Design, Brno University of Technology, 616 69 Brno, Czech Republic

4 Department of Production Engineering, Faculty of Technology, Tomas Bata University in Zlín, 760 01 Zlín, Czech Republic

2021b). Nonetheless, inconsistencies are observed in regard to the volume fraction of smaller particles. At lower fractions, the small particles fill the gaps in the chain-like structures formed by the bigger ones when an external magnetic field is applied; however; higher concentrations could cause an inferior performance (Wereley et al. 2006; Chand et al. 2014). Other types of bidisperse systems include the addition of rod-like particle into a conventional MRF composed of micron spheres. Current studies include different types of rods, mainly divided to magnetic and non-magnetic ones. Apart from improving the viability of such MRFs, these rod-like particles may also improve the mechanical properties, such as higher yield stress when an external magnetic field is applied (on-state). Jiang et al. (2011) successfully synthesized a DMRF using magnetic Fe nanowires, showing both a major reduction in sedimentation and better rheological properties which were observed even at low magnetic fields. Unfortunately, these nanowires are prone to oxidation and have relatively high values of coercivity and remanent magnetization. This could lead to a short life span of the system. Ngatu et al. (2008) also used similar nanowires with a higher length resulting in improved stability, but the rheological properties remained roughly the same. Eventually, oxidation was resolved using coated particles; however, the magnetic properties of these samples were severely hindered (Sedlacik et al. 2013). Non-magnetic rods also may show improvements in mechanical properties, leading to the conclusion that these improvements are caused mainly by the shape of the particles. This was further validated by Bombard et al. (2014), who investigated the stoichiometric ratio of the two components, illustrating that these systems are more efficient at low rod concentrations.

With the basic concepts already investigated, the way is paved for more complex DMRFs. A novel DMRF using polypyrrole (PPy) nanotubes decorated with magnetite, Fe_2O_3, which may alter their magnetic properties based on their preparation, is presented. It is important to note that this is one of the first reports of a DMRF composed of magnetic spheres and nanotubes. In a preliminary work, the effect of the tube morphology and the magnetic and conducting properties of these nanotubes was studied (Stejskal et al. 2021b). Polypyrrole nanotubes were chosen for several reasons. First, the synthesis of such tubes is proven to be quick and facile. As mentioned above, some MRFs are prone to oxidation; however, PPy nanotubes have shown antioxidant activity (Upadhyay and Kumar 2013). Moreover, non-magnetic PPy nanotubes are very versatile being able to find a utilization in several applications including actuation, batteries, conductive inks, electromagnetic interference shielding, sensors, and electrorheological fluids (Stejskal and Trchová 2018). In addition, non-magnetic PPy nanotubes have been used in medical applications including adsorbing influenza viruses, antimicrobial activity, necrolysis, and tissue engineering (Liao et al. 2014; Ivanova et al. 2017). Magnetic nanorods have been already used in biomedical applications (Nikolaou et al. 2021), thus further increasing the interest of magnetic PPy nanotubes. For the majority of literature, the rod/tube-like particles are notable smaller than the spherical one. Wang et al. (2021a) studied a DMRF with both tubes and spherical particles being in the range of ~10 nm with great results. Lastly, several DMRFs were prepared using creative materials and morphologies with the majority focusing on the sedimentation stability; however, their MR performance was inferior (Wang et al. 2018; Cvek et al. 2018; Marins et al. 2019).

In this work, composite magnetic PPy nanotubes were synthesized using a novel method, and subsequently, their magnetic properties were studied together with other physical properties. Following, several bidisperse systems were prepared, and their (magneto)rheological properties were studied and compared with a standard MRF. Lastly, the thermal stability of the DMRF is evaluated together with the sedimentation stability in a dynamic environment as a closer comparison to the actual applications.

Materials and methods

Synthesis of the magnetic nanotubes

Polypyrrole nanotubes were synthesised and decorated with magnetite nanoparticles during a two-step synthesis. Two samples were synthesised at different molarities of iron(III) chloride hexahydrate ($FeCl_3{\cdot}6H_2O$) (>99%) which was provided by Sigma-Aldrich together with the rest of the chemicals that are mentioned in this part. Table 1 presents the amount of each component used with the mole ratio of $FeCl_3{\cdot}6H_2O$ over pyrrole represented as n. For the synthesis, firstly, the pyrrole (>97%) was dispersed in water (0.2 M in 100 mL), with methyl orange (0.004 M in 100 mL) being added later on. The dye is the key substance which guides the growth of tube-like morphology instead of spheres (Mori et al. 2017). Aside, the second solution of $FeCl_3{\cdot}6H_2O$ in water ($FeCl_3{\cdot}6H_2O$ is 0.5 M in 100 mL for n=2.5 and 1.2 M in 100 mL for n=6) was prepared. Right after, both solutions were combined, and the polymerization of pyrrole to the PPy nanotubes was completed at room temperature once

Table 1 Preparation compositions for PPy/magnetite nanotubes

	N	Pyrrole (mL)	$FeCl_3{\cdot}6H_2O$ (g)	Water (mL)	Methyl orange (mg)
Sample 1	2.5	1.4	13.52	200	130
Sample 2	6	1.4	32.45	200	130

the mixture turned dark brown/black and thickened with the procedure taking a few minutes.

Figure 1 shows the main synthesis reactions. The final molar concentrations of the reaction mixture are 0.1-M pyrrole and 0.25-M $FeCl_3 \cdot 6H_2O$ for n=2.5 and 0.6 M for n=6 and 0.002-M methyl orange. To decorate the PPy nanotubes with magnetite, the resulting PPy dispersion was mixed with an excessive amount of ammonium hydroxide (4 M) at room temperature until the solution became basic (pH > 10). The pH was periodically confirmed using a pH meter. Lastly, the decorated nanotubes were isolated by filtration and washed with ethanol. The particles were left to dry overnight at 60 °C.

The final yields were 5.4 g for n=2.5 and 10.6 g for n=6. The abovementioned reactions are described in detail in a previous work, focusing only on the synthesis of the rods and perfecting the molar ratios, during which it was possible to tune the conductivity and the magnetic properties of the nanotubes by changing the molar ratio n (Stejskal et al. 2021b). However, to obtain magnetic nanoparticles with higher magnetization saturation, the deprotonation with ammonium hydroxide was modified using ammonium hydroxide with a much higher concentration in this work. For n=2.5, all $FeCl_3 \cdot 6H_2O$ should be consumed by the reaction (Fig. 1) to produce the PPy nanotubes in the base form. For n=6, the excess amount converts the mixture of $FeCl_3$ and $FeCl_2$ to magnetite and decorate the nanotubes.

Characterization of particles

The ATR FTIR spectra of the powdered samples were obtained using the Nicolet 6700 spectrometer (Thermo-Nicolet, USA) equipped with a reflective ATR extension GladiATR (PIKE Technologies, USA) and a diamond crystal. The spectra were recorded in the 4000–400-cm^{-1} range with a DLaTGS (deuterated L-alanine doped triglycine sulphate) detector at resolution of 4 cm^{-1}, 64 scans, and a Happ-Genzel apodization. The morphology of PPy particles decorated with magnetite was studied by scanning electron microscope NOVA NanoSEM 450 (FEI, the Netherlands), while their magnetic saturation was investigated using a vibrating sample magnetometer (VSM, Model 7407, USA) with the intensity of magnetic field in a range from −10 to +10 kOe.

The specific surface area of the samples was estimated using nitrogen adsorption/desorption measurement using a surface area analyser (BELSORP-mini II, BEL Japan, Inc., Japan). The data was treated with a Brunauer, Emmett, and Teller (BET) multipoint method. Thermogravimetric analysis (TGA; TGA Q500, TA Instruments, New Castle, USA) was performed in air in temperature range 25–700 °C using a heating rate 10 °C min^{-1}.

Preparation of the dimorphic magnetorheological fluids

For the dimorphic system, carbonyl iron (CI) spherical particles (CN grade, iron content >99.5%, d_{50}=6.5–8.0 µm; BASF, Germany) were mixed with the magnetic composite PPy nanotubes/magnetite nanoparticles in silicone oil (Lukosiol M200, Chemical Works Kolín, Czech Republic; viscosity 194 mPa s, density 0.965 g cm^{-3}) at various concentrations. Before preparation, the particles (both PPy nanotubes and iron microspheres) were dried overnight at high vacuum at 80 °C along with the oil to remove possible moisture. Several DMRFs were prepared with the code-names and compositions shown in Table 2.

The newly prepared DMRFs were always measured with the following techniques immediately after their preparation. Meanwhile, a sonication process was applied using an ultrasonic bath to ensure that no aggregates were formed.

Characterization of the dimorphic magnetorheological fluids

The rotational rheometer Physica MCR 502 (Anton Paar, Graz, Austria) was employed to investigate the flow

Table 2 Composition of the prepared magnetorheological fluids in vol%

Components	Code name		
	MRF 2.5	MRF 6	Standard MRF
Carbonyl iron	10	10	10
PPy/Fe_3O_4 nanotubes (n=2.5)	1	0	0
PPy/Fe_3O_4 nanotubes (n=6)	0	1	0
Silicone oil	89	89	90

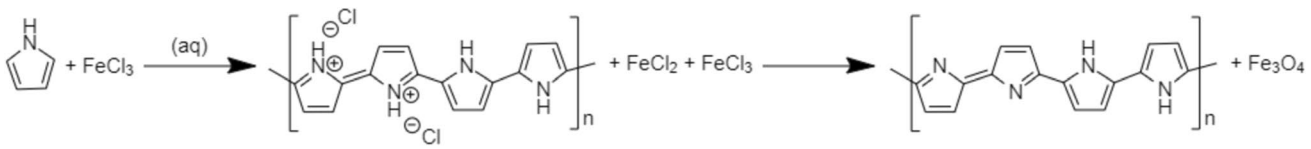

Fig. 1 The two-step synthesis of magnetic nanotubes; PPy nanotubes are first created using the oxidation of the pyrrole with $FeCl_3 \cdot 6H_2O$. Excess amounts of $FeCl_3 \cdot 6H_2O$ led to the creation of magnetite under alkaline conditions converting PPy to a base form

properties of the MRFs. To determine the effect of the magnetic field, a magneto-cell (Physica MRD 180/1T) was employed. The samples were exposed to various external magnetic fields up to 1050 kA m^{-1}. A temperature control was achieved using an additional external bath. All samples were measured using a parallel-plate geometry of 20 mm with rough surface. The gap was set at 1 mm for all measurements since this parameter is proved to affect the rheological properties (Jonkkari et al. 2012). Before each test, the samples were stirred at shear rate $(\dot{\gamma})$ of 50 s^{-1} for a minute to redisperse them. The measurements were performed in the shear rate range of 0.01 to 200 s^{-1} to ensure no overflow happens during the measurements. Flow curves were performed in the abovementioned range steadily increasing the magnetic field starting with 150 kA m^{-1} and increasing it by intervals of 300 kA m^{-1}. After the final flow curve at 1050 kA m^{-1}, the sample was redispersed and a second flow curve was performed with the magnetic field off to evaluate the impact of previews on-state measurements. Step-wise increases of magnetic field were performed under steady shear of 50 s^{-1} during which the magnetic field was turned on and off every 20 s, each time increasing by 150 kA m^{-1}. The same tests were repeated at 60 °C. The dynamic sedimentation tests were performed in the following way. The samples were pre-sheared at 50 s^{-1} for a minute to redisperse the particles. Then, the shear rate was removed with a low magnetic field of 300 A m^{-1} applied. The field was then removed and shear of 10 s^{-1} was reapplied. The sedimentation was calculated as the ratio of the current shear stress over the shear stress captured right after the field was removed thus at the start of the off-state.

Results and discussion

Characterization of the polypyrrole/magnetite particles

FTIR spectroscopy

To confirm the successful synthesis of the targeted tubes, their ATR FTIR spectra are compared with the spectra of related and well-established particles, as presented in Fig. 2. The infrared spectrum of the "standard" PPy nanotubes (PPyNT) exhibits the main bands with maxima at 1514 cm^{-1} (C–C-stretching vibrations in the pyrrole ring), at 1435 cm^{-1} (C–N-stretching vibrations in the ring), at 1283 cm^{-1} (C–H or C–N in-plane deformation modes), at 1128 and 1088 cm^{-1} (breathing vibrations of the pyrrole rings), and at 998 cm^{-1} (C–H and N–H in-plane deformation vibrations). In addition, the peaks located at 955 and 832 cm^{-1} correspond to the C–H out-of-plane deformation

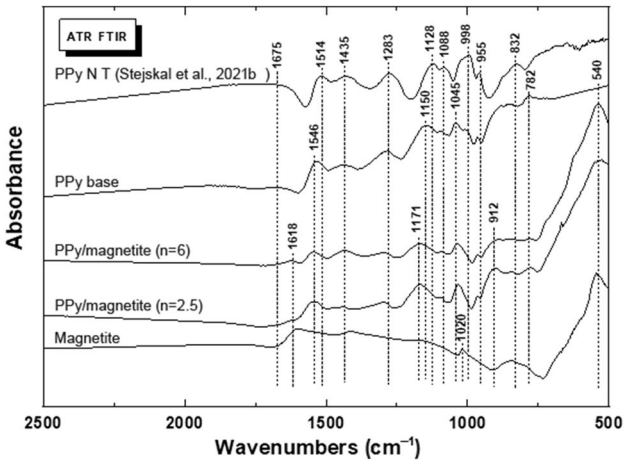

Fig. 2 The ATR FTIR spectra of the magnetic composite PPy nanotubes/magnetite nanoparticles compared with the spectra of "standard" PPy nanotubes, PPy base, and magnetite (Stejskal et al. 2016, 2021b, a; Stejskal and Trchová 2018)

vibrations of the ring (Stejskal and Trchová 2018; Stejskal et al. 2021a). The infrared spectra of the PPy nanotubes are recorded in Fig. 2. The PPy/magnetite n=6 and 2.5 exhibit a peak at 1618 cm^{-1}, a maximum at 1546 cm^{-1}, and further notable peaks at 1435, 1283, and 1171 cm^{-1}, and also at 1088, 1045, and 912 cm^{-1}. The shifts of the main bands can be observed when compared to the spectrum of the "standard" PPy base, this corresponds to a slight deprotonation of the samples which was discussed in detail in a previous work (Stejskal et al. 2016, 2021b). The deprotonation is also reflected in the intensity decrease of the broad band observed above 1800 cm^{-1}. The presence of magnetite is detected in the spectra by the peaks observed in its spectrum and by the enhancement of the intensity of the broad absorption band below 900 cm^{-1}.

Morphology

The particles' morphology of both composites based on differing molarities was studied by SEM, as presented in Fig. 3.

As can be seen, the nanotubular morphology of PPy was confirmed with a nano-scaled diameter and a length in micrometre range. Furthermore, the PPy/magnetite (n=6) particles (Fig. 3b) exhibit obvious magnetite coating (the presence of magnetite was also confirmed via FTIR and VSM). However, the n=2.5 counterpart also shows the magnetite presence (Fig. 3a), albeit in a lower amount. This hints that a residual amount of $FeCl_3 \cdot 6H_2O$ was indeed present after the reaction, even though for n=2.5, theoretically, all $FeCl_3$ oxidant should have been consumed and no magnetite thus produced, as mentioned in the synthesis section.

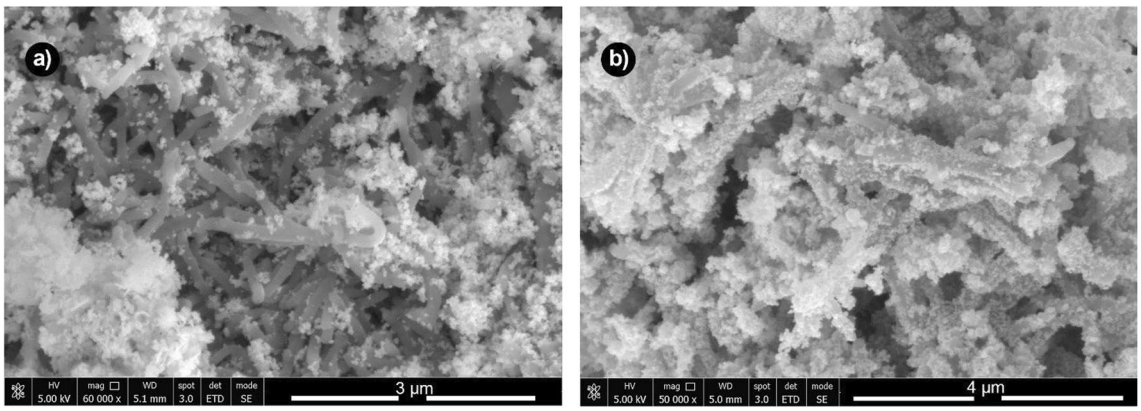

Fig. 3 Scanning electron microscopy of PPy/magnetite particles based on different molarities of $FeCl_3 \cdot 6H_2O$: n=2.5 (**a**) and n=6 (**b**)

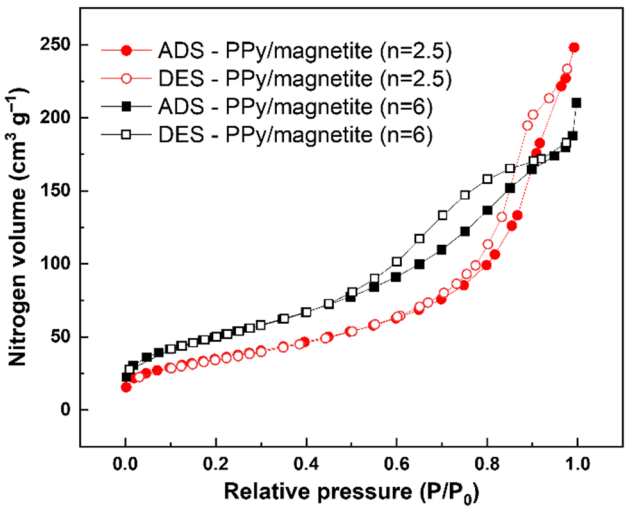

Fig. 4 Nitrogen adsorption and desorption isotherms of the prepared composite particles: PPy/magnetite (n=2.5) and PPy/magnetite (n=6)

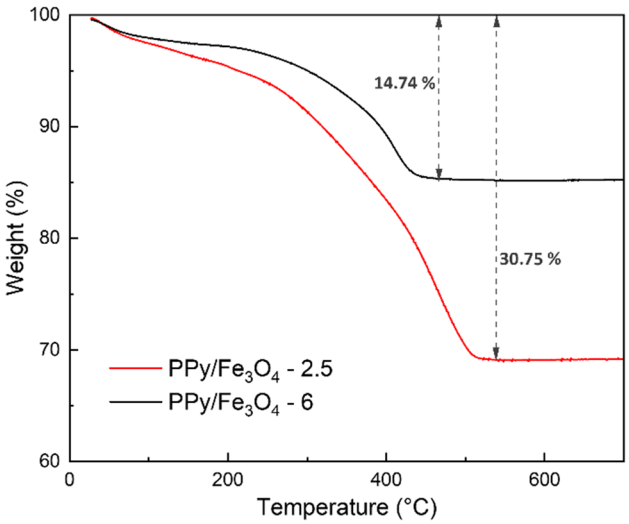

Fig. 5 Thermogravimetric analysis of prepared composite particles PPy/Fe_3O_4. Experiments were performed in an air atmosphere using heating rate 10 °C min^{-1}

Surface properties

The different mole ratio of the precursors used during the synthesis also affected the surface area of the prepared composite particles (Fig. 4). While PPy/magnetite (n=2.5) particles exhibited specific surface area 126 m^2 g^{-1}, the sample PPy/magnetite (n=6) possessed higher surface area 183 m^2 g^{-1} due to the presence of nanosized magnetite particles. Furthermore, the shape of adsorption and desorption curves indicated solid surface of the particles with the presence of micropores.

Thermogravimetric analysis

Thermogravimetric analysis of the composite PPy/magnetite particles in air (Fig. 5) showed that the sample PPy/magnetite (n=6) exhibited significantly lower drop in weight (~15%) than the second sample (~30%). While iron oxide particles during TGA treatment commonly exhibit only insignificant drop in weight (Jafari-Soghieh et al. 2019), PPy in air can be fully decomposed (Plachy et al. 2013). The mass loss should be then ascribed to PPy decomposition and is more prominent for the sample prepared at n=2.5. The residues represent the magnetite particles, and as can be clearly seen, their higher content can be found in the sample PPy/magnetite (n=6) as expected.

Magnetic properties

The composite PPy/magnetite particles exhibited magnetic properties, as illustrated in Fig. 6. The composites prepared at n=2.5 and n=6 were analysed. The synthesised particles

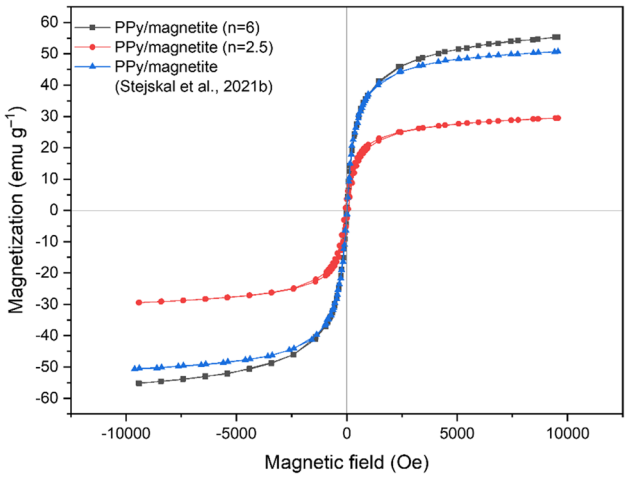

Fig. 6 Magnetic properties PPy/magnetite nanotubes composite prepared at different molarities and compared with their previous alternative as reported in Stejskal et al. (2021b)

were further compared with their analogue from a previously published report (Stejskal et al. 2021b) for a reference.

As can be seen, the newly synthesised PPy/magnetite peaked at 55.2 emu g^{-1} exceeding the maximum peak of its previous alternative, peaking at 51 emu g^{-1}; thus, this modified synthesis proved to be better. As for the reference comparison, synthesised pure magnetite nanoparticles were reported in the literature with saturation magnetization 65 emu g^{-1} and 62 emu g^{-1} (Qiu et al. 2006; Fekry et al. 2022).

Magnetorheology

The rheological properties of the bidisperse system composed of the magnetic composite PPy nanotubes/magnetite nanoparticles and standard CI microspheres were investigated. The flow curves at various magnetic fields for the MRF 6 are shown in Fig. 7.

The impact of the magnetic field is apparent on the flow curves with the shear stress increasing several orders of magnitude especially at the lower shear rates. With the presence of the magnetic field, the particles are arranged into chain-like structures which significantly increase the shear stress. As the magnetic field is further increased, the rate of stress increase is lower as the magnetization of the particles reaches their saturation values, a typical behaviour of a magnetorheological fluid. For the majority of the experimental window, the shear stress values show a plateau. Apart from the plateau values, the magnetic field also affects its length. To be specific, as can be seen in Fig. 7b, 150 kA m^{-1} is apparent that the hydrodynamic forces are starting to take over the magnetic ones at ~1 s^{-1} with the termination of the plateau and the increase of stress. The critical shear rate can be observed closer to 20 s^{-1}. At saturated fields, i.e. 1050 kA m^{-1}, the data indicates that the chain-like structures become more robust and harder for the hydrodynamic forces to break. Consequently, the magnetic forces dominate over the hydrodynamic ones throughout the majority of the experimental window of the applied shear rate starting from the very low shear rates with such long plateaus being observed before for bidispersed MRFs (Cvek et al. 2022). The dimorphic sample in particular has their plateau length increased when compared with the standard MRF which can be found in supplementary information. Such plateaus can be associated with flow instabilities such as the shear banding phenomenon. Indeed, throughout the entire experimental window and for all measurements where a magnetic field was used, there is shear banding as a result of the chain-like structures that the magnetic particles form essentially phase separating from the liquid carrier. Other shear banding phenomena in colloids and specifically for rod-like particles should not be present as the magnetic interactions between

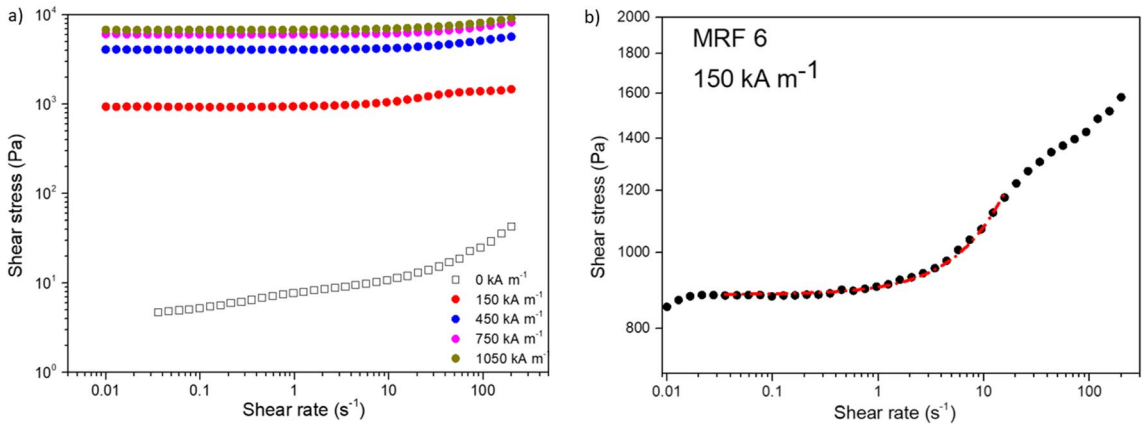

Fig. 7 Flow curves for sample MRF 6 **a** for different magnetic fields and **b** for 150 kA m^{-1}. The red line represents a fit based on the Bingham plastic model

the particles are too strong (Ovarlez et al. 2009; Parisi et al. 2022). This is the case even at high shear rates where the hydrodynamic forces dominate (Martínez-Cano et al. 2023).

The critical shear rate, where the hydrodynamic forces overcome the magnetic ones, is represented by an inclination of the flow curve to the Newtonian behaviour (Stejskal and Trchová 2018). For applications, it is important to keep the magnetic forces dominating for as high shear rates as possible (Wang and Gordaninejad 2006); thus, the present suspension can be characterized as excellent. The rest of the samples share a similar behaviour as shown in the supporting information.

From Fig. 7b, a simple Bingham plastic model was used to extract the yield stress which is shown in Table 3 together with the rest of the samples.

The dimorphic samples show more than two times higher yield stress and lower magnetic fields with the difference being reduced towards the saturated fields. The MRF 6 shows a slightly higher yield stresses although the difference with MRF 2.5 is minor. The increase of the yield stress is explained through the nanotubes which fill the gaps in the chain-like structures formed by the spheres, thus assembling a more robust arrangement (Ashtiani et al. 2015).

Previously, it was mentioned that the magnetic forces dominate over the hydrodynamic ones at lower shear rates. As the shear rate increases, eventually the hydrodynamic forces become relevant. A relevantly good quantity to compare the two types of forces is the Mason number (Mn) which is defined as the ratio between the hydrodynamic forces over the magnetic ones. The well-established behaviour in the study of Klingenberg et al. (2007) was used to calculate the Mn which essentially scales linearly with shear rate and inverse square to the magnetic field $Mn \sim \dot{\gamma} H^{-2}$. The viscosity then was plotted against Mn as can be seen in Fig. 8. For all samples, the Mn is way below unity indicating that the magnetic forces dominate for the entire experimental window. The standard MRF is following the predicted behaviour with the data from different magnetic fields collapsing together. For the dimorphic samples (n=6) however, that is not the case. The curves are not collapsing and tend to move towards lower Mn as the magnetic field is increased indicating stronger magnetic interactions. It is important to note that the Mn calculation includes many assumptions, such as perfect spheres of the same size and simplified magnetic interactions between both types of particles and the particles with the carrier. Regardless, the curves are relevantly close to each other. The same behaviour is observed for MRF 2.5 which can be found in supplementary information (Figure S3). Such discrepancies have been observed before. Literature suggests that at saturated fields, the non-linear magnetization has a significant effect (Klingenberg et al. 2007); however, in our case, the standard MRF is not impacted. Such a discrepancy was also observed in a bidisperse MRF, yet the standard equivalent follows the expected dependency (Cvek et al. 2022). The explanation suggested that the interparticle friction which was not accounted in the theory plays a notable role. Note that we used the same equations to extract the Mn examples mentioned above. Another potential explanation with the Mn not scaling as $Mn \sim \dot{\gamma} H^{-2}$ for DMRFs could be associated with the structure of the chains. The nanotubes are expected to fill the

Table 3 Yield stress in Pa at various magnetic fields for the standard and dimorphic MRFs

Magnetic field (kA m^{-1})	MRF 2.5	MRF 6	Standard MRF
150	895	884	313
450	3974	4216	1801
750	6174	6352	3252
1050	6976	7213	4309

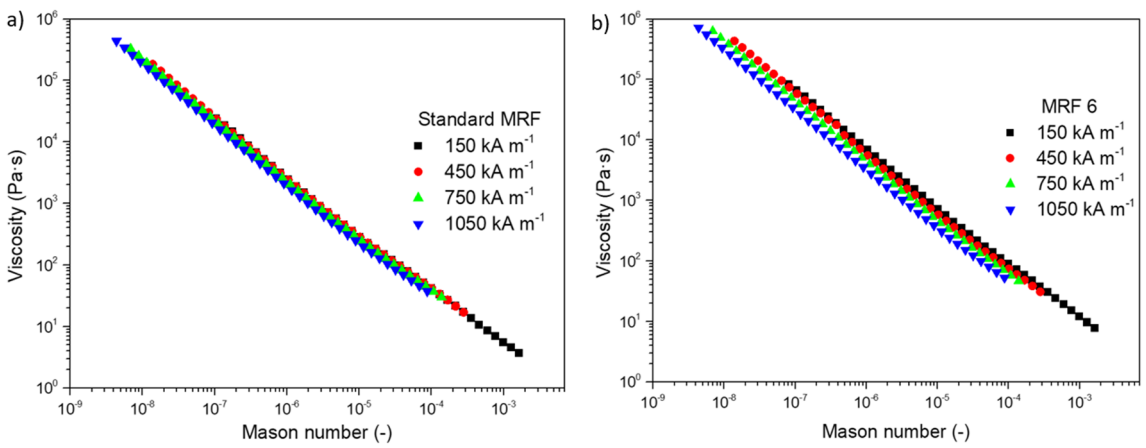

Fig. 8 Viscosity as a function of the Mason number at different magnetic fields and samples: **a** standard MRF and **b** MRF 6

gaps formed during the chain formation of the spheres rather than forming chain-like structures themselves, something that the current theory does not account for (López-López et al. 2005). This phenomenon makes the structures more robust which is reflected in Fig. 8b, as a decrease of Mn or increase of magnetic forces. To conclude, it is obvious that the Mn only describes well spherical systems of relevantly low polydispersity. Magnetorheological fluid studies with unique morphologies and components avoid to present measurements with Mn which should be presented to better understand the overall interactions.

As mentioned above, when a magnetic field is applied, magnetic particles form chain-like structures which cause a vast increase in the shear stress. To evaluate this increase, the stress ratio between the on- and the off-states is studied for different shear rates. The ratio (MR efficiency) is evaluated for all samples at two different magnetic fields, and the results are presented in Fig. 9.

The sample prepared using the PPy nanotubes/magnetite with higher content of magnetite (n=6) shows the highest shear stress increase, higher than the standard MRF with CI only, especially at lower shear rates. The MRF 2.5, on the other hand, displays the lowest stress increase especially in Fig. 9b. It is important to note that MRF 2.5 shows higher shear stress values in comparison with the standard MRF during the on-state as shown in Figure S1. However, the shear stress values during the off-state are also significantly higher due to the presence of rods in the system which keeps the spheres well dispersed and has a reflection in the shear stress values. Notably, at higher shear rates, the differences are less impactful for all samples. At lower magnetic fields, the addition of magnetic composite PPy/magnetite to the standard MRF plays a more pronounced role on the MR performance of the system.

The MR efficiency for the MRF 6 is 3.35 times higher than the standard MRF at 150 kA m^{-1} while only 1.95 times higher at 1050 kA m^{-1}. For the MRF 2.5 on the other hand, the ratio is 1.43 times lower than the standard MRF at 150 kA m^{-1}; however, at 1050 kA m^{-1}, the standard MRF is 3.65 times higher. This behaviour is attributed to the saturation magnetization of the magnetic composite PPy/magnetite which is achieved at lower fields when compared to the CI microspheres (Esmaeilzare et al. 2018), thus saturating "faster". A similar behaviour can be extracted from the yield stress values of Table 3. Thus, the nanotubes share stronger interactions at lower fields forming more robust chain-like structures. The same behaviour was observed for a different dimorphic study where rod-like particles similarly magnetically saturate at lower magnetic fields (Plachy et al. 2017). It can be concluded that the addition of magnetic composite PPy nanotubes/magnetite nanoparticles prepared using the mole ratio oxidant/pyrrole n=6 improved the MR efficiency especially at lower magnetic fields. In real applications, the MRFs are operating at elevated temperatures (McKee et al. 2018; Kumar Kariganaur et al. 2022a). Elevated temperatures may negatively affect the automobile's performance (Ramos et al. 2005; Pavlov 2017). Thus, it is important to evaluate the effect of the temperature on the MR properties of MRFs.

Temperature effect

Figure 10 shows a step-wise increase of magnetic field under steady shear for two different temperatures. During this process, the magnetic field is turned on and off while steadily increasing every 20 s. The sample was then redispersed and the test was repeated at an elevated temperature. For Fig. 10, the values for the 60 °C are shifted by 20 s for clarity.

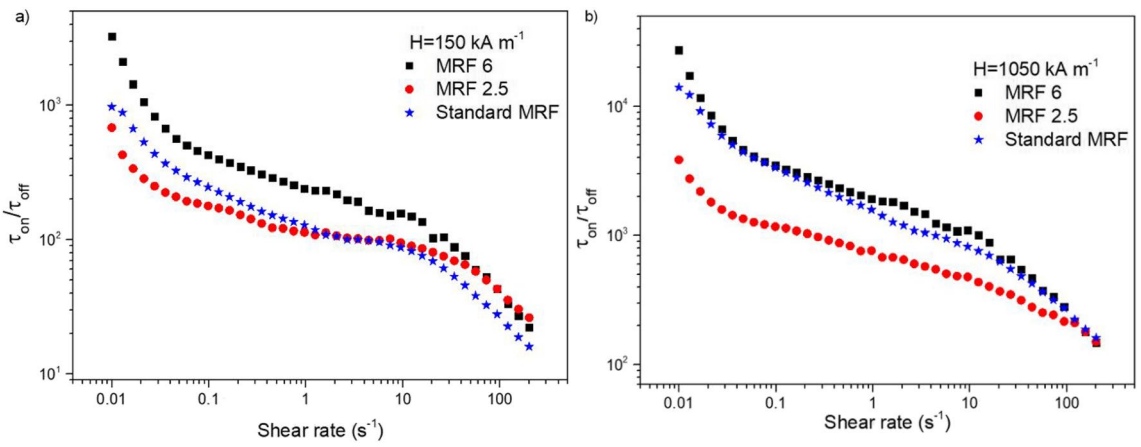

Fig. 9 Magneto-induced shear stress ratio as a function of shear rate for different samples and various magnetic fields: **a** 150 kA m^{-1} and **b** 1050 kA m^{-1}

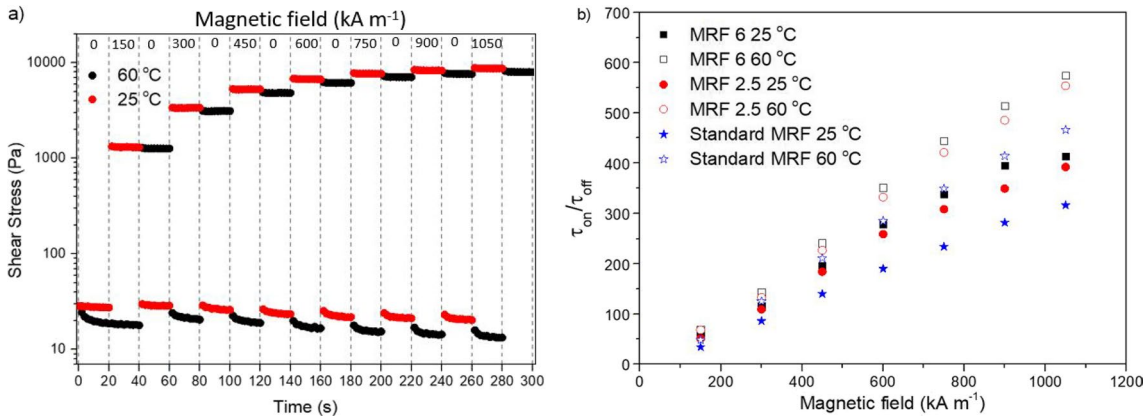

Fig. 10 **a** The effect of step-wise increase of the magnetic field on shear stress under a steady shear of 50 s^{-1} at different temperatures for the sample MRF 6. The changes of the magnetic field are illustrated with dotted lines with the values noted on top. The sample at 25 °C is shifted by 20 s for clarity reasons. **b** Shear stress ratio during the on- and off-state at different magnetic fields for different MRFs at two different temperatures

As can be seen, upon activating the magnetic field, the stress increased instantaneously. In addition, at 60 °C, despite the off-state stress being lower due to the shrinkage of the viscosity of the silicone oil, when the magnetic field is on, the stress values remain nearly the same. It can be concluded that in this case, the chain's strength has little dependence on the viscosity of the carrier as both chain-like structures are almost equally robust. An average shear stress value for the different magnetic fields was extracted, and the MR efficiency between the on- and off-state was then calculated. The results are plotted as a function of the magnetic field together with the rest of the samples (see supporting information) as shown in Fig. 10b.

Both bidisperse systems show a significant increase of their ratio for both temperatures in comparison with the standard MRF especially at higher magnetic fields. This can be explained by the interactions between the PPy nanotubes and CI microspheres. It is known that such bidisperse systems are arranged differently during the off-state (Adams et al. 1998). When a magnetic field is applied, it seems like the particles form the chain-like structures differently due to these interactions leading to a greater MR efficiency. Generally, the MR performances was improved for all samples at 60 °C. This is attributed to the lower shear stress values (thus viscosity) during the off-state while during the on-state, the viscosity values are preserved. Furthermore, several standard MRFs have been investigated at elevated temperatures of the same range with the MR performance showing a similar behaviour (Rabbani et al. 2015; McKee et al. 2018; Li et al. 2021).

Sedimentation assessment

Sedimentation stability is the biggest obstacle to overcome for MRFs as the magnetic particles form permanent aggregates reducing the MR properties of the MRFs. The sedimentation stability of the DMRFs and the standard MRF was studied under constant shear rate of 10 s^{-1} at 60 °C to simulate potential applications. The sedimentation was calculated as the stress of a given time over initial off-state stress. Figure 11 demonstrates the sedimentation stability over time. The sedimentation stability for the bidisperse samples is noticeably enhanced. Despite the elevated temperature which is proven to escalate sedimentation (Kumar Karigan-aur et al. 2022b, a), the dimorphic samples can be compared with other MRFs with increased stability (Sedlacik et al.

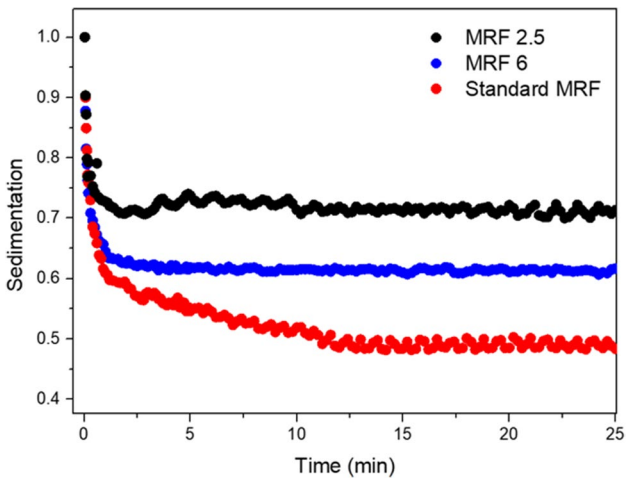

Fig. 11 Dynamic sedimentation tests for various MRFs at shear rate of 10 s^{-1} and 60 °C

2013). Additionally, the standard MRF reached steady state long after the DMRF. In the beginning, it seems like the spheres rapidly sediment; however, this increases the effective particle concentration, and as a result, the sedimentation process is slowed by the interactions of the spheres. The MRF 2.5 shows the best stability, which is attributed to the shape of the rods. As discussed in the particle morphology, the lower amount of magnetite resulted in a higher aspect ratio for the MRF 2.5. Thus, the rods in that specific sample should have stronger entropic repulsions which increases the overall stability. However, it can be assumed that there is sedimentation under shear which may affect the flow curves, especially for the lower shear rates (Russel 1980). The sedimentation of colloidal suspensions has been previously studied rheologically using different techniques showing similar results (Bazilevskii et al. 2010; Ovarlez et al. 2012). The same group showed that when fibres are added, there is a reduction of the sedimentation process similar to our case (Bazilevsky et al. 2017). From the latter, it can be concluded that the sedimentation obstacle must be addressed even during dynamic conditions for certain MRFs.

Conclusions

Two types of magnetic PPy nanotubes decorated with different amount of magnetite were synthesized using a novel method. The magnetic properties of these nanotubes are the highest among their kind and saturate faster than the standard CI spherical particles. A dimorphic magnetorheological suspension using microspheres and nanotubes was prepared. The overall flow behaviour of the dimorphic systems is similar to a standard MRF; however, the DMRFs showed higher magneto-induced shear stress increase. Through this study, it is revealed that faster saturating particles may significantly enhance the MRF's behaviour at lower fields. The samples were also tested at elevated temperatures closer to real applications. The nanotubular morphology helped the system to increase its MR effect. In addition, the stability of the fluids was studied dynamically. Despite the constant rotation of the geometry, the particles continued to settle. The addition of the nanotubes severely increased the viability of the MRFs by more than 50%. To conclude, the magnetic composite PPy nanotubes/magnetite nanoparticles improved both the rheological properties of the corresponding standard MRFs at room and elevated temperatures and their sedimentation stability.

Supplementary Information The online version contains supplementary material available at https://doi.org/10.1007/s00397-023-01409-9.

Funding Open access publishing supported by the National Technical Library in Prague. The authors A.M. and L.M. wish to thank the Internal Grant Agency of Tomas Bata University in Zlín (project no. IGA/CPS/2022/004) for its financial support. The authors A.M. and M.S. gratefully acknowledge project DKRVO (RP/CPS/2022/007), and author T.P. acknowledges project DKRVO (RP/CPS/2022/003) supported by the Ministry of Education, Youth and Sports of the Czech Republic.

Data availability Additionally, most raw data are provided in the SI.

Declarations

Competing interests The authors declare no competing interests.

References

Adams M, Dogic Z, Keller SL, Fraden S (1998) Entropically driven microphase transitions in mixtures of colloidal rods and spheres. Nature 393:349–352. https://doi.org/10.1038/30700

Ashtiani M, Hashemabadi SH, Ghaffari A (2015) A review on the magnetorheological fluid preparation and stabilization. J Magn Magn Mater 374:716–730. https://doi.org/10.1016/j.jmmm.2014.09.020

Bai X-X, Shen S, Wereley NM, Wang D-H (2019) Controllability of magnetorheological shock absorber: I. Insights, modeling and simulation. Smart Mater Struct 28:015022. https://doi.org/10.1088/1361-665X/aaf072

Bazilevskii AV, Koroteev DA, Rozhkov AN, Skobeleva AA (2010) Sedimentation of particles in shear flows of viscoelastic fluids. Fluid Dyn 45:626–637. https://doi.org/10.1134/S0015462810040125

Bazilevsky AV, Kalinichenko VA, Plyashkevich VA et al (2017) Sedimentation of particles in shear flows of viscoelastic fluids with fibers. Rheol Acta 56:787–799. https://doi.org/10.1007/s00397-017-1036-x

Bombard AJF, Gonçalves FR, Morillas JR, de Vicente J (2014) Magnetorheology of dimorphic magnetorheological fluids based on nanofibers. Smart Mater Struct 23:125013. https://doi.org/10.1088/0964-1726/23/12/125013

Chand M, Shankar A, Ali N et al (2014) An improved properties of bidispersed magneto-rheological fluids. RSC Adv. https://doi.org/10.1039/C4RA07431A

Cvek M, Jamatia T, Suly P et al (2022) Stable magnetorheological fluids containing bidisperse fillers with compact/mesoporous silica coatings. Int J Mol Sci 23:11044. https://doi.org/10.3390/ijms231911044

Cvek M, Mrlik M, Moucka R, Sedlacik M (2018) A systematical study of the overall influence of carbon allotrope additives on performance, stability and redispersibility of magnetorheological fluids. Colloids Surf A Physicochem Eng Asp 543:83–92. https://doi.org/10.1016/j.colsurfa.2018.01.046

Deng H, Gao Y, Hu R et al (2021) Self-sensing automotive magnetorheological dampers for low frequency vibration. Smart Mater Struct 30:115015. https://doi.org/10.1088/1361-665X/ac2c5f

de Vicente J, Klingenberg DJ, Hidalgo-Alvarez R (2011) Magnetorheological fluids: a review. Soft Matter 7:3701. https://doi.org/10.1039/c0sm01221a

Esmaeilzare A, Rezaei SM, Ramezanzadeh B (2018) Corrosion and magnetic properties of encapsulated carbonyl iron particles in aqueous suspension by inorganic thin films for magnetorheological finishing application. Appl Surf Sci 436:1200–1212. https://doi.org/10.1016/j.apsusc.2017.12.135

Fekry M, Elmesallamy SM, El-Rahman NRA et al (2022) Eco-friendly adsorbents based on abietic acid, boswellic acid, and chitosan/magnetite for removing waste oil from the surface of the water. Environ Sci Pollut Res 29:64633–64646. https://doi.org/10.1007/s11356-022-20169-2

Ivanova VT, Garina EO, Burtseva EI et al (2017) Conducting polymers as sorbents of influenza viruses. Chem Papers 71:495–503. https://doi.org/10.1007/s11696-016-0068-5

Jafari-Soghieh F, Maleki B, Behniafar H (2019) Effect of dendrimer-functionalized magnetic iron oxide nanoparticles on improving thermal and mechanical properties of DGEBA/IPD epoxy networks. High Perform Polym 31:24–31. https://doi.org/10.1177/0954008317749020

Jiang W, Zhang Y, Xuan S et al (2011) Dimorphic magnetorheological fluid with improved rheological properties. J Magn Magn Mater 323:3246–3250. https://doi.org/10.1016/j.jmmm.2011.07.024

Jonkkari I, Kostamo E, Kostamo J et al (2012) Effect of the plate surface characteristics and gap height on yield stresses of a magnetorheological fluid. Smart Mater Struct 21:075030. https://doi.org/10.1088/0964-1726/21/7/075030

Klingenberg DJ, Ulicny JC, Golden MA (2007) Mason numbers for magnetorheology. J Rheol (N Y N Y) 51:883–893. https://doi.org/10.1122/1.2764089

Kumar Kariganaur A, Kumar H, Arun M (2022a) Effect of temperature on sedimentation stability and flow characteristics of magnetorheological fluids with damper as the performance analyser. J Magn Magn Mater 555:169342. https://doi.org/10.1016/j.jmmm.2022.169342

Kumar Kariganaur A, Kumar H, Arun M (2022b) Influence of temperature on magnetorheological fluid properties and damping performance. Smart Mater Struct 31:055018. https://doi.org/10.1088/1361-665X/ac6346

Liao J, Ning C, Tan G et al (2014) Conducting polypyrrole nanotube arrays as an implant surface: fabricated on biomedical titanium with fine-tunability by means of template-free electrochemical polymerization. Chempluschem 79:524–530. https://doi.org/10.1002/cplu.201300385

Li H, Jönkkäri I, Sarlin E, Chen F (2021) Temperature effects and temperature-dependent constitutive model of magnetorheological fluids. Rheol Acta 60:719–728. https://doi.org/10.1007/s00397-021-01302-3

López-López MT, de Vicente J, Bossis G et al (2005) Preparation of stable magnetorheological fluids based on extremely bimodal iron–magnetite suspensions. J Mater Res 20:874–881. https://doi.org/10.1557/JMR.2005.0108

Marins JA, Plachý T, Kuzhir P (2019) Iron–sepiolite magnetorheological fluids with improved performances. J Rheol (N Y N Y) 63:125–139. https://doi.org/10.1122/1.5048051

Martínez-Cano Ó, Morillas JR, Cvek M et al (2023) High-speed videomicroscopy of sheared carbonyl iron suspensions. Smart Mater Struct 32:025004. https://doi.org/10.1088/1361-665X/acaadc

McKee M, Gordaninejad F, Wang X (2018) Effects of temperature on performance of compressible magnetorheological fluid suspension systems. J Intell Mater Syst Struct 29:41–51. https://doi.org/10.1177/1045389X17705203

Mori DI, Martin RM, Noble RD, Gin DL (2017) Cross-linked, polyurethane-based, ammonium poly(ionic liquid)/ionic liquid composite films for organic vapor suppression and ion conduction. Polymer (Guildf) 112:435–446. https://doi.org/10.1016/j.polymer.2017.01.064

Ngatu GT, Wereley NM, Karli JO, Bell RC (2008) Dimorphic magnetorheological fluids: exploiting partial substitution of microspheres by nanowires. Smart Mater Struct 17:045022. https://doi.org/10.1088/0964-1726/17/4/045022

Nikolaou M, Avraam K, Kolokithas-Ntoukas A et al (2021) Superparamagnetic electrospun microrods for magnetically-guided pulmonary drug delivery with magnetic heating. Mater Sci Eng: C 126:112117. https://doi.org/10.1016/j.msec.2021.112117

Ovarlez G, Bertrand F, Coussot P, Chateau X (2012) Shear-induced sedimentation in yield stress fluids. J Nonnewton Fluid Mech 177–178:19–28. https://doi.org/10.1016/j.jnnfm.2012.03.013

Ovarlez G, Rodts S, Chateau X, Coussot P (2009) Phenomenology and physical origin of shear localization and shear banding in complex fluids. Rheologica Acta, pp 831–844. https://doi.org/10.1007/s00397-008-0344-6

Parisi D, Vlassopoulos D, Kriegs H et al (2022) Underlying mechanism of shear-banding in soft glasses of charged colloidal rods with orientational domains. J Rheol (N Y N Y) 66:365–373. https://doi.org/10.1122/8.0000400

Park J-Y, Kim G-W, Oh J-S, Kim Y-C (2021) Hybrid multi-plate magnetorheological clutch featuring two operating modes: fluid coupling and mechanical friction. J Intell Mater Syst Struct 32:1537–1549. https://doi.org/10.1177/1045389X20988086

Pavlov N (2017) Influence of shock absorber temperature on vehicle ride comfort and road holding. MATEC Web Conf 133:02006. https://doi.org/10.1051/matecconf/201713302006

Plachy T, Cvek M, Kozakova Z et al (2017) The enhanced MR performance of dimorphic MR suspensions containing either magnetic rods or their non-magnetic analogs. Smart Mater Struct 26:025026. https://doi.org/10.1088/1361-665X/aa56ef

Plachy T, Sedlacik M, Pavlinek V et al (2013) An effect of carbonization on the electrorheology of poly(p-phenylenediamine). Carbon N Y 63:187–195. https://doi.org/10.1016/j.carbon.2013.06.070

Qiu G, Wang Q, Nie M (2006) Polypyrrole-Fe_3O_4 magnetic nanocomposite prepared by ultrasonic irradiation. Macromol Mater Eng 291:68–74. https://doi.org/10.1002/mame.200500285

Rabbani Y, Ashtiani M, Hashemabadi SH (2015) An experimental study on the effects of temperature and magnetic field strength on the magnetorheological fluid stability and MR effect. Soft Matter 11:4453–4460. https://doi.org/10.1039/C5SM00625B

Ramos JC, Rivas A, Biera J et al (2005) Development of a thermal model for automotive twin-tube shock absorbers. Appl Therm Eng 25:1836–1853. https://doi.org/10.1016/j.applthermaleng.2004.11.005

Russel WB (1980) Review of the role of colloidal forces in the rheology of suspensions. J Rheol (N Y N Y) 24:287–317. https://doi.org/10.1122/1.549564

Sedlacik M, Pavlinek V (2017) Magnetorheology of dimorphic magnetorheological fluids based on iron nanorods. J Phys Conf Ser 790:012031. https://doi.org/10.1088/1742-6596/790/1/012031

Sedlacik M, Pavlinek V, Vyroubal R et al (2013) A dimorphic magnetorheological fluid with improved oxidation and chemical stability under oscillatory shear. Smart Mater Struct 22:035011. https://doi.org/10.1088/0964-1726/22/3/035011

Stejskal J, Sapurina I, Vilčáková J et al (2021b) Conducting and magnetic composites polypyrrole nanotubes/magnetite nanoparticles: application in magnetorheology. ACS Appl Nano Mater 4:2247–2256. https://doi.org/10.1021/acsanm.1c00063

Stejskal J, Sapurina I, Vilčáková J et al (2021a) One-pot preparation of conducting melamine/polypyrrole/magnetite ferrosponge. ACS

Appl Polym Mater 3:1107–1115. https://doi.org/10.1021/acsapm.0c01331

Stejskal J, Trchová M (2018) Conducting polypyrrole nanotubes: a review. Chem Papers 72:1563–1595. https://doi.org/10.1007/s11696-018-0394-x

Stejskal J, Trchová M, Bober P et al (2016) Polypyrrole salts and bases: superior conductivity of nanotubes and their stability towards the loss of conductivity by deprotonation. RSC Adv 6:88382–88391. https://doi.org/10.1039/C6RA19461C

Thiagarajan S, Koh AS (2021) Performance and stability of magnetorheological fluids—a detailed review of the state of the art. Adv Eng Mater 23:2001458. https://doi.org/10.1002/adem.202001458

Upadhyay J, Kumar A (2013) Engineering polypyrrole nanotubes by 100MeV Si9+ ion beam irradiation: enhancement of antioxidant activity. Mater Sci Eng: C 33:4900–4904. https://doi.org/10.1016/j.msec.2013.08.009

Wang F, Ma Y, Zhang H et al (2021a) Rheological properties and sedimentation stability of magnetorheological fluid based on multi-walled carbon nanotubes/cobalt ferrite nanocomposites. J Mol Liq 324:115103. https://doi.org/10.1016/j.molliq.2020.115103

Wang G, Geng J, Qi X et al (2021b) Rheological performances and enhanced sedimentation stability of mesoporous Fe_3O_4 nanospheres in magnetorheological fluid. J Mol Liq 336:116389. https://doi.org/10.1016/j.molliq.2021.116389

Wang G, Ma Y, Cui G et al (2018) Two-dimensional Fe_3O_4/MoS_2 nanocomposites for a magnetorheological fluid with enhanced sedimentation stability. Soft Matter 14:1917–1924. https://doi.org/10.1039/C7SM02425H

Wang X, Gordaninejad F (2006) Study of magnetorheological fluids at high shear rates. Rheol Acta 45:899–908. https://doi.org/10.1007/s00397-005-0058-y

Wereley NM, Chaudhuri A, Yoo J-H et al (2006) Bidisperse magnetorheological fluids using Fe particles at nanometer and micron scale. J Intell Mater Syst Struct 17:393–401. https://doi.org/10.1177/1045389X06056953

Zainordin AZ, Mohamed Z, Ahmad F (2021) Magnetorheological fluid: testing on automotive braking system. Int J Automot Mech Eng 18:8577–8584. https://doi.org/10.15282/ijame.18.1.2021.16.0651

Paper 3

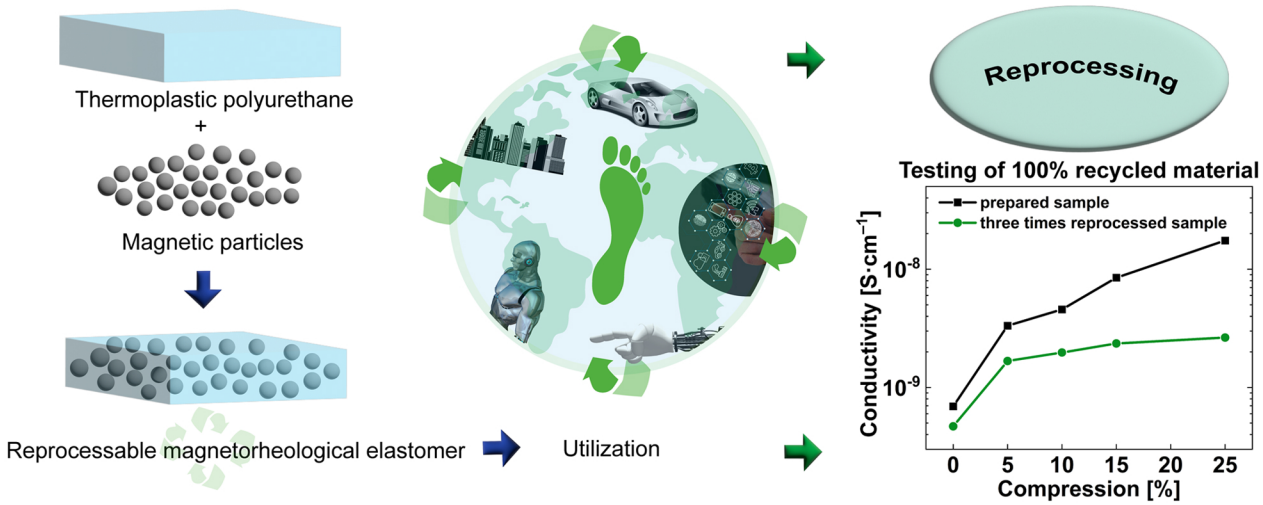

Nature Portfolio
Scientific Reports
Accepted 5th July 2022

scientific reports

Check for updates

OPEN

Reprocessed magnetorheological elastomers with reduced carbon footprint and their piezoresistive properties

A. Munteanu[1], A. Ronzova[1,2], E. Kutalkova[1], P. Drohsler[1], R. Moucka[1,3], M. Kracalik[4], O. Bilek[2], S. A. Mazlan[5] & M. Sedlacik[1,2]✉

Despite the vast amount of studies based on magnetorheological elastomers (MREs), a very limited number of investigations have been initiated on their reprocessing. This paper presents a new type of recyclable MRE which is composed of thermoplastic polyurethane (TPU) and carbonyl iron particles (CI). The chosen TPU can be processed using injection moulding (IM), followed by several reprocessing cycles while preserving its properties. Numerous types of injection moulded and reprocessed MREs have been prepared for various particle concentrations. The effect of thermo-mechanical degradation on the recycled MREs has been investigated while simulating the reprocessing procedure. An apparent decrease in molecular weight was observed for all the examined matrices during the reprocessing cycles. These changes are attributed to the intermolecular bonding between the hydroxyl groups on the surface of the CI particles and the matrix which is studied in depth. The effect of reprocessing and the presence of magnetic particles is evaluated via tensile test, magnetorheology and piezoresistivity. These characterization techniques prove that the properties of our MREs are preserved at an acceptable level despite using 100% of recyclates while in real applications only up to 30% of recycled material is generally used.

Smart or intelligent materials are able to substantially change their material properties under an external stimulus, such as stress, electromagnetic radiation, pH, electrical or magnetic field[1,2]. A unique type of such smart materials are the magnetorheological elastomers (MREs) which are consisted of magnetic microparticles embedded in an elastomeric matrix. These composites are mostly known for their controllable viscoelastic character which can be tuned with an external magnetic field[3]. As a result, these elastomers can be used in a huge variety of applications. The most common field for applications is engineering which involves vibration absorbers, actuators and dampers[4,5]. Other notable applications include electromagnetic shielding, sensors and flexible electronics[6–8]. Lately medical applications use the MREs as fluid transportation, artificial muscles and cell substrates[9–14]. It is clear that the usage of the MREs constantly increases which arises the need of reusability of these elastomers. Recycling is an important aspect of product design from both environmental and economical point of view. However, not many MREs are investigated in this regard, as most of them are not able to undergo such procedures.

A good solution for these elastomers is the selection of an appropriate filler and matrix with the ability to undergo several recycling processes. Carbonyl iron (CI) is the most common filler used in MREs due to its superior magnetic properties and stability[15]. In terms of reprocessing, exposure to high temperatures can lead to inferior magnetic particles, however polymers are usually reprocessed at much lower temperatures[16]. A sufficiently flexible elastomer including synthetic silicone matrices[17], nitrile rubbers[18], and polyurethanes[19,20] represent the second important component of the most common MREs. The complexity of reusing these MREs is related to the crosslinked structure of the composite's matrix. In contrast to crosslinked matrices, thermoplastic elastomers (TPEs) can be melted and reused[21,22]. Thermoplastic elastomers can compete with vulcanized rubbers at room

[1]Centre of Polymer Systems, University Institute, Tomas Bata University in Zlín, Trida T. Bati 5678, 760 01 Zlín, Czech Republic. [2]Department of Production Engineering, Faculty of Technology, Tomas Bata University in Zlín, Vavreckova 275, 760 01 Zlín, Czech Republic. [3]Polymer Centre, Faculty of Technology, Tomas Bata University in Zlín, Vavreckova 275, 760 01 Zlín, Czech Republic. [4]Institute of Polymer Science, Johannes Kepler University Linz, Altenberger Straße 69, 4040 Linz, Austria. [5]Engineering Materials and Structures (eMast) iKohza, Malaysia-Japan International Institute of Technology (MJIIT), Universiti Teknologi Malaysia, Jalan Sultan Yahya Petra, 54100 Kuala Lumpur, Malaysia. ✉email: msedlacik@utb.cz

temperature in terms of their mechanical properties and difficulty of processing. The main difference between TPE and vulcanized rubbers can be found in the structure of the polymer network. Vulcanized rubbers share stronger networks, a property obtained from the disulfide bonds, however they are not fit for reprocessing. The balanced properties of the TPEs originate from their microstructure, which is generated by alternating mutually immiscible soft and hard elastomeric segments with a distinctly different glass transition temperature[23].

Considering the broad utilization of MREs, they have to be highly functional and tide over some difficulties. The properties of the MREs are greatly affected by the magnetic properties of the particles, their concentration and microstructure which is either a well-dispersed isotropic state or directed in an anisotropic arrangement[24]. In addition, the flexibility of the matrix is crucial for maintaining specific properties for example the MR effect[7]. The MR effect describes the difference of the matrix's stiffness before and after the application of a magnetic field[25]. Most studies use the shear storage (G') and the loss modulus (G'') to evaluate the MR effect[26,27]. An excess amount of particles in the matrix enhances the MR effect however, highly filled MREs usually suffer from the Payne effect which could significantly limit their applications. The Payne effect is observed as a simultaneous rapid decrease of the G' and a local maximum of G'' above certain values of deformation. It is a common behaviour for elastomers embedded with a filler at high concentrations and it is based on changes in the microstructure of the material[28]. Nevertheless, this phenomenon is rather ignored in the literature dealing with MREs and thus needs to be further investigated.

In this study, we use a thermoplastic polyurethane (TPU) as a MRE which can be processed and recycled while competing with its analogous in terms of MR performance. These properties of the TPU originate from its structure which is composed of a two-phase chemically bonded soft and hard segments[29]. TPU-based composites are used in a wide range of applications[30–32] however, their presence in MREs is rather limited[20,33,34]. We simulate the processing conditions and evaluate their effects on the structure and molecular properties of the matrices. In addition, we characterize the samples in terms of mechanical and MR performance using industrial-friendly equipment. Lastly, we prove that these MREs are suitable for piezoresistive applications. Piezoresistive sensors have been investigated for decades[35,36] leading to a significant improvement in a variety of state-of-the-art robotics[37]. Our MREs are able to detect external forces under deformation converting them into a change of resistivity thus allowing them to be used as sensors.

Experimental

Materials and fabrication of the MREs. The CI particles (CN grade, iron content > 99.5%, $d_{50} = 6.5$–8.0 μm; BASF, Germany) were used as the magnetic filler for the preparation of MREs. Elastolan® 35A12P (BASF, Germany; 37 Shore A hardness) was chosen as an appropriate TPU matrix. The MREs were prepared by mixing the CI particles with the TPU matrix in various concentrations from 30 to 80 wt%. The samples with the most diverse and representative results are presented here including 30, 50 and 80 wt%. The mixing was performed using a twin-screw counter-rotating mixer supplied by Brabender (Duisburg, Germany). Each matrix was prepared at 170 °C, following 1-min dosing of the mixture and its compounding for 4 min at 50 rpm. In addition to composite samples, a neat matrix was also subjected to the mixing process in order to investigate the effect of its degradation and to compare its mechanical properties with the MREs. After cooling, the homogeneous matrices were cut into small pieces so they can be processed with IM. The IM was executed using HAAKE MiniJet Pro—Piston IM System (Thermo Scientific, Germany) and disk-shaped samples of 25 and 1.23 mm in diameter and height, respectively, and standard dog-bone tensile specimens (type 5 according to ISO 527) with the same thickness were produced. During the IM of filled samples, the optimal parameters, such as the temperature of the cylinder, temperature of the mould, the injection pressure/time and post-pressure/time, were set up 190 °C, 30 °C, 450 bar/7 s, and 350 bar/3 s, respectively. The same parameters were set up for neat samples (TPU) with the exception of the temperature of cylinder which was set at 180 °C. The prepared samples were labelled as raw material (R0) and characterized by the methods below. Consequently, the samples were further cut into small pieces, compounded, injected under the same conditions as stated above, and labelled as recycled material (R1). The whole process of mixing and IM was repeated 3 times thus fabricating recycled samples labelled R1–R3.

Degradation process analysis. The effect of recycling on the pure TPU matrix was studied by Fourier-transform infra-red spectroscopy (FTIR). The measurements were performed on FTIR instrument Nicolet 6700 (Nicolet, USA) supplied with an ATR-accessory with a diamond crystal under laboratory temperature with the spectra resolution of 2 cm^{-1} from 64 scans, in the range of 4000–700 cm^{-1}, however the region between 2000 and 2800 cm^{-1} is not presented due to the intrinsic absorption of the diamond crystal. The weight average molecular weight (M_w), the number average molecular weight (M_n), and the polydispersity index ($Đ = M_w/M_n$) of the tested samples were determined from the peaks corresponding to the polymer fraction according to the absolute calibration method by the gel permeation chromatography (GPC) method using a Waters HPLC system, equipped with a Waters model e2695 and a Waters model 2414 differential refractometer (Waters Corporation, Milford, USA). The samples were dissolved in tetrahydrofurane (THF) (2–3 mg mL^{-1}), then stabilized with butylated hydroxytoluen (BHT) (240 mg L^{-1}) and lastly, filtered using a syringe filter (0.45 μm). The separation was carried out using a series of gel-mixed bed columns (Polymer Laboratories Ltd, Shropshire, UK) as follows: 1 × PLgel-Mixed-A bed column (300 × 7.5 mm, 20 μm), 1 × PLgel-Mixed-B bed column (300 × 7.5 mm, 10 μm), and 1 × PLgel-Mixed-D bed column (300 × 7.5 mm, 5 μm); the mobile phase containing the THF was stabilized with BHT (240 mg L^{-1}) at 40 °C. The flow rate of the mobile phase was set to 1.0 mL min^{-1} and the injection volume equal to 100 μL. All data were analysed using the Empower 3 software.

The reflection spectra of the TPU samples with the same dimensions as used in rheological analysis (see below) were analysed using a Lovibond RT850i (Tintometer Ltd) equipped with xenon pulse light. For the colorimetric evaluation the matrices were taken from the original pellet and then processed through IM. The

measurement of reflection spectra in the range of 360–750 nm was performed with a 10-mm aperture size and d/8° observation geometry. The average whiteness index (WI) was evaluated from the obtained spectrum by averaging 10 measurements at various positions on the sample according to ASTM E313-20. The glass transition temperature (*T*g) of the soft segments of the matrices was investigated via a differential scanning calorimetry (DSC) method using the Gas Controller GC100 (Mettler Toledo, Switzerland). The samples were prepared with similar weights (≈ 6 mg) and measured for a temperature range of – 40 to 250 °C using heating and cooling rates of 20 °C min^{-1} under nitrogen atmosphere. The *T*g of the soft segments was evaluated using the half-height technique in the transition regime. The error for each *T*g was taken as the average temperature step for each measuring point.

Rheology. The rheological properties of the TPU elastomers were characterized using the rotational rheometer Physica MCR 502 (Anton Paar, Graz, Austria). The magnetorheological measurements were performed using a magneto-cell (Physica MRD 180/1 T). The samples were exposed to various external magnetic fields up to 750 kA m^{-1}. To perform the degradation study, a water-cooled Peltier system (Physica H-PTD 200) was equipped, which enables one to reach temperatures up to 180 °C to simulate the processing conditions. For both accessories, a parallel-plate geometry was used. The diameters of plates were 20 and 25 mm for the magneto-cell and the Peltier, respectively. In addition, the geometry used for magnetorheological measurement was sand-blasted and 0.5 N normal force was applied during the measurement for the elastic samples to eliminate any possible wall-slip at low shear rates. All measurements were performed in the linear viscoelastic regime (LVE) where the modulus is independent of strain. The LVE was identified using dynamic strain sweeps for strains between 0.001 and 10% at the frequency of 1 rad s^{-1}. At elevated temperatures, the samples were tested under inert atmosphere using nitrogen. Finally, dynamic time sweeps were performed at 1 rad s^{-1} until the elastomers reached a steady state for samples unaffected by thermal degradation. For the neat samples, further frequency sweeps were performed in the 0.1–100 rads s^{-1} regime.

Mechanical testing. The samples for tensile tests were produced directly in the shape of the test specimen according to the requirements of the standard test method using the IM process. The tensile properties of the TPU matrix as well as the MREs were investigated using the tensile testing machine M350-5 CT (Testometric Company, Lancashire, UK) with a cross-head speed of 500 mm min^{-1}. The measurements were performed according to the ASTM D638 standard test method at the room temperature and subsequently the results of the tensile strength were evaluated as an arithmetic mean using 5 samples of type 5. The standard deviation was obtained using five test specimens from the stress–strain dependencies. The coefficient of variation among all the tested variants of samples was lower than 10% and 12% for tensile strength and for Young's modulus, respectively.

Piezoresistivity testing. To determine the piezoresistive properties, an electrometer (Keithley 6517A, USA) coupled with a tensile machine (M3750-5CT, Testometric, UK) and supplied with a load cell with a maximum capacity of 5 kN was used. Cylindrical samples with 4 mm high and 10 mm in diameter were sandwiched between two gilded brass electrodes and were gradually compressed narrowing their mutual distance by up to 25% of their initial spacing (sample height) at the rate of 5 mm min^{-1}. The deformations were set to 5, 10, 15, 25% of the height of the sample and were kept for the period of 1 min during which conductivity (later converted to resistivity as a reciprocal value) was measured. The measurements were performed at room temperature. The conductivity (σ) was calculated from the measured current–voltage dependencies according to the following formula:

$$\sigma = \frac{I}{U}\frac{t}{A} \tag{1}$$

where *t* is the sample thickness (distance of electrodes) for given deformation, *A* is the nominal area of the sample (electrode), *I* is the electric current, and *U* is the voltage.

Results and discussion

Degradation process analysis. The degradation of TPU was examined by FTIR spectra for each reprocess cycle. In Fig. 1, the reprocessing cycles spectra of neat TPU matrix can be observed. The graph displays a peak at 3300 cm^{-1} which represents an N–H stretching. It is clear, that the N–H group is reduced during reprocessing. Moreover, the figure shows characteristic peaks at 2900 and 2800 cm^{-1} of asymmetric and symmetric C–H stretching, respectively. These peaks drop with each reprocess cycle which can be attributed to the mechanical and thermal degradation.

In addition, Fig. 1 displays a peak at 1700 cm^{-1}, which corresponds to an ester linkage, which is typical during the reprocessing of such matrices[38]. Finally, aromatic amine C–N groups were identified from the peaks between 1300 and 1250 cm^{-1} which are more pronounced with each recycling. The reason behind the C–N stretching is explained in detail later on. It can be concluded that FTIR spectra prove certain chemical changes in the matrix during reprocessing.

Gel permeation chromatography. Gel permeation chromatography analysis is an important method for the determination of the polymer's molecular weight and molecular weight distribution, which can be used to track the degradation process during processing. Table 1 shows the changes in the chain length, expressed as M_w for different recycling cycles. The effect of magnetic filler on chemical changes during IM process, followed by

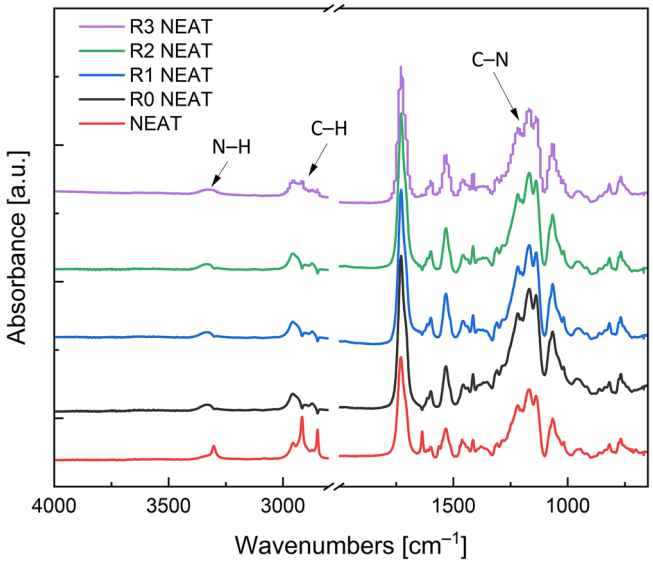

Figure 1. FTIR analysis of neat TPU matrix for each reprocessing cycle.

	Treatment	M_n (g mol^{-1})	M_w (g mol^{-1})	$Đ$ (–)
R0 NEAT	IM	63,600 ± 2100	131,600 ± 2100	2.07 ± 0.06
R1 NEAT	IM/one times recycling process	58,600 ± 900	119,900 ± 700	2.05 ± 0.05
R2 NEAT	IM/two times recycling process	57,300 ± 700	115,600 ± 600	2.02 ± 0.01
R3 NEAT	IM/three times recycling process	57,700 ± 1200	115,200 ± 1300	2.00 ± 0.02
R0 80 wt%	IM	53,100 ± 4200	98,800 ± 2200	1.87 ± 0.11
R1 80 wt%	IM/one times recycling process 80 wt% filled	55,600 ± 900	100,600 ± 200	1.81 ± 0.03
R2 80 wt%	IM/two times recycling process 80 wt% filled	50,800 ± 300	88,600 ± 100	1.74 ± 0.01
R3 80 wt%	IM/three times recycling process 80 wt% filled	46,400 ± 900	81,500 ± 1100	1.76 ± 0.01

Table 1. Molecular weights and polydispersity index obtained from GPC measurements.

three processes of recycling is observed using the GPC method. In general, heat treatment of neat TPU induced a reduction in M_w caused by thermal degradation of the polymer chains. However, during the 2nd and 3rd recycling process, these values became almost unchanged, probably reaching equilibrium originating from the simultaneous degradation and accumulation of processes in the TPU[23,39].

An apparent decrease in M_w and $Đ$, was observed for the 80 wt% composite in contrast to the TPU sample, indicating a chain shortening due to the presence of CI particles. In the first recycling cycle, higher values of M_w and M_n were observed. This phenomenon indicates the probable bonding of the chains with the particles during the thermal stress in the composite processing. As the number of melt agitations increases, the chains shorten and the M_w and M_n values decrease, indicating that the degradation processes prevail over the recombination[40]. The abovementioned results revealed that excessive mixing of the melt with CI particles resulted in a more significant reduction of the molecular weight for the 80 wt% polymer by up to ~ 18%, rather than the neat TPU where the reduction was only ~ 13%.

Colorimetry evaluation. An additional degradation study, relevant to the industry, was conducted through whiteness index (WI) measurements. In Fig. 2, the values of the WI are demonstrated for the same matrix during different processing states. Initially, the WI dropped by half after the matrix underwent the first IM process. This could be attributed to the degradation of the elastomer and the by-products of processing as mentioned above. Thereafter, the recycled samples share very similar values of WI indicating the same overall product. The filled matrices could not be measured due to the high concentrations of the particles. To conclude, despite this method being mainly complementary, the colour assignment for recycled products is a quick and a practical test.

Mechanical testing. Tensile strength tests were conducted to study in depth the mechanical behaviour of the neat and filled TPUs. The tensile properties were measured five times for each processing cycle. The most representative stress–strain curves for each sample for both neat and filled matrices are displayed in Fig. 3. The trend of the curves for neat matrix demonstrates that the samples break at high elongations. This indicates that the matrix is consisted mostly of elastomeric segments as these curves are typical for a rubber-like materials. The

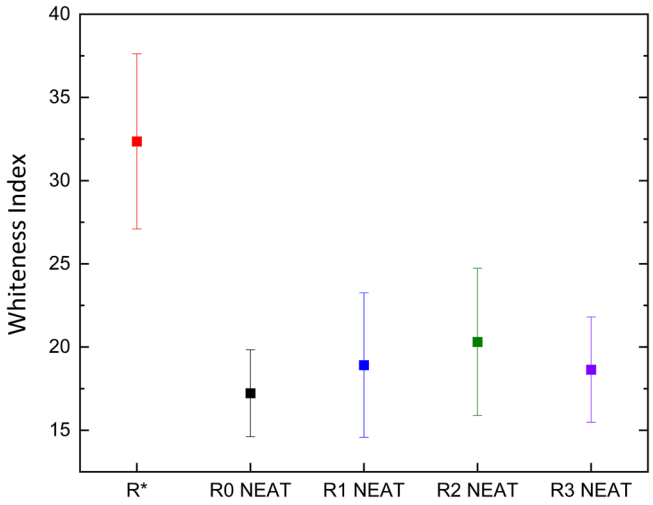

Figure 2. Whiteness Index values for the original pellet (R*), matrices obtained through IM process (R0) and further reprocessing (R1–R3).

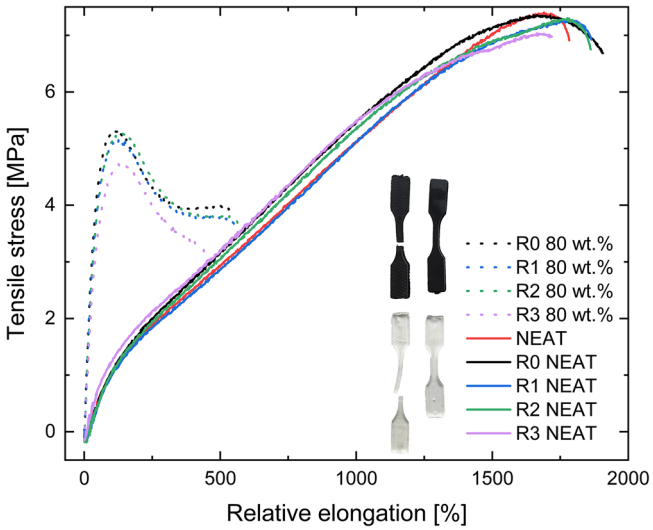

Figure 3. Tensile strength properties for unfilled neat TPU matrix (full line) and 80 wt% filled TPU matrix (dot line).

MREs on the other hand, break at shorter elongations as the magnetic particles cannot deform above a certain point forcing the matrix to be extended, thus the deformation that the polymeric part feels is greater than the one that the machine imposes. All the MREs samples certainly show a very similar strain hardening and necking which ends up in a break at similar values of stress.

The maximum elongation at break differs for every recycling process of the neat TPUs, however the differences between the samples is negligible, only R3 possesses a little bit lower elongation. It can be clearly concluded from the Fig. 3 that the selected matrix is suitable for reprocessing as the matrices retain their mechanical properties during each reprocessing cycle. As shown in the graph, the filled matrix has a very similar trend to the R0 after the first two reprocessing cycles with virtually the same maximum elongation and slightly lower tensile stress.

On the other hand, the third recycling cycle shows significantly lower both elongation at break and tensile stress, which can be attributed to the degradation process caused by recycling and potential bonding between the matrix and the CI particles during the reprocessing.

Additionally, the comparison of the neat and filled TPUs reveals qualitatively different behaviour. The first difference can be seen at post-yield behaviour where the unfilled matrices have no visible strain softening whereas the filled material has distinctive stress drop beyond yield point. Furthermore, as can be observed from the Fig. 3, the unfilled materials are capable of sustaining enormous elongation with partial reversible deformation, unlike the filled analogues, in which the presence of the CI particles resulted in three times lower elongation at break. This disparity is caused by the high filling of the matrix, and the presence of the CI particles which also causes the higher fragility of the filled system. The tensile strength was also greatly reduced as shown in Fig. 4, however,

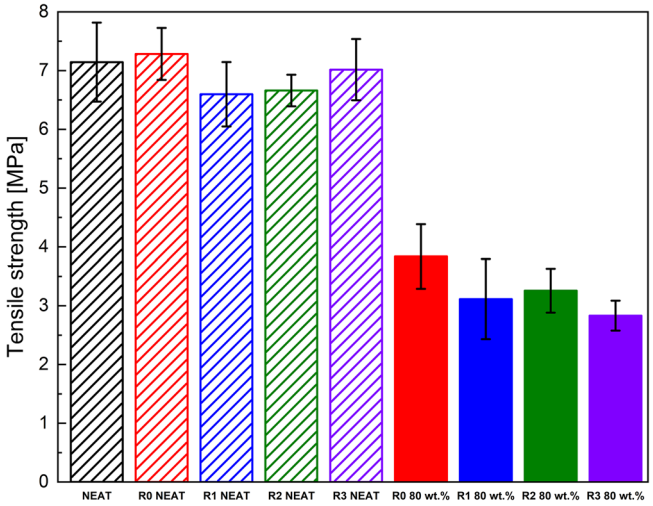

Figure 4. Tensile strength of the neat and 80 wt% filled TPU samples.

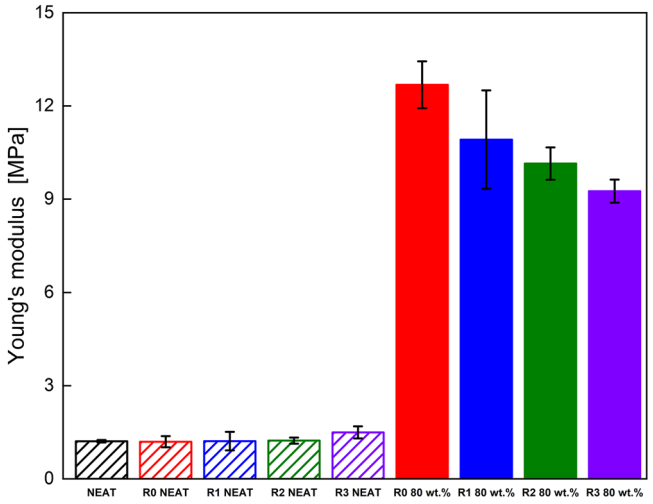

Figure 5. Young's modulus of the neat and 80 wt% filled TPU matrices.

the ultimate strength was less affected. Furthermore, Fig. 5 confirms that the filled matrices need higher stress to achieve the same deformation resulting in a higher Young's modulus for the filled elastomers.

Analysing the Young's modulus of the filled and unfilled samples, it can be concluded that the neat matrices have almost the same Young's modulus for all recycling cycles despite the small degradation. On the contrary, for the filled samples, a light drop of Young's modulus is observed with each recycling. It is generally known, that rigid particles increase Young's moduli of elastomers[41], in this case it can be also assumed that with an application of external magnetic field the moduli would increase even higher[42] which contributes to their future applications and will be shown later on.

Rheology and glass transition temperature. To compare the structure of the recycled neat TPU matrices, dynamic frequency sweeps were performed at 150 °C, as shown in Fig. 6. At high frequencies, the recycled matrices show no difference from each other. It seems that the values of *G'* for these samples will converge at even higher frequencies. On the other hand, the recycled samples show a reduced *G'* at lower frequencies, however the difference is not very significant. This decrease is not proportional to the reprocessing cycles and the elastic modulus differs approximately by 10% with each cycle. Generally, the *G'* is reduced except for the case of R2. This behaviour is known to generally follow the tensile stress trend[40]. The abovementioned trend is the same as the tensile stress in Fig. 6. A possible explanation of the drop could be associated with the degradation of the TPU matrix as mentioned above[29]. The shorter chains would disentangle faster for matrices with lower molar mass. Another possible explanation would be the oxidation of the outer layer of the matrices which could decrease the material's strength during processing[43]. Nevertheless, the outcome of the changes caused by the third recycling process in terms of *G'* seems to be minor from a practical point of view.

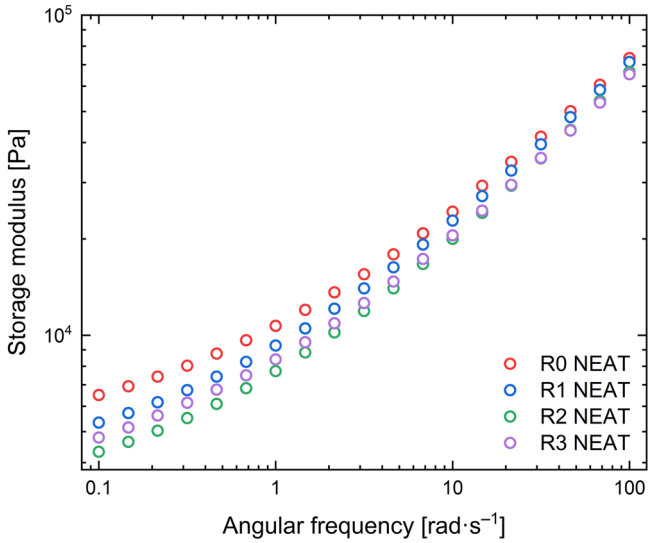

Figure 6. Dynamic frequency sweeps for the neat TPU samples at 150 °C.

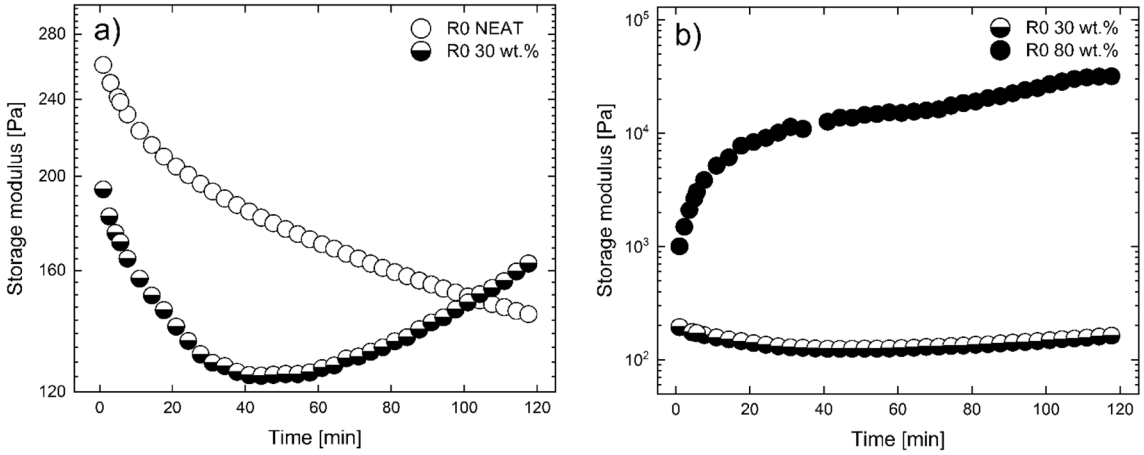

Figure 7. Dynamic time sweeps for (**a**) R0 PURE open circles and R0 30 wt% half open circles and (**b**) R0 30 wt.% half open circles and R0 80 wt.% filled circles.

In order to simulate the sample during the recycling process, dynamic time sweep tests (angular frequency 1 rad s^{-1} and strain within LVE) were performed at 170 °C for specific samples. In Fig. 7, the neat TPU matrix is compared with their filled analogue. The neat matrix shows a typical polymeric behaviour with the *G'* decreasing with time until the chains are relaxed and *G'* becomes independent of time. The abovementioned behaviour could hinder a degradation process; however, it cannot be evaluated for this matrix with this method. Moreover, based on the last observation, it can be confirmed that a potential curing or crosslinking process (if any) is insignificant due to the decreasing trend of *G'*. The 30 wt% filled matrix, on the other hand, shows a similar drop of *G'* for the first 50 min before a noteworthy increase of *G'* is observed. This can be attributed to the covalent bonding which occurs between the bare CI particles and the matrix[44]. These particles are covered with hydroxyl groups at their surface which can react with the end-groups of the TPU chains[45,46]. The abovementioned statement is further supported by *Fig. 7 b)* in which two MREs with different concentrations are compared. It can be clearly seen that for the 80 wt% filled matrix, the increase of the *G'* starts immediately and is orders of magnitude higher than the 30 wt% MRE. In addition, the behaviour for the 80 wt% is very important in the present study as this increase takes place during the same time-window as the fabrications and recycling process. On the other hand, for 30 wt% this increase can be considered insignificant as it can only be noticed after 50 min, which corresponds to more than ten reprocessing cycles.

It is worth mentioning that a similar test was performed with the sample exposed to O_2 by removing the hood which provided a N_2 based environment. A sharp increment of *G'* was observed for all samples due to reactions with oxygen. The latter behaviour can lead to inferior magnetic particles formation (iron oxidation), but such by-products are formed at much higher temperatures[16]. In Fig. 7 though, all matrices are under dormant conditions.

	R0	R1	R2	R3
Tg (±0.3 °C)	− 17.4	− 13.1	− 14.5	− 14.4

Table 2. The Tg values of the soft segments at different reprocessing cycles for the 80 wt% MRE.

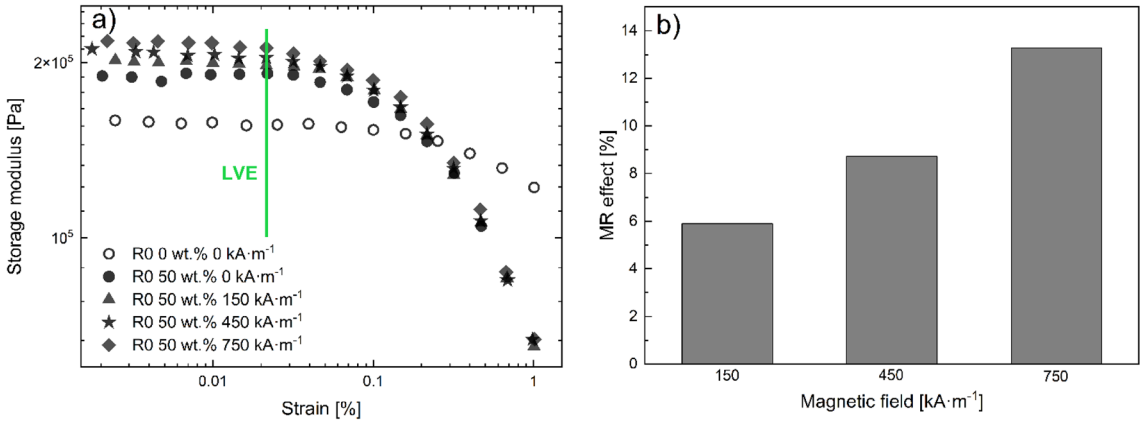

Figure 8. (**a**) Dynamic strain sweeps for samples containing 50 wt% CI particles at different magnetic fields (filled symbols; circles 0 kA m^{-1}; triangles 150 kA m^{-1}; stars 450 kA m^{-1}; diamonds 750 kA m^{-1}); neat TPU matrix (unfilled) and (**b**) MR effect for the same 50 wt% matrix.

The *Tg* of the soft segments was evaluated using the DSC method as it is a critical parameter for magnetorheology[34]. The *Tg* values for the TPU 80 wt% MREs are shown in Table 2. An apparent increase of *Tg* is observed after the first reprocessing. There are two main reasons for the *Tg* to increase. The first indicates an incensement in *Mw*, however, considering the GPC measurements that is not the case. The second and most probable reason is the limited mobility of the chains or their stiffening. It has been reported that TPU matrices are prone to intermolecular bonding during processing[47]. It has been observed for particles other than CI to bond with this matrix[48]. As a result, the mobility of the chains is reduced leading to higher values of *Tg*. As shown in Fig. 8b, the possible bonding seems to be intense only during the first minutes of processing. This is attributed to the rate that *G'* increases which is constantly dropping and is indicated by the concave curvature. This is in agreement with the *Tg* values reaching an equilibrium after the second reprocessing which corresponds to at least 10 min of processing not counting the time to cool down. Lastly, the values of the *Tg* have a significant influence on the MR effect. For a different TPU with a similar *Tg* but filled with the same concentration of CI particles, a 9 °C increase of the *Tg* corresponded to a ~ 70% decrease of the MR effect[34]. For the recycled samples, the bonding between the particles and the matrix suppresses the MR performance, thus only injection moulded matrices were studied. To conclude, the abovementioned bonding reduces the effects of degradation on the mechanical properties, and the MR effect is suppressed for the recycled matrices. However, in the real applications, only one third of the matrix will be recycled thus the MR performance of the injection moulded samples will not be changed dramatically.

The magnetic properties of the TPU matrices filled with CI particles were evaluated at room temperature using dynamic strain sweeps under various homogeneous magnetic fields through the MR effect which is defined in the following formula:

$$MR_{\text{effect}} = \frac{G'_{\text{on}} - G'_{\text{off}}}{G'_{\text{off}}} \tag{2}$$

where the on- and off-states are referred to as the presence and absence of the magnetic field, respectively. Generally, samples with particle concentrations below 50 wt% do not show any significant MR effect which was observed in the past for a very similar system[33]. On the other hand, the 80 wt% matrices are too immobile due to the bonds with the matrix and therefore an insignificant MR effect was observed. For that reason, a new matrix filled with 50 wt% was prepared and the MR performance was studied through dynamic strain sweeps. Figure 8a shows an increase in *G'* when the samples are exposed to external magnetic fields. The increase of *G'* is attributed to the magnetic particles attempting to align themselves and form chain-like structures parallel to the magnetic field. In addition, this trend is present mainly during the LVE where *G'* is independent of strain, which can be distinguished by the green solid line in Fig. 8a. Above the critical strain, the current structure collapses indicated by the sudden drop of the *G'*. The data in the LVE seems scattered especially at lower strains which is attributed to the high filling and stiffness of the matrix. Another difficulty is connected with the values of torque at lower strains which are only a few times higher than the resolution of the instrument. The latter is commonly encountered for highly filled matrices[49]. As a result of the slightly scattered data, the average of these points was considered for the evaluation of the MR effect. Unlike the responsive LVE, the magnetic field does not affect the modulus soon after the critical strain is reached. Thus, the MR effect for various fields was obtained only from

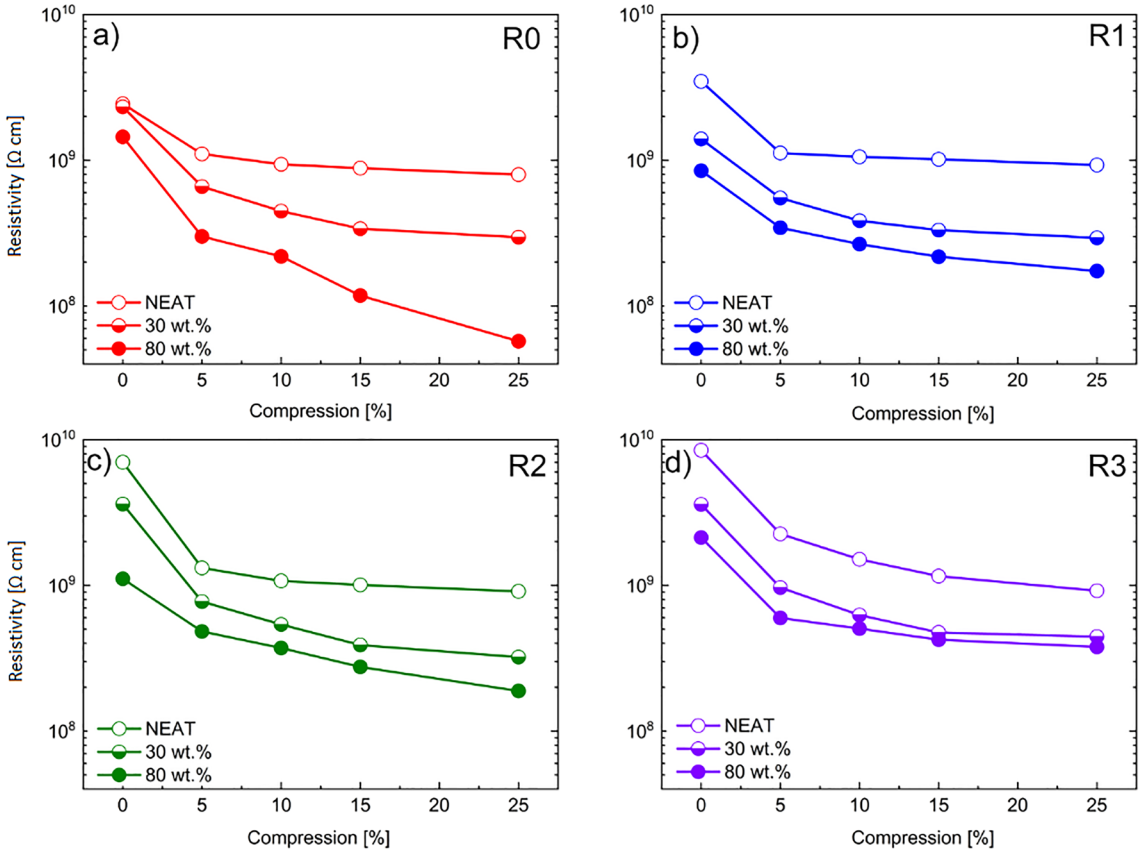

Figure 9. Resistivity dependences on the relative compression deformation of the neat TPUs (open symbols), 30 wt% filled TPUs (half up open symbols) and 80 wt% filled TPUs (solid symbols) for (**a**) IM/samples (red), (**b**) IM/one time recycling process (blue), (**c**) IM/two times recycling process (green), (**d**) IM/three times recycling process (purple).

the LVE. A linear incensement of the MR effect is demonstrated in Fig. 8b. These results can be compared with similar elastomers, thus these processed TPU are able to compete and surpass other TPU-based MREs on the MR effect point of view[33,34].

Lastly, it is very important to address the Payne effect as it could become a potential problem for future applications. Despite being observed in MREs and highly filled matrices as a sudden decrease in *G'*, similar to the one in Fig. 8a, this effect is completely ignored in most of the studies regarding MREs. For the MREs specifically, it experiences more effects such as a steady increment of *G'* with each consequential measurement making it worth investigating[28]. However, the focus of this study is to only evaluate the presence of the Payne effect. In Fig. 8a, the neat TPU matrix is also illustrated with a similar overall behaviour as the filled samples. The two main differences include the values of *G'* in the LVE which are higher for the filled particles and the extended LVE regime of the neat matrix. Both observations are common for highly filled matrices[50]. Since the pure matrix also shows a drop in the neighbourhood of the filled particles it is safe to conclude that any potential Payne effect could exist only in the limited strain regime around 0.02 and 0.2% where the LVE is terminated for the filled and neat matrices, respectively. However, as mentioned before, matrices with high filler concentrations have their LVE shorten[50]. As a result, the drop in *G'* is mainly caused by the collapse of the polymeric structure, rather than the collapse of the filler's network which should be more robust regardless due to the particle–matrix bonding of the matrix as mentioned above.

Piezoresistivity testing. In general, when a conductive composite is exposed to compression, its conductivity is increased (resistivity is decreased) as a result of the piezoresistive effect which is widely exploited[51]. As can be observed in Fig. 9, the dependence of the resistivity, used frequently as a quantity describing the performance of piezoresistive sensors, at various compression rates for both neat and filled matrices at different concentration and reprocessing cycles is presented. The resistivity is decreased at higher compression strains. For the neat TPU matrix, once a compression of 5% is achieved, a steep decrease of resistivity is apparent which is followed by a saturation as the samples underwent further deformation. Moreover, the matrices filled with the CI particles showed a notable increase in conductivity. The latter remark has been observed before in anisotropic MREs [13]. In the same study it was suggested that the decrease of resistivity was achieved with a different mechanism known as the variable-range hopping mechanism.

Overall, piezoresistivity increases with concentration and compression, nevertheless it slightly decreases with recycling. A possible cause could be the created bonds between iron and matrix during reprocessing. Finally,

the resistivity increases after each recycling process, however, the difference is not as significant resulting in an acceptable for an application.

Conclusion

We present a new type of MREs, which are able to be reprocessed several times while keeping their mechanical properties in the same level. Together with their pure analogues these MREs were studied in terms of mechanical properties, internal structure, magnetorheological performance and piezoresistivity. As in any other polymer filled with stiff particles, the material becomes stiffer and stronger however, more ductile. Reprocessing the samples results in a very minor drop (less than 10%) of mechanical properties. In addition, the magnetic performance of the sample can be compared with similar TPU based MREs, however after recycling the MR effect is severely reduced. The structural changes of the material during reprocessing is the key to answer the drops in the magnetomechanical performance. On one hand, a supressed degradation still resulted in a minor chain shortening which was detected via GPC and resulted in the drop of stiffness. On the other hand, for the first time, the bonding between the particles and the matrix was shown with a convincing analysis during which the reprocessing procedure was simulated. Moreover, these specific MREs did not suffer from the Payne effect unlike a typical highly filled matrix. Finally, piezoresistivity tests confirmed that after each reprocessing cycle, the conductivity slightly fell, however that change does not significantly affect the final product. In practice, the amount of the recycled matrix does not exceed one third of the final product. On the contrary, in this work, the samples containing 100% of recycled TPUs were examined with no significant decrease in observed properties. It can be concluded that MREs based on TPU are suitable for reuse with the exception of their magnetorheological properties which can be boosted regardless using established procedures such as adding plasticizers or an oil.

Data availability

The datasets generated and/or analysed during the current study are not publicly available due to their use as a part of an ongoing study but are available from the corresponding author on reasonable request.

Received: 19 April 2022; Accepted: 5 July 2022
Published online: 14 July 2022

References

1. Ahamed, R., Choi, S. B. & Ferdaus, M. M. A state of art on magneto-rheological materials and their potential applications. *J. Intell. Mater. Syst. Struct.* **29**(10), 2051–2095 (2018).
2. Saleh, T. A., Fadillah, G. & Ciptawati, E. Smart advanced responsive materials, synthesis methods and classifications: From lab to applications. *J. Polym. Res.* **28**, 6 (2021).
3. Carlson, J. D. & Jolly, M. R. MR fluid, foam and elastomer devices. *Mechatronics* **10**(4–5), 555–569 (2000).
4. Sun, S. *et al.* Development of magnetorheological elastomers-based tuned mass damper for building protection from seismic events. *J. Intell. Mater. Syst. Struct.* **29**(8), 1777–1789 (2018).
5. Komatsuzaki, T., Inoue, T. & Terashima, O. Broadband vibration control of a structure by using a magnetorheological elastomer-based tuned dynamic absorber. *Mechatronics* **40**, 128–136 (2016).
6. Cvek, M., Moucka, R., Sedlacik, M., Babayan, V. & Pavlinek, V. Enhancement of radio-absorbing properties and thermal conductivity of polysiloxane-based magnetorheological elastomers by the alignment of filler particles. *Smart Mater. Struct.* **26**, 9 (2017).
7. Cvek, M., Kutalkova, E., Moucka, R., Urbanek, P. & Sedlacik, M. Lightweight, transparent piezoresistive sensors conceptualized as anisotropic magnetorheological elastomers: A durability study. *Int. J. Mech. Sci.* **183**, 10 (2020).
8. Fiorillo, A. S., Critello, C. D. & Pullano, S. A. Theory, technology and applications of piezoresistive sensors: A review. *Sens. Actuators A.* **281**, 156–175 (2018).
9. Behrooz, M. & Gordaninejad, F. Three-dimensional study of a one-way, flexible magnetorheological elastomer-based micro fluid transport system. *Smart Mater. Struct.* **25**, 9 (2016).
10. Behrooz, M. & Gordaninejad, F. A flexible micro fluid transport system featuring magnetorheological elastomer. *Smart Mater. Struct.* **25**, 2 (2016).
11. Murao, S., Mitsufuji, K., Hirata, K. & Miyasaka, F. Coupled analysis by viscoelastic body with rigid body for design of MRE soft actuator. *Electr. Eng. Jpn.* **203**(3), 30–38 (2018).
12. Fu, Y. *et al.* A muscle-like magnetorheological actuator based on bidisperse magnetic particles enhanced flexible alginate-gelatin sponges. *Smart Mater. Struct.* **29**, 1 (2020).
13. Kelley, C. R. & Kauffman, J. L. Towards wearable tremor suppression using dielectric elastomer stack actuators. *Smart Mater. Struct.* **30**, 2 (2021).
14. Stoll, A., Mayer, M., Monkman, G. J. & Shamonin, M. Evaluation of highly compliant magneto-active elastomers with colossal magnetorheological response. *J. Appl. Polym. Sci.* **131**, 2 (2014).
15. Plachy, T. *et al.* Impact of corrosion process of carbonyl iron particles on magnetorheological behavior of their suspensions. *J. Ind. Eng. Chem.* **66**, 362–369 (2018).
16. Murin, I. V. *et al.* Structural-chemical transformations of alpha-Fe_2O_3 upon transport reduction. *Solid State Ionics* **133**(3–4), 203–210 (2000).
17. Cvek, M., Mrlik, M., Sevcik, J. & Sedlacik, M. Tailoring performance, damping, and surface properties of magnetorheological elastomers via particle-grafting technology. *Polymers* **10**, 12 (2018).
18. Perez, L. D., Zuluaga, M. A., Kyu, T., Mark, J. E. & Lopez, B. L. Preparation, characterization, and physical properties of multiwall carbon nanotube/elastomer composites. *Polym. Eng. Sci.* **49**(5), 866–874 (2009).
19. Boczkowska, A., Awietjan, S. F. & Wroblewski, R. Microstructure-property relationships of urethane magnetorheological elastomers. *Smart Mater. Struct.* **16**(5), 1924–1930 (2007).
20. Ju, B. X. *et al.* Dynamic mechanical properties of magnetorheological elastomers based on polyurethane matrix. *Polym. Compos.* **37**(5), 1587–1595 (2016).
21. Grigorescu, R. M. *et al.* Development of thermoplastic composites based on recycled polypropylene and waste printed circuit boards. *Waste Manage.* **118**, 391–401 (2020).
22. Datta, S., Naskar, K., Bhardwaj, Y. K. & Sabharwal, S. A study on dynamic rheological characterisation of electron beam crosslinked high vinyl styrene butadiene styrene block copolymer. *Polym. Bull.* **66**(5), 637–647 (2011).
23. Wolfel, B. *et al.* Recycling and reprocessing of thermoplastic polyurethane materials towards nonwoven processing. *Polymers* **12**(9), 13 (2020).

24. Vatandoost, H., Rakheja, S. & Sedaghati, R. Effects of iron particles' volume fraction on compression mode properties of magnetorheological elastomers. *J. Magn. Magn. Mater.* **522**, 14 (2021).
25. Winger, J., Schumann, M., Kupka, A. & Odenbach, S. Influence of the particle size on the magnetorheological effect of magnetorheological elastomers. *J. Magn. Magn. Mater.* **481**, 176–182 (2019).
26. Kwon, S. H., An, J. S., Choi, S. Y., Chung, K. H. & Choi, H. J. Poly(glycidyl methacrylate) coated soft-magnetic carbonyl iron/silicone rubber composite elastomer and its magnetorheology. *Macromol. Res.* **27**(5), 448–453 (2019).
27. Kwon, S. H., Lee, C. J., Choi, H. J., Chung, K. H. & Jung, J. H. Viscoelastic and mechanical behaviors of magneto-rheological carbonyl iron/natural rubber composites with magnetic iron oxide nanoparticle. *Smart Mater. Struct.* **28**, 4 (2019).
28. Sorokin, V. V. *et al.* Experimental study of the magnetic field enhanced Payne effect in magnetorheological elastomers. *Soft Matter* **10**(43), 8765–8776 (2014).
29. Fuensanta, M. & Martin-Martinez, J. M. Structural and viscoelastic properties of thermoplastic polyurethanes containing mixed soft segments with potential application as pressure sensitive adhesives. *Polymers* **13**, 18 (2021).
30. Albozahid, M., Naji, H. Z., Alobad, Z. K. & Saiani, A. TPU nanocomposites tailored by graphene nanoplatelets: The investigation of dispersion approaches and annealing treatment on thermal and mechanical properties. *Polym. Bull.* **1**, 1–10 (2021).
31. Luo, Y. *et al.* Fabrication of thermoplastic polyurethane with functionalized MXene towards high mechanical strength, flame-retardant, and smoke suppression properties. *J. Colloid Interface Sci.* **606**, 223–235 (2022).
32. Bozyel, I., Keser, Y. I. & Gokcen, D. Triple mode and multi-purpose flexible sensor fabrication based on carbon black and thermoplastic polyurethane composite with propolis. *Sens. Actuators A.* **332**, 17 (2021).
33. Wu, J. K., Gong, X. G., Chen, L., Xia, H. S. & Hu, Z. G. Preparation and characterization of isotropic polyurethane magnetorheological elastomer through in situ polymerization. *J. Appl. Polym. Sci.* **114**(2), 901–910 (2009).
34. Wei, B., Gong, X. L. & Jiang, W. Q. Influence of polyurethane properties on mechanical performances of magnetorheological elastomers. *J. Appl. Polym. Sci.* **116**(2), 771–778 (2010).
35. Cookson, J. W. Theory of the Piezo-resistive effect. *Phys. Rev.* **1**, 156–175 (2022).
36. Li, W. *et al.* Synergy of porous structure and microstructure in piezoresistive material for high-performance and flexible pressure sensors. *ACS Appl. Mater. Interfaces.* **13**(16), 19211–19220 (2021).
37. Georgopoulou, A., Michel, S., Vanderborght, B. & Clemens, F. Piezoresistive sensor fiber composites based on silicone elastomers for the monitoring of the position of a robot arm. *Sens. Actuators A.* **318**, 11 (2021).
38. Zhang, Y. H., Xia, Z. B., Huang, H. & Chen, H. Q. A degradation study of waterborne polyurethane based on TDI. *Polym. Testing* **28**(3), 264–269 (2009).
39. Hentschel, T. & Munstedt, H. Kinetics of the molar mass decrease in a polyurethane melt: A rheological study. *Polymer* **42**(7), 3195–3203 (2001).
40. Cvek, M., Kracalik, M., Sedlacik, M., Mrlik, M. & Sedlarik, V. Reprocessing of injection-molded magnetorheological elastomers based on TPE matrix. *Composites B* **172**, 253–261 (2019).
41. Lopez-Pamies, O. An exact result for the macroscopic response of particle-reinforced neo-Hookean solids. *J. Appl. Mech. Trans. ASME.* **77**, 2 (2010).
42. Schrodner, M. & Pflug, G. Magnetomechanical properties of composites and fibers made from thermoplastic elastomers (TPE) and carbonyl iron powder (CIP). *J. Magn. Magn. Mater.* **454**, 258–263 (2018).
43. Takahara, A., Coury, A. J., Hergenrother, R. W. & Cooper, S. L. Effect of soft segment chemistry on the biostability of segmented polyurethanes. I. In vitro oxidation. *J. Biomed. Mater. Res.* **25**(3), 341–356 (1991).
44. Grigoryeva, O. P. *et al.* The effect of multi-reprocessing on the structure and characteristics of thermoplastic elastomers based on recycled polymers. *Polym. Sci. A* **51**(2), 216–225 (2009).
45. Cvek, M. *et al.* Synthesis of silicone elastomers containing silyl-based polymer grafted carbonyl iron particles: An efficient way to improve magnetorheological, damping, and sensing performances. *Macromolecules* **50**(5), 2189–2200 (2017).
46. Rabindranath, R. & Bose, H., editors. On the mobility of iron particles embedded in elastomeric silicone matrix. *13th International Conference on Electrorheological Fluids and Magnetorheological Suspensions (ERMR)* (2012).
47. Sulkowski, W. W. *et al.* Thermogravimetric study of rubber waste-polyurethane composites. *J. Therm. Anal. Calorim.* **78**(3), 905–921 (2004).
48. Dwan'isa, J. P. L., Mohanty, A. K., Misra, M., Drzal, L. T. & Kazemizadeh, M. Novel soy oil based polyurethane composites: Fabrication and dynamic mechanical properties evaluation. *J. Mater. Sci.* **39**(5), 1887–1890 (2004).
49. Barnes, H. A. A review of the rheology of filled viscoelastic systems. *Rheol. Rev.* **1**, 1–36 (2003).
50. Rueda, M. M. *et al.* Rheology and applications of highly filled polymers: A review of current understanding. *Prog. Polym. Sci.* **66**, 22–53 (2017).
51. Chung, D. D. L. A critical review of piezoresistivity and its application in electrical-resistance-based strain sensing. *J. Mater. Sci.* **55**(32), 15367–15396 (2020).

Acknowledgements

The authors would like to thank L. Munteanu for her help with the WI measurements.

Author contributions

M.A.: Conceptualization; Investigation; Writing—Original Draft. R.A.: Investigation; Writing—Original Draft; Visualization; Funding acquisition. K.E.: Investigation; Writing—Original Draft. D.P.: Investigation; Writing—Original Draft. M.R.: Writing—Review & Editing. K.M.: Writing—Review & Editing. B.O.: Writing—Review & Editing. M.S.A.: Writing—Review & Editing. S.M.: Conceptualization; Writing—Original Draft; Writing—Review & Editing; Supervision; Funding acquisition.

Funding

The authors wish to thank the Internal Grant Agency of Tomas Bata University in Zlín (Project No. IGA/CPS/2021/003) for its financial support. The authors A.R., A.M., E.K., R.M. and M.S. gratefully acknowledge project DKRVO (RP/CPS/2022/007) supported by the Ministry of Education, Youth and Sports of the Czech Republic.

Competing interests

The authors declare no competing interests.

Additional information

Correspondence and requests for materials should be addressed to M.S.

Paper 4

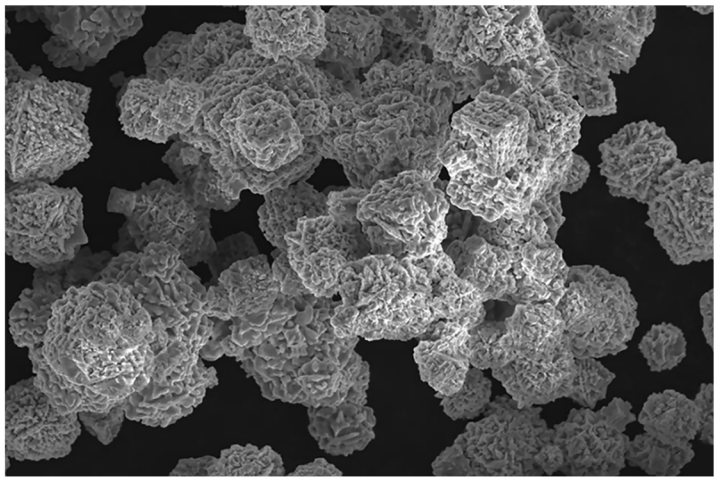

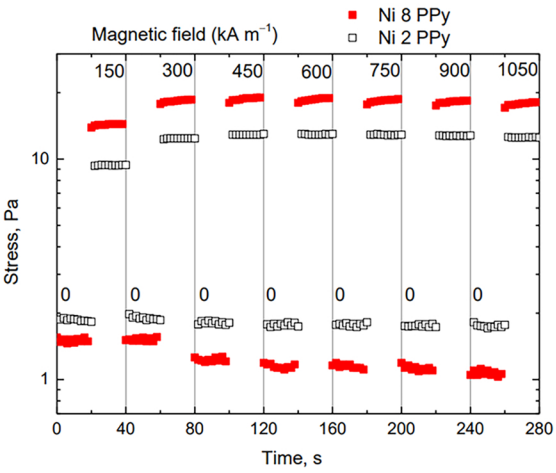

MDPI
Materials
Accepted 23rd December 2023

materials

MDPI

Article

Conducting and Magnetic Hybrid Polypyrrole/Nickel Composites and their Application in Magnetorheology

Marek Jurča [1], Jarmila Vilčáková [1], Natalia E. Kazantseva [1], Andrei Munteanu [1], Lenka Munteanu [1], Michal Sedlačík [1], Jaroslav Stejskal [1,2,*], Miroslava Trchová [2] and Jan Prokeš [3]

[1] University Institute, Tomas Bata University in Zlín, 760 01 Zlín, Czech Republic; jurca@utb.cz (M.J.); vilcakova@utb.cz (J.V.); kazantseva@utb.cz (N.E.K.); munteanu@utb.cz (A.M.); strouhalova@utb.cz (L.M.); msedlacik@utb.cz (M.S.)
[2] University of Chemistry and Technology, 166 28 Prague 6, Czech Republic; miroslava.trchova@vscht.cz
[3] Faculty of Mathematics and Physics, Charles University, 180 00 Prague 8, Czech Republic; jprokes@semi.mff.cuni.cz
* Correspondence: stejskal@utb.cz

Abstract: Hybrid organic/inorganic conducting and magnetic composites of core–shell type have been prepared by in-situ coating of nickel microparticles with polypyrrole. Three series of syntheses have been made. In the first, pyrrole was oxidised with ammonium peroxydisulfate in water in the presence of various amounts of nickel and the composites contained up to 83 wt% of this metal. The second series used 0.1 M sulfuric acid as a reaction medium. Finally, the composites with polypyrrole nanotubes were prepared in water in the presence of structure-guiding methyl orange dye. The nanotubes have always been accompanied by the globular morphology. FTIR and Raman spectroscopies confirmed the formation of polypyrrole. The resistivity of composite powders of the order of tens to hundreds Ω cm was monitored as a function of pressure up to 10 MPa. The resistivity of composites slightly increased with increasing content of nickel. This apparent paradox is explained by the coating of nickel particles with polypyrrole, which prevents their contact and subsequent generation of metallic conducting pathways. Electrical properties were practically independent of the way of composite preparation or nickel content and were controlled by the polypyrrole phase. On the contrary, magnetic properties were determined exclusively by nickel content. The composites were used as a solid phase to prepare a magnetorheological fluid. The test showed better performance when compared with a different nickel system reported earlier.

Keywords: nickel microparticles; polypyrrole; hybrid composites; resistivity; conductivity; magnetization; magnetorheology

Citation: Jurča, M.; Vilčáková, J.; Kazantseva, N.E.; Munteanu, A.; Munteanu, L.; Sedlačík, M.; Stejskal, J.; Trchová, M.; Prokeš, J. Conducting and Magnetic Hybrid Polypyrrole/Nickel Composites and their Application in Magnetorheology. *Materials* **2024**, *17*, 151. https://doi.org/10.3390/ma17010151

Academic Editors: Vlassios Likodimos and Giuseppe Mele

Received: 23 November 2023
Revised: 13 December 2023
Accepted: 23 December 2023
Published: 27 December 2023

1. Introduction

Hybrid organic/inorganic composites constitute the core of many functional materials. This applies especially to the cases when both matrix/filler components have a functional character, i.e., they display complementary chemical or physical properties alone or in accord. The combination of metals with conducting polymers in composites is one of the possibilities frequently discussed in the literature in the design of energy conversion and storage devices and in a variety of other applications. Even though the composites applied in practice often include additional inorganic components, typically mixed metal oxides and sulfides or carbons [1,2], the understanding of binary systems is essential. One of the open research tasks includes the preparation of polypyrrole/nickel composites.

Nickel is a key element used in electrodes for its conductivity and electrocatalytic activity, suitable morphology and material properties. Furthermore, its magnetic properties make the element even more attractive. Conducting polymers, such as polypyrrole,

have often been used as additives that improve conductivity and electrochemical activity and facilitate electron–ion transfers [2]. The system, which is composed of metallic nickel and a conducting polymer, polypyrrole, is discussed below.

Nickel metal may be present in two forms: nickel foam and microparticles, the former being dominant. Nickel foam has been used as a support for the deposition of polypyrrole by the in-situ chemical oxidation of pyrrole with ammonium peroxydisulfate [3–6]. An original approach was represented by the chemical oxidation using silver nitrate at nickel foam that catalysed the pyrrole polymerisation and introduced metallic silver at the same time [7]. The polypyrrole coating was obtained in an acidic solution even without an added oxidant [8]. In another case, the separately prepared polypyrrole suspension was simply deposited in nickel foam [9]. As an alternative, the nickel foam has been coated with polypyrrole potentiostatically [10,11], at a constant current density [12] or by using cyclic voltammetry [13,14]. Systems based on nickel foam are applicable, especially as current collectors in supercapacitors where the nickel provides the conductivity as well as the mechanical support for the deposition of polypyrrole [4–9,15–17]. Other diverse applications are represented by electrodes for electrocatalytic oxidation of methanol [11], improved water-splitting [14,17], solar steam-generation [3,10], solar-thermal desalination [18], or allowed for controlled electrosorption of organic pollutant dye [12].

There are two types of composites based on polypyrrole and nickel microparticles. The first is represented by the deposition of nickel on conducting polymer. Polypyrrole was electrochemically prepared on a graphite electrode, followed by the electrochemical electrodeposition of nickel microparticles [19–21]. This type of polypyrrole/nickel particulate composite has been used as an electrocatalyst of hydrogen-evolution reaction [17,19] or ethanol oxidation [20], and in the design of glucose biosensors [21] or in insulin sensors [22]. The reverse strategy relies on the coating of nickel particles with polypyrrole. Polypyrrole was electrodeposited on nickel particles at silicon nanowire arrays [16]. The chemical oxidation of pyrrole with sodium peroxydisulfate in the presence of nickel flakes is another example [23].

The defined preparation of polypyrrole-coated nickel microparticles is still a challenge. Virtually any interface immersed in the aqueous reaction mixture used for the preparation of conducting polymers by the chemical oxidation of respective monomers becomes coated with a thin submicrometre polymer film. This applies both to polyaniline and polypyrrole. The oligomers produced in the early stages of oxidation are hydrophobic, and they adsorb at available surfaces. The growth of polymer chains follows, resulting in the brush-like coating of substrates with conducting polymers. Such an approach has also been used for the coating of inorganic particles, e.g., ferrites [24]. When applied to particles of non-noble metals, such as nickel, some problems have been met. The oxidation of pyrrole to polypyrrole proceeds invariably under acidic conditions. The combination of an acidic medium and the presence of an oxidant is expected to cause the corrosion of non-noble metals followed by their dissolution, instead of being coated with a conducting polymer. For this reason, studies in this direction have been rare [23,25]. For example, when aniline hydrochloride was oxidised with ammonium peroxydisulfate in the presence of nickel microparticles, polyaniline/nickel was produced at reduced yield and conductivity of the order 10^{-2}–10^{-3} S cm^{-1}, i.e., values below the conductivity of components [25]. This phenomenon was explained by the nickel dissolution assisted by sulfuric acid generated during polymerisation. It was accompanied by the evolution of hydrogen gas catalysed by nickel and followed by a simultaneous reduction of the emeraldine form of polyaniline to leucoemeraldine. The present study reports similar trends in the preparation of polypyrrole/nickel composites but offers an alternative explanation of their properties.

Polypyrrole/nickel composites, where nickel core is coated with polypyrrole shell, may find use in various electrodes, suspensions in magnetorheology, magnetically separable adsorbents, electrocatalysts, fillers in functional flexible composites, and electro-

magnetic interference shielding, thus exploiting also magnetic and catalytic properties of nickel [26]. The preparation of such composites and their electrical characterisation is the goal of the present study, which introduces a novel way to include the deposition of polypyrrole nanotubes.

2. Experimental

2.1. Preparation

Nickel microparticles with a hedgehog-like morphology were employed as a conducting and magnetic filler to prepare polypyrrole-coated nickel microparticles (Table 1). Nickel particles (99.8%; Goodfellow, London, UK) exhibited a normal size distribution with a mean diameter of 5.5 ± 1.8 μm. Various amounts of nickel were dispersed in an aqueous solution of pyrrole, and then the solution of ammonium peroxydisulfate, also in water, was added under stirring to initiate the in-situ polymerisation of pyrrole. The concentrations of reactants were 0.1 M pyrrole (1.34 g, 20 mmol per 200 mL) and 0.125 M ammonium peroxydisulfate (5.71 g, 25 mmol per 200 mL). The polymerisation was left to proceed for 30 min at room temperature. In the second series, water was replaced with 0.1 M sulfuric acid (Table 1). The resulting composite microparticles of globular polypyrrole deposited on nickel were separated by filtration, rinsed several times with distilled water or 0.1 M sulfuric acid, followed by ethanol, to remove any unreacted reagents or by-products. The solids were left to dry at ambient temperature in open air for 48 h. The preparation of similar composites, including polypyrrole nanotubes and nickel, followed the same protocol in water that contained, in addition, 0.004 M methyl orange (262 mg, 0.8 mmol per 200 mL). All chemicals were supplied by the Sigma-Aldrich branch (Prague, Czech Republic) and used as delivered.

Table 1. The protocol for the oxidation of 0.1 M pyrrole with 0.125 M ammonium peroxydisulfate to polypyrrole in the presence of nickel microparticles at 20 °C.

Series	Medium	Additive	Morphology
1	water	–	globules
2	0.1 M H_2SO_4	–	globules
3	water	0.004 M MO	nanotubes/globules

2.2. Composition

The composition of prepared materials involved the combustion of the organic component in an oxygen atmosphere at 800 °C in a muffle furnace (Nabertherm L9/S27, Lilienthal, Germany). The residual mass represented by nickel(II) oxide was recalculated to nickel metal. Additionally, a subset of randomly selected samples was subjected to thermogravimetric analysis (TA Q500; TA Instruments, Eden Prairie, MN, USA) with a heating rate of 10 °C min^{-1} in an oxygen atmosphere. The results were consistent with those obtained by the bulk combustion method.

2.3. Morphology

A scanning electron microscope (Nova NanoSEM FEI, Brno, Czech Republic) was used to assess the morphology of polypyrrole and its composites with nickel. Prior to analysis, the samples were gold sputter-coated using a JEOL JFC 1300 Auto Fine Coater (JEOL, Tokyo, Japan).

2.4. Spectroscopy

ATR FTIR spectra were analysed with a Nicolet 6700 spectrometer (Thermo-Nicolet, Waltham, MA, USA) equipped with a reflective ATR extension GladiATR (PIKE Technologies, Fitchburg, WI, USA) and a diamond crystal. Spectra were recorded in the range of 4000–400 cm^{-1} with a resolution of 4 cm^{-1}, 64 scans, and Happ–Genzel appodization.

The OMNIC 8 package was used for both the spectrometer control and spectral data processing.

Dispersive Raman spectra were recorded in a back-scattering geometry using a Scientific DXR Raman microscope (Thermo Fisher Scientific, Waltham, MA, USA) using a 780 nm excitation laser line. The scattered light was analysed by a spectrograph with holographic grating 1200 lines mm^{-1} and a 50 μm pinhole width. The acquisition time was 10 s with 10 repetitions.

2.5. Resistivity

A four-point van der Pauw method using a lab-made press based on a cylindrical glass cell with an inner diameter of 10 mm was used to assess electrical properties [27]. The powdered composites were placed between a support and a glass piston with four wire electrodes fixed at its perimeter. The experimental setup included a current source, a Keithley 220, a Keithley 2010 multimeter and a Keithley 705 scanner with a Keithley 7052 matrix card (Keithley Instruments Inc., Cleveland, OH, USA). The pressure up to 10 MPa (=102 kp cm^{-2}) was registered with a L6E3 strain gauge cell (Zemic Europe BV, Etten-Leur, The Netherlands). The pressure was applied with an E87H4-B05 stepper motor (Haydon Switch & Instrument Inc., Waterbury, CT, USA). The sample thickness was recorded during the compression with a dial indicator Mitutoyo ID-S112X (Mitutoyo Corp., Sakado, Japan). The resistivity was also separately determined on composite pellets prepared after compression at 527 MPa by a manual hydraulic press (Specac, Orpington, UK).

2.6. Magnetic Properties

The magnetic characteristics were determined by measurement of a magnetic hysteresis curve in the range ±10 kOe by a vibrating sample magnetometer (VSM, Model 7407, Westerville, OH, USA).

2.7. Magnetorheology

The fluids were prepared by mixing the polypyrrole/nickel composites with mineral oil (Sigma-Aldrich, Czech Republic; viscosity 19.6 mPa s at 25 °C) at 9 wt% composite content. After preparation and before each measurement, the suspensions were sonicated in an ultrasonic bath for 10 min to remove any agglomerates. For the rheological measurements, the rotational rheometer Physica MCR 502 (Anton Paar, Graz, Austria) was used. To determine the flow properties of the samples under an external magnetic field, the device was equipped with an MRD 170/1T magneto cell and H-PTD hood. Magnetic fields varied from 0 to 1050 kA m^{-1}. For the tests, a 20 mm plate–plate geometry with a sandblasted surface was used to reduce the potential wall slip. The measurements were performed at a 300 μm gap and 25 °C, which was controlled using an external bath. Two types of flow tests were performed. At first, the flow curves were obtained for various magnetic fields. The shear rate window used was determined to be between 0.01 and 150 s^{-1} to avoid overflow. The second type of measurement included a stepwise increase of the magnetic field under steady shear. The magnetic field was turned on and off periodically every 20 s while the magnetic field linearly increased by 150 kA m^{-1} with the shear rate kept constant at 50 s^{-1}. Before each measurement, the samples were redispersed under the shear rate of 50 s^{-1} for 1 min, and after each test, the magnetic field was set to 150 kA m^{-1} to avoid potential sedimentation. Each measurement was repeated at least twice.

3. Results and Discussion

3.1. Preparation

It should be noted that polymer chemists prefer the use of iron(III) chloride as an oxidant of pyrrole due to the superior conductivity of polypyrrole, especially in the preparation of polypyrrole nanotubes. When pyrrole was oxidised with iron(III) chloride

in the presence of nickel microparticles, however, nickel dissolved and no composite was obtained. In an attempt to reduce the acidity of the reaction medium, the oxidant was replaced by ammonium peroxydisulfate. There was a single report in the literature when polypyrrole coating of nickel flakes was achieved by admicellar polymerisation of pyrrole, i.e., by the oxidation of pyrrole with sodium peroxydisulfate in the presence of anionic surfactant micelles [23]. The conductivity of coated nickel has not changed, and nickel has not dissolved either. When used in a polyethylene matrix, improved particle contacts afforded by polypyrrole coating were found. Following this approach, pyrrole was oxidised with ammonium peroxydisulfate in aqueous medium along with various portions of nickel microparticles and conducting polypyrrole/nickel composites have been obtained in stoichiometric yield (Figure 1). In contrast to the case of polyaniline [25], no hydrogen evolution associated with a partial metal dissolution of nickel has been observed.

The oxidation of pyrrole produces polypyrrole salt (Figure 1). The constitutional repeating unit is represented by four pyrroles with two protonated nitrogen atoms. The redistribution of electrons yields cation radicals (polarons) within the chain structure. They act as charge carriers that are responsible for the electrical conduction. When ammonium peroxydisulfate is an oxidant, sulfuric acid and ammonium sulfate are by-products. A part of sulfuric acid participates in the protonation of polypyrrole and provides sulfate counter-ions.

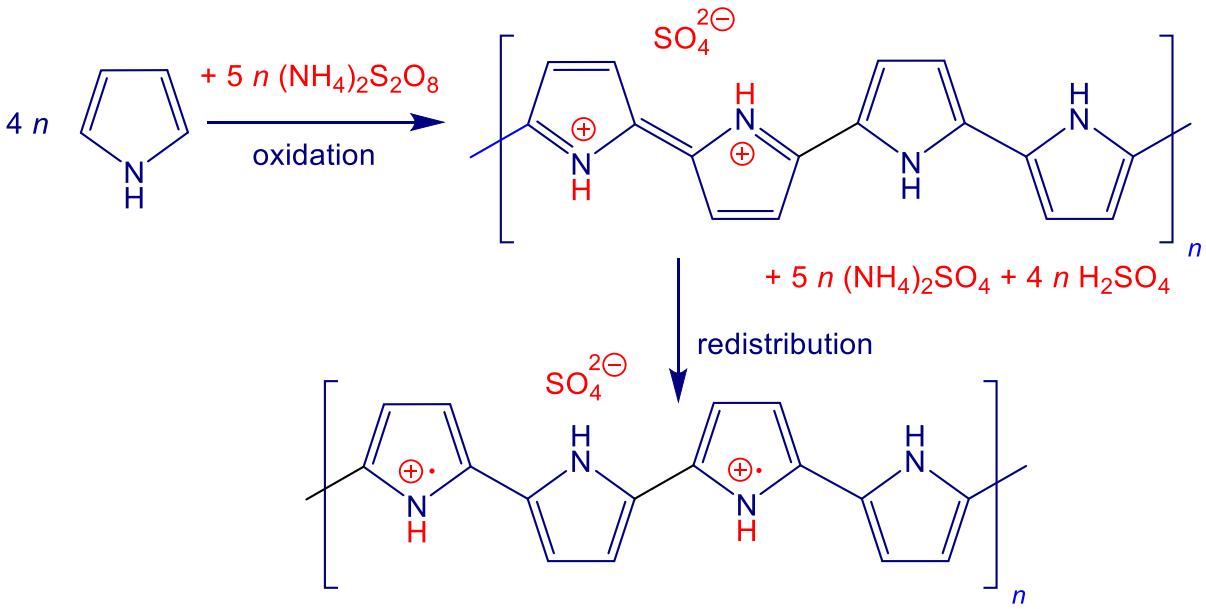

Figure 1. The oxidation of pyrrole with ammonium peroxydisulfate yields polypyrrole (sulfate salt). The electron redistribution generates the polaronic structure. Ammonium sulfate and sulfuric acid are by-products.

In the present synthesis, 20 mmol (1.34 g) of pyrrole was oxidised with 25 mmol (5.71 g) of ammonium peroxydisulfate in 200 mL of aqueous medium. The idealised stoichiometry (Figure 1) thus expects the 1.78 g yield of polypyrrole sulfate. Various amounts of nickel, 0.5–8 g, were introduced prior to the oxidant addition. The composite yields were close to each other in all three series (Table 1) carried out (1) in water, (2) in 0.1 M sulfuric acid, and (3) in water in the presence of methyl orange (MO). The compositions were practically independent of the reaction medium and well corresponded to the stoichiometric expectation (Table 2). Both components of the composite differ in density, 1.5 g cm^{-3} for polypyrrole [28] and 8.91 g cm^{-3} for nickel at 20 °C. One should keep in mind that electrical properties are controlled by volume fractions of components, and volume fractions of nickel are considerably lower than those based on weight (Table 2).

Table 2. Composite composition expected from the reaction stoichiometry (Figure 1) in dependence on nickel mass entering 200 mL of the reaction mixture and the nickel content found in the composites prepared in water or 0.1 M sulfuric acid (globular polypyrroles), and in water in the presence of methyl orange (polypyrrole nanotubes/globules).

Nickel,	Expected Nickel Content		Nickel Content Found, wt%		
g/200 mL	wt% Ni	vol% Ni	Water	0.1 M H_2SO_4	Water + MO
0.5	21.9	4.5	18.3	–	22.9
1	36.0	8.7	35.0	–	33.6
2	52.9	15.9	56.4	52.8	53.1
4	69.2	27.4	70.9	70.2	70.7
6	77.1	36.2	78.5	77.7	78.3
8	81.2	42.1	83.2	84.7	83.4

3.2. Morphology

Nickel microparticles have a typical hedgehog morphology (Figure 2a) with the size of several micrometres and medium polydispersity. Polypyrrole was prepared in water without and with methyl orange, respectively. The former reveals the typical globular morphology with a particle size of 50–200 nm (Figure 2b); the latter resulted in the formation of polypyrrole nanotubes accompanied by a significant fraction of globular morphology (Figure 2c). It has to be stressed that uniform and highly conducting polypyrrole nanotubes are prepared with iron(III) chloride oxidant, and its replacement with ammonium peroxydisulfate in a present study led to definitely inferior morphology with only a limited occurrence of nanotubes.

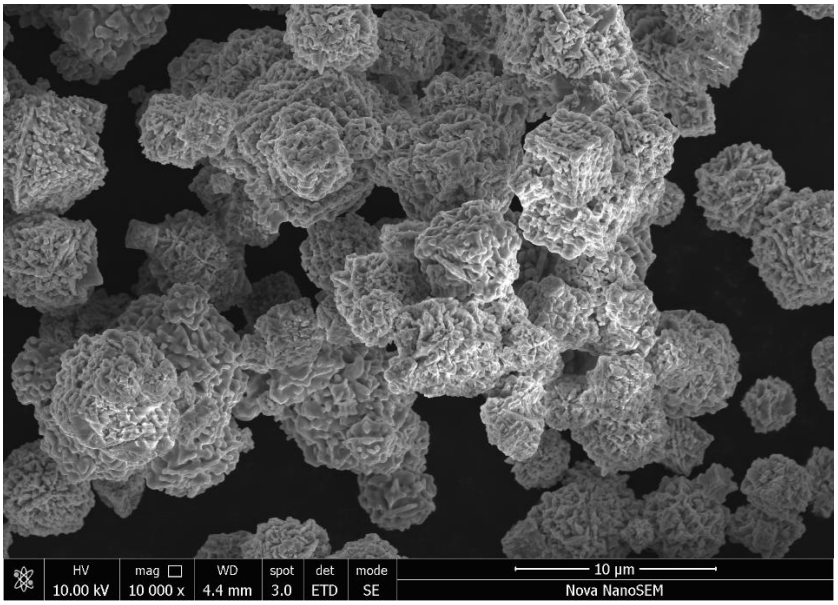

(**a**) Nickel microparticles

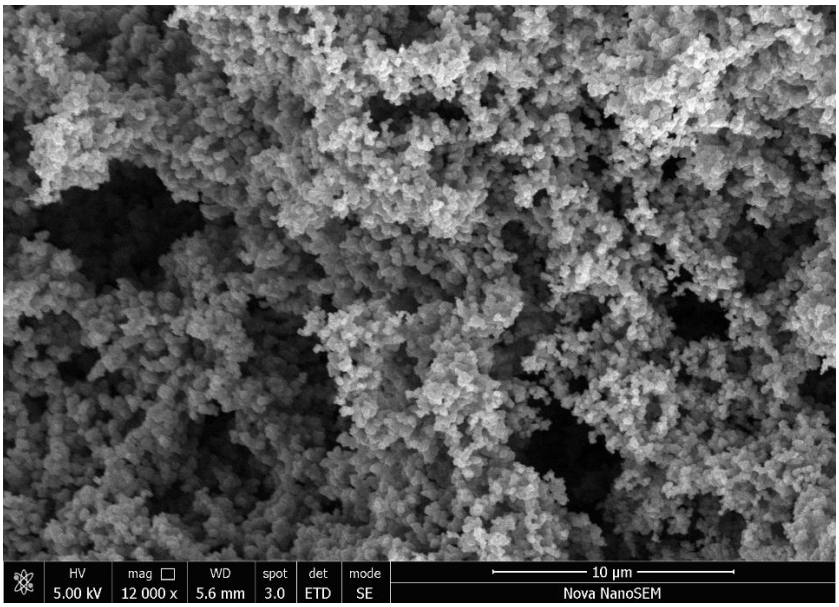

(**b**) Globular polypyrrole

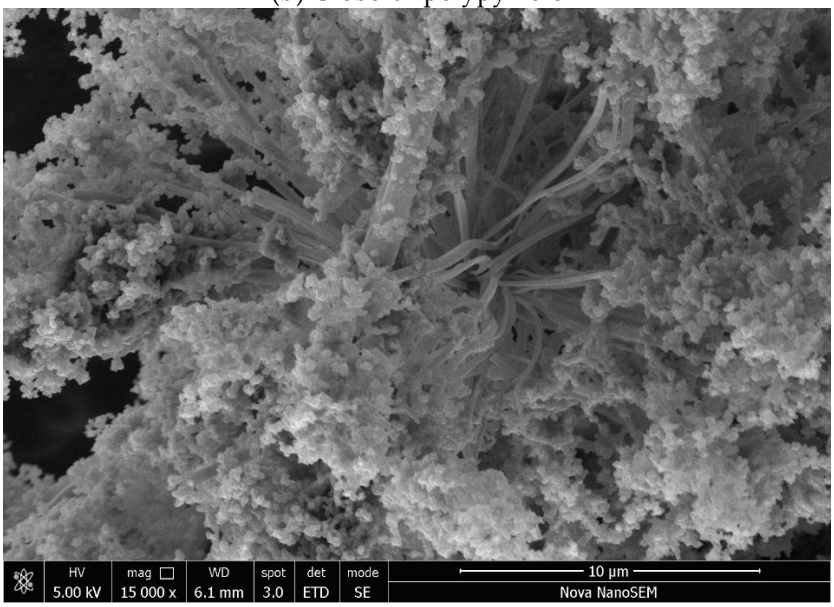

(**c**) Polypyrrole nanotubes/globules

Figure 2. Scanning electron micrographs of composite components: (**a**) nickel and (**b**) globular polypyrrole, and (**c**) polypyrrole nanotubes/globules.

The images of polypyrrole/nickel composites show only the presence of polypyrrole in globular form (Figure 3a) or its mixture with polypyrrole nanotubes with a diameter of about 100–500 nm and a length of 5–10 µm (Figure 3b). No nickel microparticles have been observed. During the polypyrrole synthesis, this polymer grows at the nickel surface, resulting in a complete coating of metal microparticles. As a result, nickel particles are dispersed in the polypyrrole matrix, and they stay apart from each other within the polymer phase. Such composite structure determines the electrical properties discussed below.

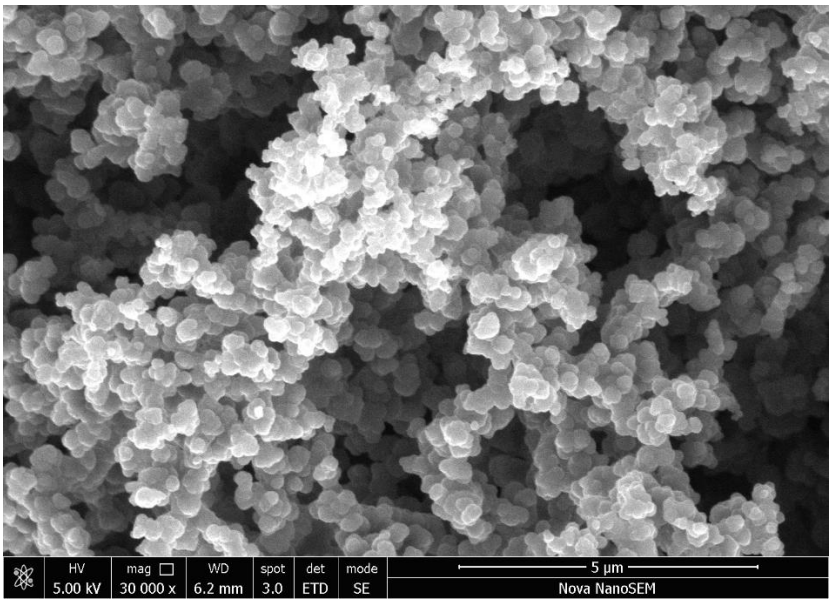

(**a**) Globular polypyrrole/nickel

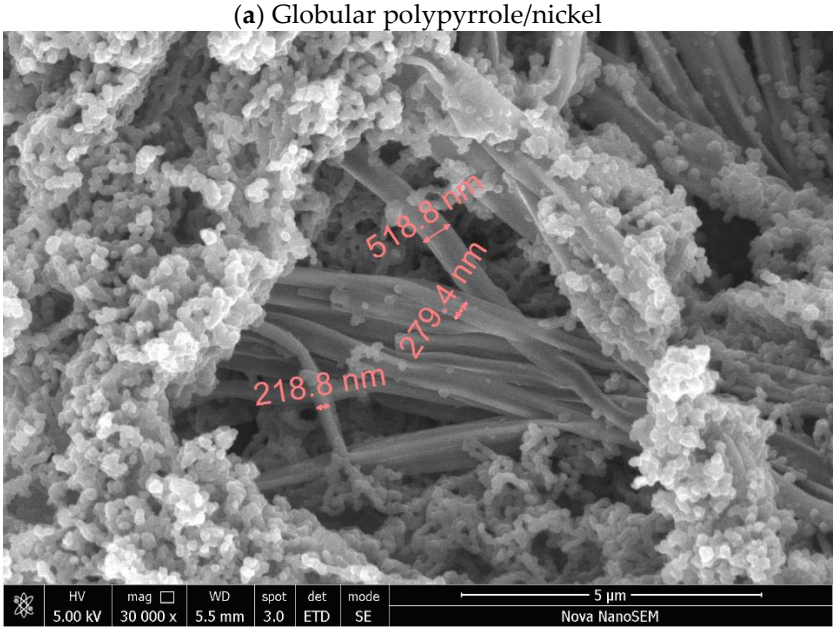

(**b**) Polypyrrole nanotubes/nickel

Figure 3. Scanning electron micrographs of composites composed of nickel (ca 50 wt%) and (**a**) polypyrrole globules or (**b**) polypyrrole nanotubes/globules.

3.3. Spectroscopy

ATR FTIR spectrum of powdered polypyrrole prepared in the absence of nickel (PPy in Figure 4) corresponds to the protonated form of polypyrrole (Figure 1), which exhibits, in addition to a broad absorption band at wavenumbers above 2000 cm^{-1} (Figure 4), the main bands with local maxima situated at 1542 cm^{-1} (C–C stretching vibrations in the pyrrole ring), 1467 cm^{-1} (C–N stretching vibrations in the ring), 1290 cm^{-1} (C–H and C–N in-plane deformation modes), 1164 cm^{-1} (breathing vibrations of the pyrrole ring), 1094 cm^{-1} (breathing vibrations of pyrrole ring), 1036 cm^{-1} (C–H and C–N in-plane deformation vibrations), 991 cm^{-1} (C–H out-of-plane deformation vibrations of the ring), and at 897 cm^{-1} (C–C out-of-plane deformation vibrations of the ring). The maximum of the broadband detected at 1686 cm^{-1} was assigned to the presence of the carbonyl group previously attributed to the nucleophilic attack of water on the pyrrole ring during the preparation. The shape of polypyrrole spectra did not change with increasing amounts of nickel in the reaction mixture, i.e., nickel did not interfere with the formation of

polypyrrole. A small shift of the maxima of the main bands to higher wavenumbers may indicate a slight deprotonation of the polypyrrole with an increasing amount of nickel. There is no observable difference between polypyrrole prepared in water and 0.1 M sulfuric acid (Figure 4). This is not surprising because sulfuric acid is generated as a by-product during the synthesis (Figure 1).

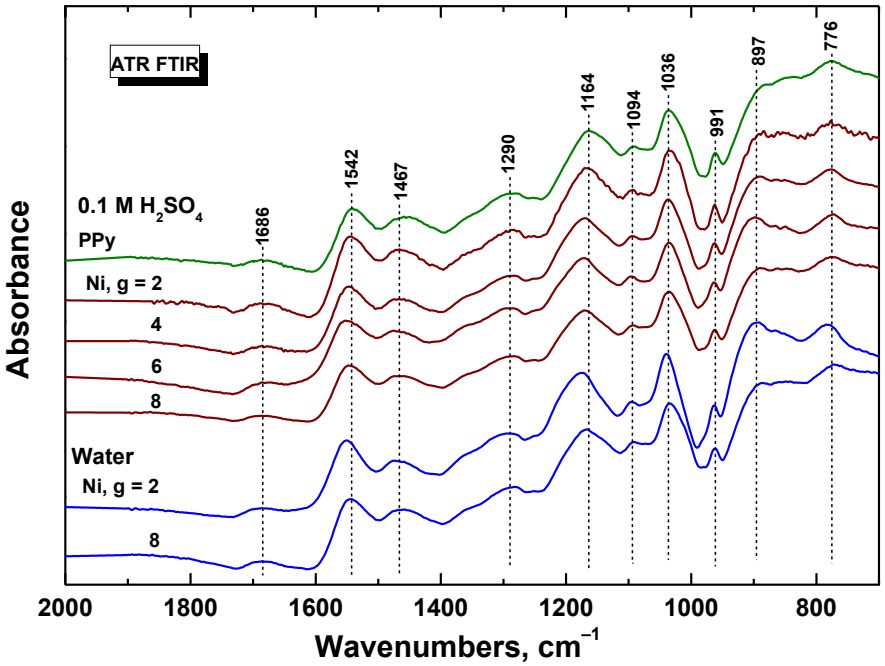

Figure 4. ATR FTIR spectra of polypyrrole and polypyrrole/nickel composites (2–8 g nickel) prepared in 0.1 M sulfuric acid or in water.

Raman spectroscopy is the surface-dedicated method. In Raman spectra of polypyrrole prepared in the absence of nickel (PPy in Figure 5), we detect the bands of polypyrrole with local maxima at 1590 cm^{-1} (C=C stretching vibrations of polypyrrole backbone) and 1479 cm^{-1} (C–C and C=N stretching skeletal vibrations), two bands of ring-stretching vibrations at 1382 and 1315 cm^{-1}, a band at 1245 cm^{-1} (antisymmetric C–H deformation vibrations), and a double-peak with local maxima at 1085 and 1045 cm^{-1} (C–H out-of-plane deformation vibrations, the second became sharper during deprotonation [29]). This is in agreement with the infrared spectra that suggest a slight deprotonation of the samples with an increasing amount of nickel.

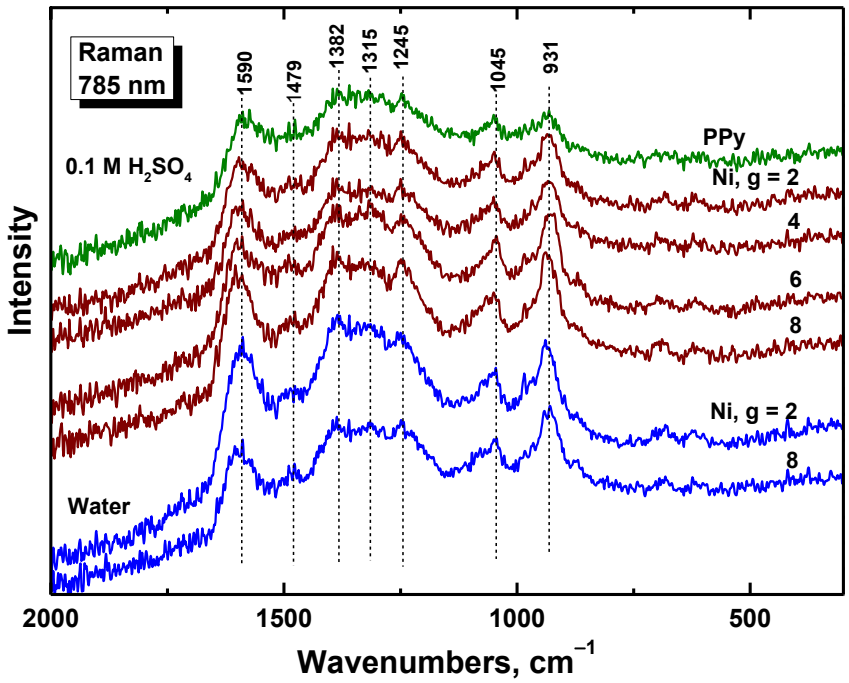

Figure 5. Raman spectra of polypyrrole (PPy) and polypyrrole/nickel composites (Ni, g = 2–8) prepared in water and in 0.1 M sulfuric acid.

3.4. Resistivity

The resistivity of various conducting powders is usually determined by the four-point method on compressed pellets. Free-standing pellets cannot be prepared for many materials, e.g., carbon black or carbon nanotubes, nickel or ferrite microparticles, and the characterisation has to be performed with powders under applied pressure. This is not the case of present composites, but the measurement of pressure dependences of resistivity provides additional information about the electrical properties of powders.

Double-logarithmic dependences of resistivity on pressure are linear in the investigated range of 0.1–10 MPa for composites of both types of polypyrrole with nickel (Figure 6a,b). The resistivity of neat nickel particles recorded in the same manner is two orders of magnitude lower (Figure 6c). When compressed at 10 MPa, it was 1.43×10^{-3} Ω cm, which corresponds to 700 S cm^{-1} conductivity, in accordance with the earlier data [25]. The results then constitute an apparent paradox illustrating that the introduction of highly conducting nickel results in the *increase* of resistivity, and this becomes even more pronounced as the nickel content grows.

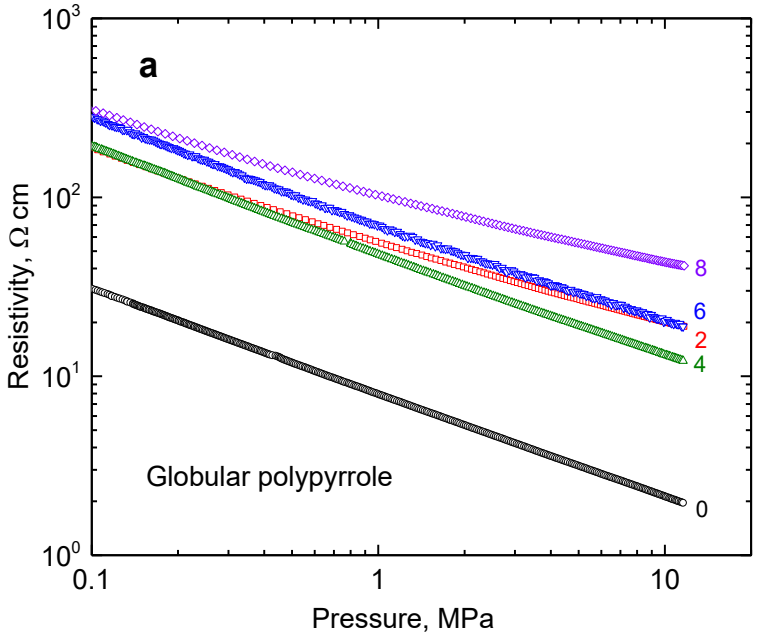
a
Resistivity, Ω cm
Pressure, MPa
Globular polypyrrole
8
6
2
4
0

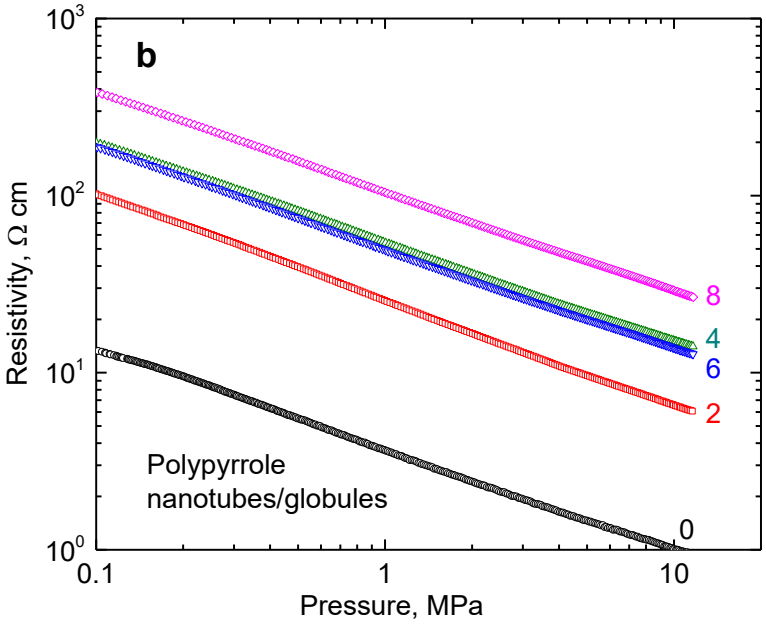
b
Resistivity, Ω cm
Pressure, MPa
Polypyrrole
nanotubes/globules
8
4
6
2
0

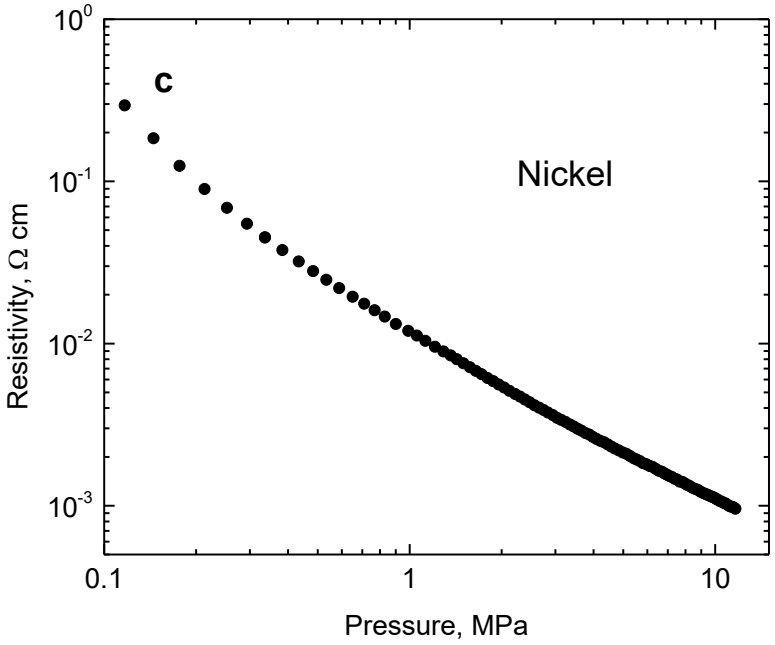

Figure 6. The pressure dependence of resistivity for (**a**) globular polypyrrole (0) and its polypyrrole/nickel composites (2–8 g nickel) and (**b**) for analogous polypyrrole nanotubes/globules composites with nickel. (**c**) The similar dependence for neat nickel microparticles.

The explanation follows: Let us consider the classical case when the conducting metal particles are gradually introduced into a non-conducting polymer matrix. When their fraction is low, they are randomly distributed without any mutual contacts. In such a composite, no conducting pathways are present, and the composite would remain non-conducting despite the presence of dispersed conducting objects. When the content of metal particles becomes higher, their contacts start to occur, and finally, they generate the first conducting pathway at the so-called percolation threshold. The conductivity then starts to grow rapidly with increasing metal content.

The microstructure of the system under study, however, is different. Instead of neat metal particles distributed in the polymer matrix, the composite is constituted by metal particles *coated* with polypyrrole. This coating and any accompanying polypyrrole form the conducing matrix. This means that the coating prevents contact between metal particles; they will always be separated regardless of their fraction, and they cannot, therefore, create any conducting pathways and thus contribute to the overall composite conductivity. The conductivity of the composite is then determined by the conductivity of the polypyrrole matrix.

In addition, as the content of metal particles in the composite increases, the volume fraction of the matrix decreases accordingly, and consequently, the resistivity of the composite increases (Figure 6a,b). Such results produce an apparent paradox when the increasing fraction of conducting metal particles (but coated with polymer!) leads to an increase in the composite resistivity. A similar behaviour was observed earlier with nickel microparticles coated with polyaniline [25].

In the present case, the standard compact pellets could also be prepared by compression at 527 MPa. The resistivity determined with them is several times lower than that found at 10 MPa pressure (Figure 7a). The resistivity of true polypyrrole nanotubes is lower compared with globular polypyrrole, but in the present study, the nanotubular morphology has not been fully developed. As far as the composites are concerned, the conductivity is, therefore, about the same within one order of magnitude regardless of the way of preparation and polypyrrole morphology.

Some readers may prefer plotting the conductivity against the volume fraction of nickel (Table 2, Figure 7b). The apparent paradox demonstrated then by the decrease in composite conductivity with increasing content of highly conducting nickel microparticles is obvious.

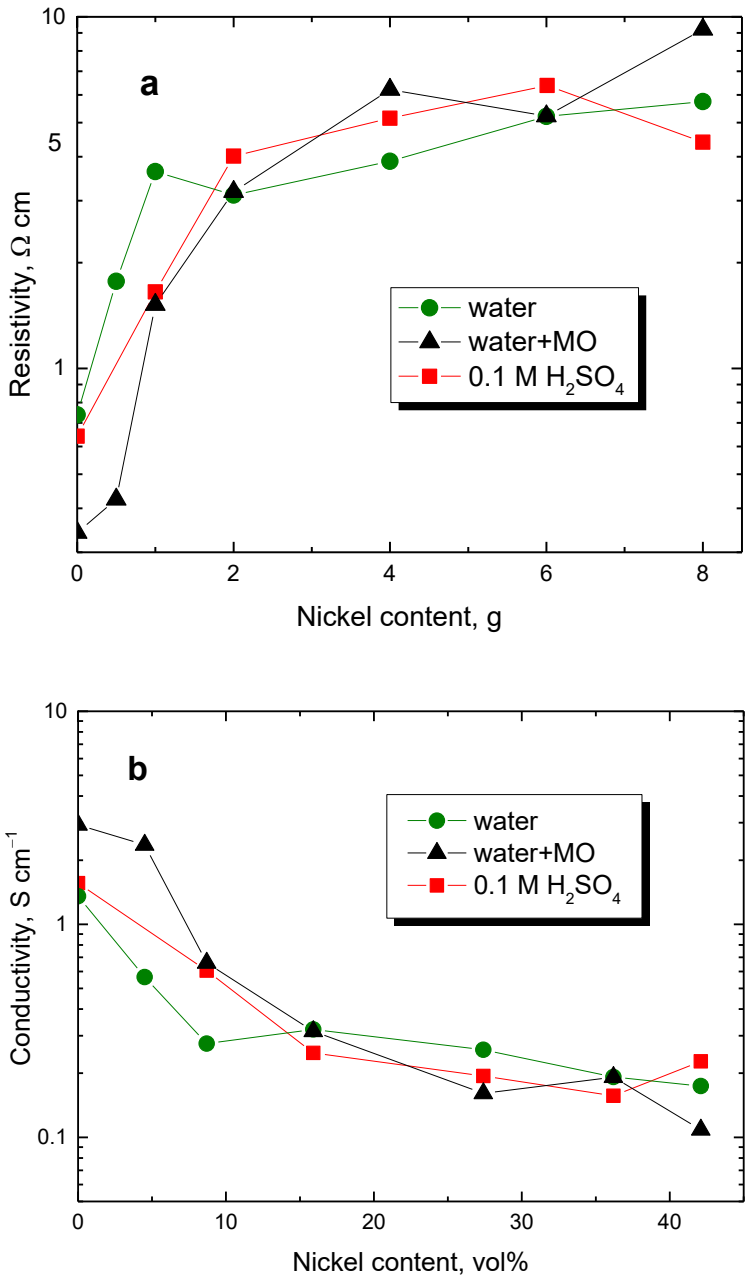

Figure 7. (**a**) Resistivity of polypyrrole/nickel composites determined in pellets in dependence on nickel content (in g) and (**b**) its reciprocal value, conductivity, on nickel content (in vol%). Preparation of globular polypyrrole in water (circles), nanotubes/globules in the presence of methyl orange (triangles), or globules in an acidic medium (squares).

3.5. Mechanical Properties

The experimental setup used for the determination of resistivity also allows for the monitoring of sample thickness during compression (Figure 8). The pressure dependence of composites is close to linear in double-logarithmic presentation. The slope provides information about the fluffiness, i.e., the steeper it is, the easier the material is compressed. The decrease in the slope with increasing nickel content reflects the composite reinforcement with metallic microparticles.

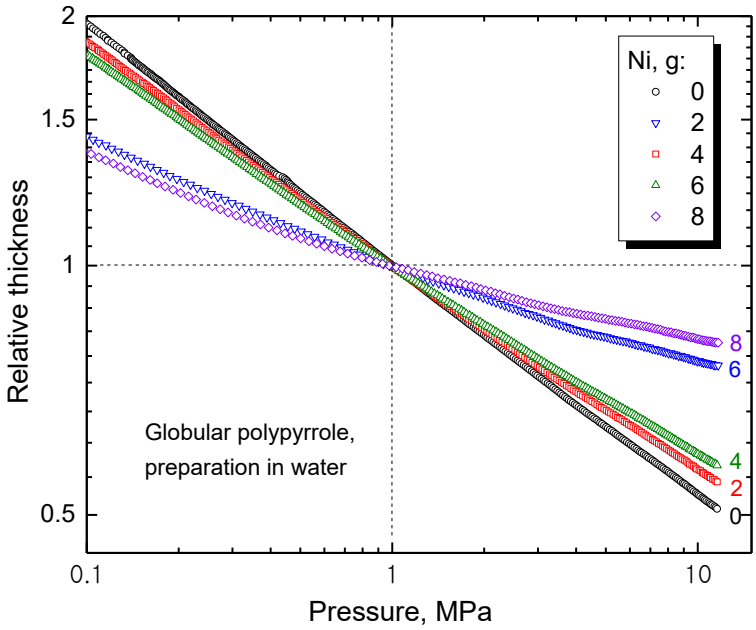

Figure 8. Pressure dependence of sample thickness relative to the thickness at 1 MPa for various contents of nickel.

3.6. Magnetic Properties

The magnetisation curves reflect the properties of nickel (Figure 9). The saturation magnetisation increased with nickel content (Table 3). As expected, polypyrrole does not contribute to magnetic properties, and consequently, its morphology has no effect.

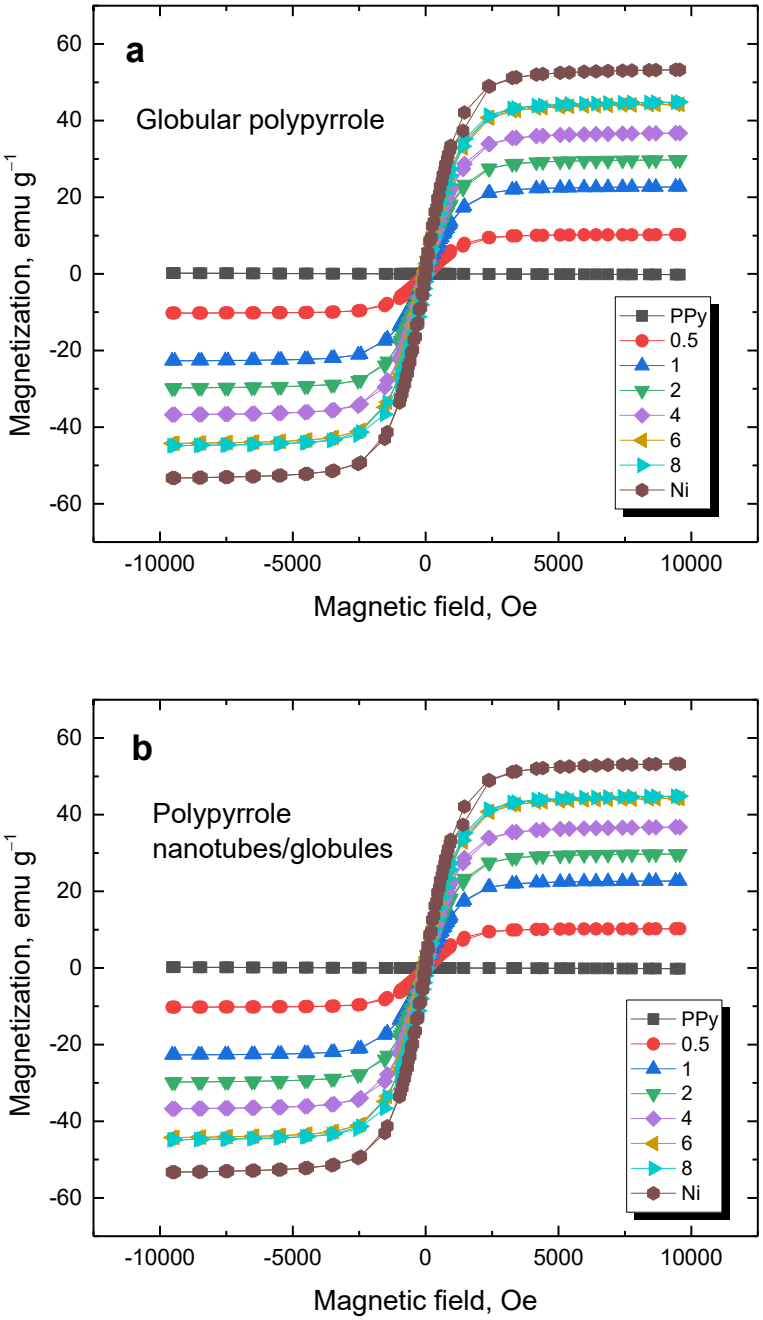

Figure 9. Magnetisation curves of (**a**) globular polypyrrole and (**b**) polypyrrole nanotubes/globules deposited on various amounts of nickel microparticles (in g).

Table 3. Coercivity, H_C, remanent magnetisation, M_R, and saturation magnetisation, M_S, of polypyrrole composites prepared with various amounts of nickel, *Ni*, in water.

Ni, g	H_C, Oe	M_R, emu g^{-1}	M_S, emu g^{-1}
Globular polypyrrole			
0.5	38.0	1.78	10.2
1	39.0	5.47	22.7
2	39.4	1.14	29.7
4	39.6	1.85	36.7
6	39.7	0.02	44.2
8	40.1	2.04	44.8

Polypyrrole nanotubes/globules			
0.5	38.9	2.26	11.7
1	38.5	4.87	15.3
2	38.8	7.19	17.6
4	39.9	1.48	28.7
6	40.3	2.00	39.3
8	40.2	3.82	44.3
Nickel			
Ni	41.7	0.2	53.3

3.7. Magnetorheology

Magnetorheology deals with the liquid suspensions of magnetic particles and the changes in their rheology produced by applied magnetic fields. The prospective applications include magnetorheological dampers and mechanical shock absorbers in the automotive industry that become important with the expanding electromobility and availability of magnetic fields generated by electromagnets. Magnetorheological dampers are developed for military vehicles or aerospace. The composites are of promise in stimuli-responsive polymer systems in biomedical sciences [30], e.g., in human prostheses.

Due to the magnetic properties afforded by nickel, the composites with polypyrrole can be tested in the design of magnetorheological fluids composed of magnetic micrometre-sized particles and a non-magnetic liquid phase [31]. The viscosity of these suspensions increases by several orders of magnitude in less than a second when an external magnetic field is applied. Due to the density mismatch of the particles and the carrier medium, these systems suffer from sedimentation instability. The coating of metal particles with organics is one of the most common solutions [32]. It reduces the average density of composite particles and thus prevents the sedimentation of the solid phase [33,34]. The systems incorporating nickel have been reported seldom [35]. It has been observed that the magnetorheological effect depended on the morphology [36] and particle size [37] of the dispersed phase. The coating of nickel particles with polypyrrole reported in the present study may also be regarded as a way to alter the properties of the dispersed phase.

The flow curves of the composite prepared with 8 g of nickel (=83.2 wt% Ni, Table 2) are shown in Figure 10. The shear stress increased with the intensity of the magnetic field up to 450 kA m^{-1}. Then, the particles were magnetically saturated (as shown in the magnetisation curves), and the shear stress remained at approximately the same level. For the majority of the experimental window, the stress increased more than 10 times. A Bingham plastic behaviour was observed during the on-state. The particles form chain-like structures, granting the fluid a yield stress. However, above the shear rate of 1 s^{-1}, the hydrodynamic forces started to compete with magnetostatic ones, eventually overtaking them. During the off-state below the shear rate of 10 s^{-1}, flow instability was observed as a result of shear banding. This is a common behaviour for certain colloids especially when a plate–plate geometry is used. The selection of this geometry, however, is key for a uniform magnetic field. A dotted line has been drawn following the behaviour at high shear rates for comparison in case there was no shear banding.

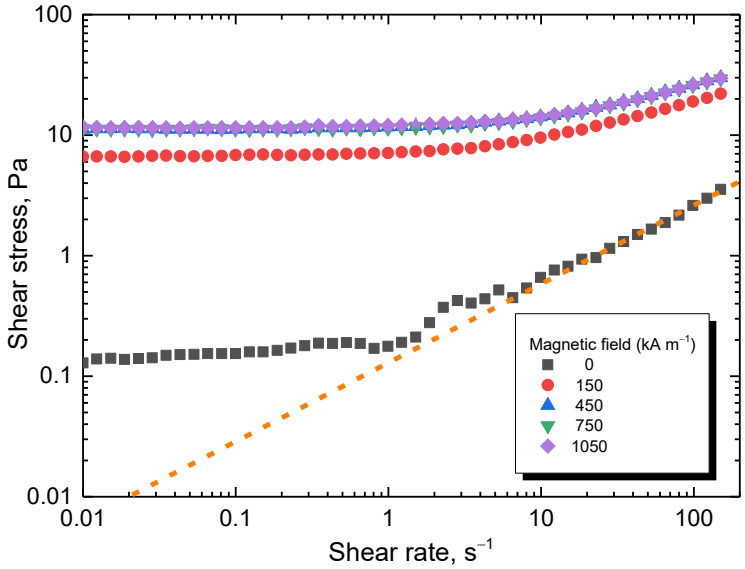

Figure 10. Flow curves at various magnetic fields for the composite prepared with 8 g of nickel. The dashed line represents the potential flow curve during the off-state if the shear band is not present.

The flow curves for the sample using the lowest 2 g content of nickel in the reaction mixture (=56.4 wt% Ni, Table 2) can be seen in Figure 11a. When a magnetic field was applied, the shear stress significantly increased, with the trend being similar to the sample shown in Figure 10. However, the shear stress increase is lower for the sample with low nickel content due to the lower content of the magnetic component. The same instabilities were observed (Figure 11b). However, for repetitions of the flow curves, a behaviour closer to reality is found, with the data not forming an unstable plateau. The data at lower shear rates are scattered due to the low torque measured by the instrument. Nevertheless, the trend is clear.

Furthermore, both tested samples were exposed to a steady shear rate of 50 s^{-1} with the magnetic field turned on and off every 20 s and gradually increasing level (Figure 12a). The stress increased immediately after the magnetic field was applied. When the magnetic field was turned off, the stress reached its original values, showing great control. The sample with a high 8 g nickel content showed both lower off-state and higher on-state stress, promoting it as a better candidate for applications regarding magnetorheology. The average stress of the on- and off-states was calculated for both samples, and the magnetorheological performance was obtained by dividing the on-state stress by the off-state one (Figure 12b). The sample with 8 g nickel had approximately three times higher performance while, for both samples above 450 kA m^{-1}, the performance remained the same as the nickel particles were magnetically saturated. It is important to note that there was a nickel ferrite-based magnetorheological fluid with a similar carrier [35]. Present composite particles have nearly two times higher performance with only 9 wt% loading, while the compared system [35] used 60 wt% particles.

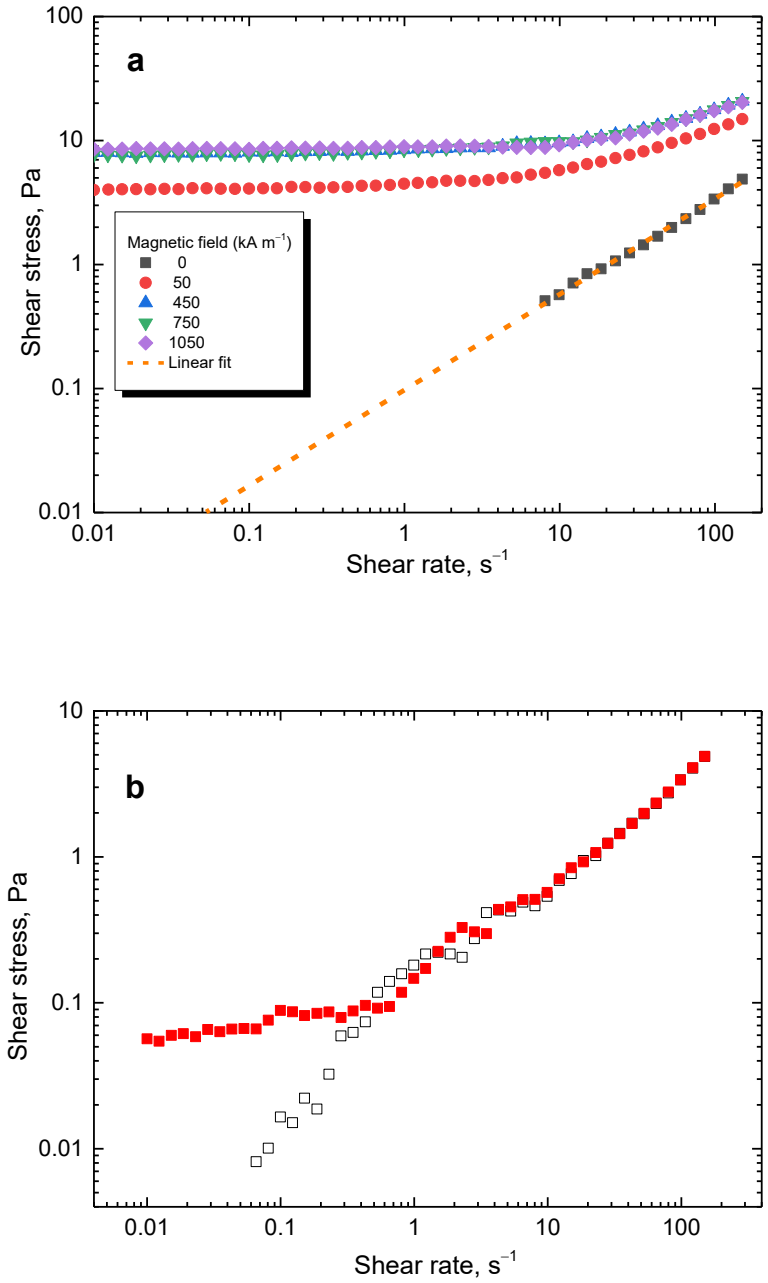

Figure 11. (**a**) Flow curves at various magnetic fields for the lowest 2 g nickel content. The dashed line represents a potential flow curve during the off-state if the shear band was not present. (**b**) Flow curves during the off-state. The full squares depict data with shear banding present, while open squares are those without shear banding.

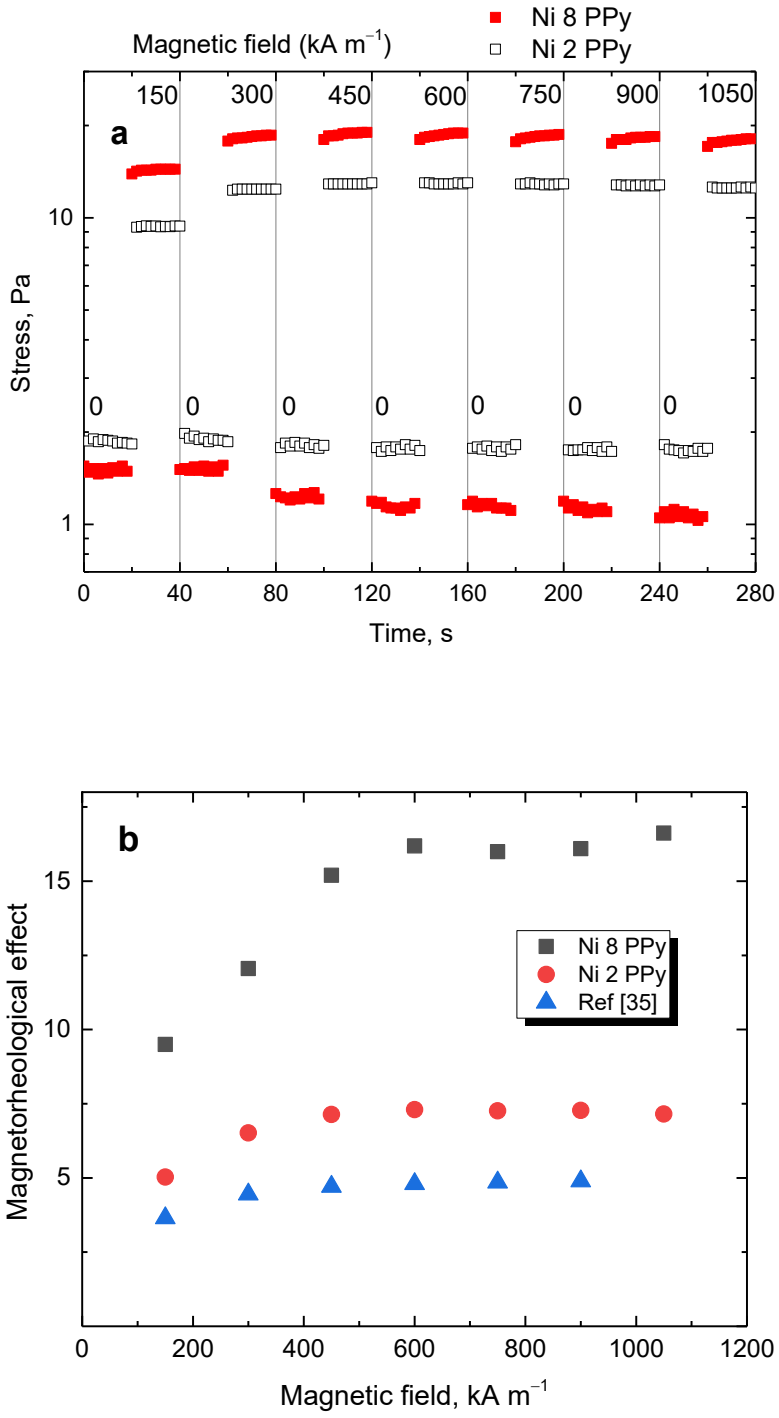

Figure 12. (**a**) Stepwise increase in the magnetic field under the shear rate of 50 s^{-1} for samples prepared with 8 g (full squares) and 2 g nickel (open squares). (**b**) The magnetorheological performance as a function of the magnetic field for composites prepared with 8 g (squares) or 2 g nickel (circles) and the comparison with data reported in the literature [35] (triangles).

4. Conclusions

The hybrid organic/inorganic composites displaying electrical conductivity and magnetic properties, polypyrrole-coated nickel microparticles, have been prepared and characterised. While the oxidation of pyrrole with iron(III) chloride in the presence of nickel does not provide desired composites due to the metal dissolution, the use of am-

monium peroxydisulfate does. The resistivity of composite powders has been newly determined as a function of applied pressure. The conductivity measured on pellets was of the order of 10^{-1} S cm^{-1}, i.e., slightly lower than that of neat polypyrrole. Electrical properties did not depend on the polypyrrole morphology, globules or nanotubes, or acidity of the reaction medium. The conductivity of nickel did not contribute to the overall conductivity of composites, which was determined only by the polypyrrole matrix. In fact, the conductivity moderately decreased with increasing content of well-conducting nickel. This apparent paradox is explained by the inability of nickel cores to produce conducting pathways, as they are always separated by polypyrrole coating. Magnetic properties were independent of polypyrrole content and morphology, and the magnetisation was proportional to the nickel content. The hybrid composites of this type may find application as competitive functional materials, e.g., in magnetorheology, as illustrated by present results.

Author Contributions: M.J.: Synthesis, Writing—review & editing. J.V.: Formal analysis. N.E.K.: Validation. A.M.: Investigation, Writing—review & editing. L.M.: Data Curation. M.S.: Supervision, Funding acquisition, Resources. J.S.: Conceptualization, Writing—original draft. M.T.: Investigation, Data curation. J.P.: Investigation, Validation. All authors have read and agreed to the published version of the manuscript.

Funding: The authors thank the Czech Science Foundation (A.M., M.S., L.M.: 23-07244S and J.S.: 22-25734S) for financial support.

Institutional Review Board Statement: Not applicable.

Informed Consent Statement: Not applicable.

Data Availability Statement: Data are contained within the article.

Conflicts of Interest: The authors declare no conflicts of interest.

References

1. Obodo, R.M.; Shinde, N.M.; Chime, U.K.; Ezugwu, S.; Nwanya, A.C.; Ahmad, S.; Maaza, M.; Ejikeme, P.M.; Ezema, F.I. Recent advances in metal oxide/hydroxide on three-dimensional nickel foam substrate for high performance pseudocapacitive electrodes. *Curr. Opin. Electrochem.* **2020**, *21*, 242–249. https://doi.org/10.1016/j.coelec.2020.02.022.
2. Ul-Hoque, M.I.; Holze, R. Intrinsically conducting polymer composites as active masses in supercapacitors. *Polymers* **2023**, *15*, 730. https://doi.org/10.3390/polym15030730.
3. Irshad, M.S.; Arshad, N.; Wang, X.B.; Li, H.R.; Javed, M.Q.; Xu, Y.; Alshahrani, L.A.; Mei, T.; Li, J.H. Intensifying solar interfacial heat accumulation for clean water generation excluding heavy metal ions and oil emulsions. *Solar RRL* **2021**, *5*, 2100427. https://doi.org/10.1002/solr.202100427.
4. Ghanbari, R.; Ghorbani, S.R. High-performance nickel molybdate/reduced graphene oxide/polypyrrole ternary nanocomposite as flexible all-solid-state asymmetric supercapacitor. *J. Energy Storage* **2023**, *60*, 106670. https://doi.org/10.1016/j.est.2023.106670.
5. Shi, A.R.; Song, X.M.; Wei, L.; Ma, H.Y.; Pang, H.J.; Li, W.W.; Liu, X.W.; Tan, L.C. Design of an internal/external bicontinuous conductive network for high-performance asymmetrical supercapacitors. *Molecules* **2023**, *27*, 8168. https://doi.org/10.3390/molecules27238168.
6. Zhao, M.M.; Zhao, Q.X.; Li, B.; Xue, H.G.; Pang, H.; Chen, C.Y. Recent progress in layered double hydroxide based materials for electrochemical capacitors: Design, synthesis and performance. *Nanoscale* **2017**, *9*, 15206–15225. https://doi.org/10.1039/c7nr04752e.
7. Wei, J.T.; Xing, G.Z.; Gao, L.; Suo, H.; He, X.P.; Zhao, C.; Li, S.; Xing, S.X. Nickel foam based polypyrrole-Ag composite film: A new route toward stable electrodes for supercapacitors. *New J. Chem.* **2013**, *37*, 337–341. https://doi.org/10.1039/c2nj40590c.
8. Gao, J.; Wang, X.H.; Wang, X.Q.; Que, R.H.; Fang, Y.; Shi, B.; Wang, Z.H. Hierarchical polypyrrole/Ni_3S_2@MoS_2 core-shell nanostructures on a nickel foam for high-performance supercapacitors. *RSC Adv.* **2016**, *6*, 68460–68467. https://doi.org/10.1039/c6ra12095d.
9. Hasanzadeh, M.; Ansari, R.; Farahpour, M. Cobalt disulfide/polypyrrole cauliflower-like nanocomposite: Single-pot hydrothermal synthesis, characterization, and their enhanced storage energy in supercapacitors. *J. Alloy Compd.* **2023**, *951*, 169965. https://doi.org/10.1016/j.jallcom.2023.169965.
10. Wang, S.; Fan, Y.K.; Wang, F.; Su, Y.N.; Zhou, X.; Zhu, Z.Q.; Sun, H.X.; Liang, W.D.; Li, A. Potentially scalable fabrication of salt-rejection evaporator based on electrogenerated polypyrrole-coated nickel foam for efficient solar steam generation. *Desalination* **2021**, *505*, 114982. https://doi.org/10.1016/j.desal.2021.114982.

11. Karazehir, T. Electrodeposited Pd nanoparticles on polypyrrole/nickel foam for efficient methanol oxidation. *Int. J. Hydrogen Energy* **2023**, *48*, 10493–10506. https://doi.org/10.1016/j.ijhydene.2022.12.059.
12. Yu, H.B.; Che, M.; Zhao, B.; Lu, Y.; Zhu, S.Y.; Wang, X.H.; Qin, W.C.; Huo, M.X. Enhanced electrosorption of rhodamine B over porous copper-nickel foam electrodes modified with graphene oxide/polypyrrole. *Synth. Met.* **2021**, *262*, 116332. https://doi.org/10.1016/j.synthmet.2020.116332.
13. Ren, J.; Shen, M.; Li, Z.L.; Yang, C.M.; Liang, Y.; Wang, H.E.; Li, J.H.; Li, N.; Qian, D. Towards high-performance all-solid-state asymmetric supercapacitors: A hierarchical doughnut-like Ni_3S_2@PPy core-shell heterostructure on nickel foam electrode and density functional theory calculations. *J. Power Sources* **2021**, *501*, 230003. https://doi.org/10.1016/j.jpowsour.2021.230003.
14. Song, Y.C.; Hong, P.D.; Li, T.F.; Ma, G.X.; Deng, Q.H.; Zhou, Y.M.; Zhang, Y.W. A nanoflower-like polypyrrole-based cobalt-nickel sulfide hybrid heterostructures with electrons migration to boost overall water splitting. *J. Colloid Interface Sci.* **2022**, *618*, 1–10. https://doi.org/10.1016/j.jcis.2022.03.035.
15. Li, J.; Zou, Y.J.; Li, B.; Xu, F.; Chu, H.L.; Qiu, S.J.; Zhang, J.; Sun, L.X.; Xiang, C.L. Polypyrrole-wrapped $NiCo_2S_4$ nanoneedles as an electrode material for supercapacitor applications. *Ceram. Int.* **2021**, *47*, 16562–16569. https://doi.org/10.1016/j.ceramint.2021.02.227.
16. Shen, X.J.; Wei, X.Y.; Wang, T.F.; Li, S.M.; Li, H.T. Polypyrrole embedded in nickel-cobalt sulfide nanosheets grown on nickel particles passivated silicon nanowire arrays for high-performance supercapacitors. *Chem. Eng. J.* **2023**, *461*, 141745. https://doi.org/10.1016/j.cej.2023.141745.
17. Kumar, A.; Kumar, S.; Jana, S.; Prakash, R. Investigation of the synergistic effect in polypyrrole/Ni-doped NASICON composites for an enhanced hydrogen evolution reaction. *Energy Fuels* **2023**, *37*, 4552–4565. https://doi.org/10.1021/acs.energyfuels.2c04178.
18. Jiao, F.Z.; Wu, J.; Zhang, T.T.; Pan, R.J.; Wang, Z.H.; Yu, Z.Z.; Qu, J. Simultaneous solar-thermal desalination and catalytic degradation of wastewater containing both salt ions and organic contaminants. *ACS Appl. Mater. Interfaces* **2023**, *15*, 41007–41018. https://doi.org/10.1021/acsami.3c09346.
19. Oriňáková, R.; Filkusová, M. Hydrogen evolution on microstructured polypyrrole films modified with nickel. *Synth. Met.* **2010**, *160*, 927–931. https://doi.org/10.1016/j.synthmet.2010.02.002.
20. Chemchoub, S.; Oularbi, L.; El Attar, A.; Younssi, S.A.; Bentiss, F.; Jama, C.; El Rhazi, M. Cost-effective non-noble metal supported on conducting polymer composite such as nickel nanoparticles/polypyrrole as efficient anode electrocatalyst for ethanol oxidation. *Mater. Chem. Phys.* **2020**, *250*, 123009. https://doi.org/10.1016/j.matchemphys.2020.123009.
21. Emir, G.; Dilgin, Y.; Ramanaviciene, A.; Ramanavicius, A. Amperometric nonenzymatic glucose biosensor based on graphite rod electrode modified by Ni-nanoparticle/polypyrrole composite. *Microchem. J.* **2021**, *161*, 105751. https://doi.org/10.1016/j.microc.2020.105751.
22. Šišoláková, I.; Gorejová, R.; Chovancová, F.; Shepa, J.; Ngwabebhoh, F.A.; Fedorková, A.S.; Sáha, P.; Oriňáková, R. Polymer-based electrochemical sensor: Fast, accurate, and simple insulin diagnostics tool. *Electrocatalysis* **2023**, *14*, 697–707. https://doi.org/10.1007/s12678-023-00827-w.
23. Genetti, W.B.; Yuan, W.L.; Grady, B.P.; O'Rear, E.A.; Lai, C.L.; Glatzhofer, D.T. Polymer matrix composites: Conductivity enhancement through polypyrrole coating of nickel flake. *J. Mater. Sci.* **1998**, *33*, 3085–3093. https://doi.org/10.1023/A:1004387621165.
24. Guo, J.; Li, X.; Chen, Z.R.; Zhu, J.F.; Mai, X.M.; Wei, R.B.; Sun, K.; Liu, H.; Chen, Y.X.; Naik, N. Magnetic $NiFe_2O_4$/polypyrrole nanocomposites with enhanced electromagnetic wave absorption. *J. Mater. Sci. Technol.* **2022**, *108*, 64–72. https://doi.org/10.1016/j.jmst.2021.08.049.
25. Jurča, M.; Vilčáková, J.; Kazantseva, N.E.; Prokeš, J.; Trchová, M.; Stejskal, J. Conducting and magnetic hybrid polyaniline/nickel composites. *Synth. Met.* **2022**, *291*, 117165. https://doi.org/10.1016/j.synthmet.2022.117165.
26. Saraswat, A.; Kumar, S. Cutting-edge applications of polyaniline composites towards futuristic energy supply devices. *Eur. Polym. J.* **2023**, *200*, 112501. https://doi.org/10.1016/j.eurpolymj.2023.112501.
27. Stejskal, J.; Vilčáková, J.; Jurča, M.; Fei, H.J.; Trchová, M.; Kolská, Z.; Prokeš, J.; Křivka, I. Polypyrrole-coated melamine sponge as a precursor for conducting macroporous nitrogen-containing carbons. *Coatings* **2022**, *12*, 324. https://doi.org/10.3390/coatings12030324.
28. Cascales, J.J.L.; Fernandez, A.J.; Otero, T.F. Characterization of the reduced and oxidized polypyrrole/water interface: A molecular dynamics simulation study. *J. Phys. Chem. B* **2003**, *107*, 9339–9343. https://doi.org/10.1021/jp027717o.
29. Trchová, M.; Stejskal, J. Resonance Raman spectroscopy of conducting polypyrrole nanotubes: Disordered surface versus ordered body. *J. Phys. Chem. A* **2018**, *122*, 9298−9306. https://doi.org/10.1021/acs.jpca.8b09794.
30. Shymborska, Y.; Budkowski, A.; Raczkowska, J.; Donchak, V.; Vasiichuk, V.; Stetsyshyn, Y. Switching it up: The promise of stimuli-responsive polymer systems in biomedical science. *Chem. Rec.* **2023**, e202300217. https://doi.org/10.1002/tcr.202300217.
31. Park, B.J.; Fang, F.F.; Choi, H.J. Magnetorheology: Materials and application. *Soft Matter* **2010**, *6*, 5246–5253. https://doi.org/10.1039/C0SM00014K.
32. Lim, S.T.; Cho, M.S.; Jang, I.B.; Choi, H.J. Magnetorheological characterization of carbonyl iron based suspension stabilized by fumed silica. *J. Magn. Magn. Mater.* **2004**, *282*, 170–173. https://doi.org/10.1016/j.jmmm.2004.04.040.
33. Fang, F.F.; Kim, J.H.; Choi, H.J. Synthesis of core-shell structured PS/Fe_3O_4 microbeads and their magnetorheology. *Polymer* **2009**, *50*, 2290–2293. https://doi.org/10.1016/j.polymer.2009.03.023.

34. Munteanu, A.; Plachý, T.; Munteanu, L.; Ngwabebhoh, F.A.; Stejskal, J.; Trchová, M.; Kubík, M.; Sedlačík, M. Bidisperse magnetorheological fluids utilizing composite polypyrrole nanotubes/magnetite nanoparticles and carbonyl iron microspheres. *Rheol. Acta* **2023**, *62*, 461–472. https://doi.org/10.1007/s00397-023-01409-9.
35. Munteanu, L.; Masař, M.; Sedlačík, M.; Kohl, M.; Kalendová, A. Magneto-active ferrite-based paint pigments. *AIP Conf. Proc.* **2023**, *2997*, 040006. https://doi.org/10.1063/5.0159567.
36. Morillas, J.R.; Carreón-González, E.; de Vicente, J. Effect of particle aspect ratio in magnetorheology. *Smart Mater. Struct.* **2015**, *24*, 125005. https://doi.org/10.1088/0964-1726/24/12/125005.
37. Gwon, H.; Park, S.; Lu, Q.; Choi, H.J.; Lee, S. Size effect of iron oxide nanorods with controlled aspect ratio on magneto-responsive behavior. *J. Ind. Eng. Chem.* **2023**, *124*, 279–286. https://doi.org/10.1016/j.jiec.2023.04.017.